Universal parameters of the $\Lambda(1380)$, the $\Lambda(1405)$, and their isospin partners from a combined analysis of lattice QCD and experimental results

Ferenc Pittler,[1,*] Maxim Mai,[2,3,†] Ulf-G. Meißner,[4,5,6,‡] Ryan F. Ferguson,[7] Peter Hurck,[7] David G. Ireland,[7] and Bryan McKinnon[7]

[1]*Computation-Based Science and Technology Research Center, The Cyprus Institute, Nicosia, Cyprus*
[2]*Albert Einstein Center for Fundamental Physics, Institute for Theoretical Physics, University of Bern, Sidlerstrasse 5, 3012 Bern, Switzerland*
[3]*Institute for Nuclear Studies and Department of Physics, The George Washington University, Washington, DC 20052, USA*
[4]*Helmholtz-Institut für Strahlen- und Kernphysik (Theorie) and Bethe Center for Theoretical Physics, Universität Bonn, 53115 Bonn, Germany*
[5]*Institute for Advanced Simulation (IAS-4), Forschungszentrum Jülich, D-52425 Jülich, Germany*
[6]*Peng Huanwu Collaborative Center for Research and Education, International Institute for Interdisciplinary and Frontiers, Beihang University, Beijing 100191, China*
[7]*School of Physics and Astronomy, University of Glasgow, Glasgow, G12 8QQ, United Kingdom*

(Received 13 August 2025; accepted 30 September 2025; published 28 October 2025)

We perform a global analysis of lattice and experimental data on negative-strangeness meson-baryon scattering using a large set of variations of the theoretical framework based on the chiral unitary approach. For the former, the Lüscher formalism is utilized taking into account all pertinent coupled-channel effects. Through this, systematic uncertainties related to data scarcity, potential ambiguities, and possible framework dependence are quantified for the first time. The implementation of information criteria and other statistical tools is discussed. As a final result we provide pole positions for isoscalar resonances at the physical and lattice points, including statistical and systematic uncertainties. Predictions for the isovector states are also provided, showing large uncertainties.

DOI: 10.1103/ls4c-6f2y

I. INTRODUCTION AND SUMMARY

The hadron spectrum provides a manifestation of structure formation of the strong interaction, which remains a challenge to our understanding of the so successful standard model of particle physics. Primarily due to advances in experimental techniques, hundreds of new and predominantly excited hadrons have been discovered over the past century [1]. A partial ordering of the spectrum can be achieved through a simple quark model organizing mesons as quark-antiquark and baryons as three-quark states. However, this simple picture does not reflect the reality calling for a more comprehensive approach. For recent related reviews, see Refs. [2–6]. A prominent example of this kind is the negative-strangeness, isoscalar $\Lambda(1405)$ baryon, which became a poster child of the two-pole structure [7,8]. Currently, this is associated with two states, the $\Lambda(1405)$ and $\Lambda(1380)$. For a dedicated review including historical aspects, see Ref. [9] as well as Refs. [8,10] for a broader context.

Originally, the connection between the fundamental theory of the strong interaction, quantum chromodynamics (QCD), and the phenomenology of the two-pole structure of the $\Lambda(1405)$ was established using chiral perturbation theory (CHPT) while extending the range of applicability through unitarization techniques. For details and connection to other approaches see Ref. [9]. Note further that the isovector pole also seen in Ref. [7] (see also [11–14]) has obtained much less attention, but this issue will also be taken up here. Typically, the free parameters of this approach are fixed using the data available from experiments conducted over the last several decades. These parameters originate partly from the so-called low-energy constants, which encode the effects of integrated out heavy degrees of freedom of QCD but also reflect a certain degree of model dependence in the exact prescription of the unitarization procedure. This model dependence, along

*Contact author: f.pittler@cyi.ac.cy
†Contact author: maxim.mai@faculty.unibe.ch
‡Contact author: meissner@hiskp.uni-bonn.de

TABLE I. Numerical values for extracted pole positions (combined fit to lattice and experimental input) for the isoscalar and isovector case (in GeV). Different fits refer to variations of the UCHPT approach, as explained in Sec. IV (where M refers to the chosen interaction kernel and S to the method of regularization). The lattice point refers to the quark mass setup used in Refs. [20,21].

	Type	Physical point	Lattice point
$I=0$ $S=-1$	M3S1 (F_{17})	$1.342^{+0.009}_{-0.010} - i0.028^{+0.013}_{-0.014}$	$1.359^{+0.010}_{-0.014} - i0.100^{+0.050}_{-0.050}$
		$1.432^{+0.002}_{-0.002} - i0.025^{+0.001}_{-0.001}$	$1.460^{+0.006}_{-0.005} - i0.013^{+0.005}_{-0.004}$
	M3S2 (F_{16})	$1.373^{+0.002}_{-0.005} - i0.082^{+0.011}_{-0.009}$	$1.389^{+0.006}_{-0.007}$
		$1.423^{+0.002}_{-0.001} - i0.020^{+0.001}_{-0.002}$	$1.466^{+0.003}_{-0.004} - i0.020^{+0.001}_{-0.001}$
	M3S3 (F_{12})	$1.352^{+0.004}_{-0.007} - i0.091^{+0.005}_{-0.006}$	$1.401^{+0.003}_{-0.003}$
		$1.420^{+0.001}_{-0.001} - i0.018^{+0.001}_{-0.001}$	$1.478^{+0.005}_{-0.004} - i0.026^{+0.001}_{-0.001}$
$I=1$ $S=-1$	M3S1 (F_{17})	$1.351^{+0.022}_{-0.015} - i0.112^{+0.010}_{-0.011}$	$1.333^{+0.018}_{-0.024} - i0.144^{+0.008}_{-0.012}$
		$1.356^{+0.005}_{-0.011} - i0.035^{+0.022}_{-0.014}$	
	M3S2 (F_{16})	$1.430^{+0.090}_{-0.040} - i0.281^{+0.170}_{-0.002}$	$1.430^{+0.050}_{-0.060} - i0.208^{+0.090}_{-0.000}$
	M3S3 (F_{12})	$1.338^{+0.021}_{-0.023} - i0.215^{+0.007}_{-0.004}$	$1.335^{+0.025}_{-0.017} - i0.143^{+0.008}_{-0.005}$

with ambiguities in the existing experimental input, leads to different predictions of the chiral unitary approaches (UCHPT) in regimes not covered by the experimental data. Illustrative examples of such systematic uncertainties are discussed in, e.g., Refs. [9,11].

The problem can also be tackled from a different angle using lattice QCD methodology [15–19]. In a most recent calculation, not too far away from the physical point (that is, quark masses that are only slightly larger than the physical ones) and using state-of-the-art methodology, finite-volume spectra for the isoscalar channel of negative-strangeness meson-baryon interaction have been determined by BaSc collaboration [20,21]. While unphysical quark masses are used in this setup, CHPT underlying UCHPT allows one to extrapolate and connect these results to the physical point. Establishing this connection, along with the study of the model dependence within the UCHPT approaches, constitutes the main goals of the present work. The central observations of our study can be summarized as follows:

(i) UCHPT approaches based on the lowest-order chiral Lagrangian (called type M1 and M2 in what follows) do capture the main features of the interaction but fail to quantitatively describe the existing experimental data.

(ii) UCHPT can accurately describe the lattice input. Still, the latter input alone does not seems sufficient for determining accurately both pole positions when model variations are taken into account.

(iii) Within the most flexible models, the experimental input does lead to the pole structure similar to that found in the existing literature. When extrapolating to the unphysical quark mass scenario (lattice point), the pole structure determined by BaSc collaboration is confirmed. For the most flexible models we observe that ambiguities in the older cross section data dominate the systematic uncertainties.

(iv) Combined fits including all experimental and lattice inputs provide a very good description. Variations between different models are assessed using information criteria. Numerical results for the isoscalar poles, as well as predicted isovector poles, are collected in Table I.

This paper is organized as follows. Details on the lattice QCD input are provided in Sec. II, which also includes details of the finite-volume implementation. The experimental data are reviewed in Sec. III, discussing also their ambiguities. The chiral unitary approach is discussed in Sec. IV, including variation of the methodology reflecting systematic uncertainties. Additionally, potential complications due to three-body on-shell states are evaluated in Sec. IV D. Fits and pertinent predictions are discussed in Secs. V and VI, respectively. Individual fit results are moved to the Appendices for convenience.

II. LATTICE QCD INPUT

A. Overview of the available quantities

Recent advances in both theoretical frameworks and computational techniques have enabled lattice QCD to make increasingly precise predictions for the properties of strongly interacting unstable particles (resonances), such as the ρ, Δ, and more recently, the $\Lambda(1405)$. For recent reviews, see Refs. [5,22,23]. In lattice calculations, one extracts information about such states by computing the discrete energy spectrum of multihadron scattering states in a finite Euclidean volume. This is achieved through Markov chain Monte Carlo integration and analyzing the exponential decay of correlation functions constructed from suitably designed interpolating operators. In his

seminal work, Lüscher showed that the energy levels of two interacting hadrons in a finite spatial volume are shifted from their noninteracting values by an amount that is only power-law suppressed in the box size [24,25]. These finite-volume energy shifts are directly related to the infinite-volume scattering phase shift [26,27], and hence to the scattering amplitudes themselves. Subsequent works extended Lüscher's formalism to arbitrary spins and multiple coupled channels [28–32]. In the following subsection, we briefly summarize the quantization condition used in the present work.

B. Implementation of the quantization condition

Experimental observables, such as cross sections and the finite-volume energy spectrum obtained from lattice simulations, can both be described using effective models in which the scattering amplitude is parametrized using a small number of input parameters. These parameters are constrained through a correlated χ^2 fit to both types of data: the finite-volume lattice energy spectrum and experimental observables.

Instead of parametrizing the unitary S-matrix directly, we work with the real, symmetric K-matrix, which is related to the S-matrix via

$$S = (1 - iK)^{-1}(1 + iK). \tag{2.1}$$

Due to rotational invariance, the infinite dimensional K-matrix is diagonal in angular momentum space,

$$\langle J' m_{J'} \ell' S' a' | K | J m_J \ell S a \rangle = \delta_{JJ'} \delta_{m_J m_{J'}} K^{(J)}_{\ell' S' a'; \ell S a}(s), \tag{2.2}$$

where the states $|Jm_J\ell Sa\rangle$ are labeled by the total angular momentum J, its projection on the z-axis m_J, the total orbital angular momentum ℓ, and the spin angular momentum S of the two particles, respectively, a is the channel index, and lastly, s is the Mandelstam variable, the square of the total energy in the center-of-mass frame. In this section, we connect the parametrization of the K-matrix used in the quantization condition [20] with the UCHPT parametrizations (e.g., Refs. [33–35]), which provide what is often referred to as the Höhler's partial-wave amplitudes $f_{\ell\pm}(s)$ [36,37], described later in Sec. IV B in terms of the T-matrix. We also briefly summarize the quantization condition in multichannel space applied in this work, closely following [22,38].

To connect the two parametrizations, physical quantities are extracted from both meson-baryon scattering $MB \to MB$ Höhler partial-wave amplitudes and $\tilde{K}$ [38]. For example, using the former, the elastic scattering phase shifts can be computed through a K-matrix-like quantity as

$$\begin{aligned} f_{0+}(s) &= \frac{1}{(\tilde{K}_E^{-1}(s) - i p_{\rm cm}(s))} \Rightarrow \cot\delta = \frac{\mathrm{Re} f_{0+}}{\mathrm{Im} f_{0+}} \\ &= \frac{\tilde{K}_E^{-1}}{p_{\rm cm}} \Rightarrow p_{\rm cm} \cot\delta = \tilde{K}_E^{-1}. \end{aligned} \tag{2.3}$$

Here, $p_{\rm cm}$ denotes the magnitude of the three-momentum in the center-of-mass frame. In the same region, the phase shifts can also be extracted using $\tilde{K}$, the matrix in the quantization condition for the finite-volume energy spectrum [38],

$$\det(1 - \tilde{K} B^{\vec{P}}) = 0, \tag{2.4}$$

where $\vec{P}$ is the total momentum of the two-particle system, $\tilde{K} = \frac{2\pi}{L p_{\rm cm}} K = \frac{2\pi}{L} \frac{1}{p_{\rm cm} \cot\delta} = \frac{2\pi}{L} \tilde{K}_E$, and here the first two equalities follow from Eqs. (16) and (18) in [38] and (2.3) is used in the last one. The so-called box matrix $B^{\vec{P}}$ does not depend on interactions—it is a known, purely kinematical matrix that depends on the finite volume. For real scattering momenta, $B^{\vec{P}}$ is Hermitian and diagonal in the channel space,

$$\langle J' m_{J'} \ell' S' a' | B^{\vec{p}} | J m_J \ell S a \rangle = -i \delta_{aa'} \delta_{SS'} p_{{\rm cm},a}^{\ell+\ell'+1} W^{\vec{P}a}_{\ell' m_{\ell'}; \ell m_\ell} \langle J' m_{J'} | \ell' m_{\ell'}, S m_S \rangle \langle \ell m_\ell, S m_S | J m_J \rangle, \tag{2.5}$$

where $\langle j_1 m_1 j_2 m_2 | J M \rangle$ are the familiar Clebsch-Gordan coefficients and W is defined in Eq. (6) in [38]. In practice, the infinite-dimensional matrix in the determinant (2.4) is block-diagonalized by projecting onto the superposition of states that transforms according to the irreducible representation (irrep) of the little group of $\vec{P}$, i.e., by performing a unitary basis transformation,

$$|\Lambda \lambda n J \ell S a\rangle = \sum_{m_J} c_{m_J}^{J (-1)^\ell; \Lambda \lambda n} |J m_J \ell S a\rangle, \tag{2.6}$$

where Λ is the irrep of the little group of $\vec{P}$, λ is the irrep row, and n is the occurrence of the particular irrep in the reducible representation $|Jm_J\ell Sa\rangle$. In each block, a truncation to $\ell \le \ell_{\rm max}$ is imposed to make the determinant condition manageable. In the present work, we consider only the S-wave, $\ell_{\rm max} = 0$. We include energy levels from the rest frame up to total momenta of three units of lattice momenta [20]. The interchannel interactions are encoded in the dense $\tilde{K}_E$ matrix, while the box matrix remains diagonal in the channel space. The matrix $\tilde{K}_E$ is a 10×10 matrix in

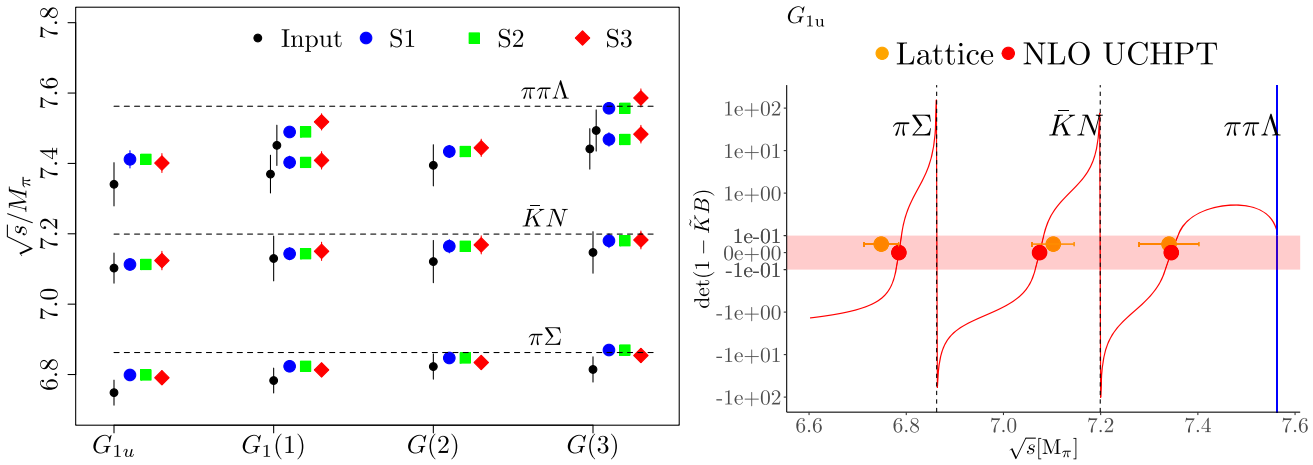

FIG. 1. Left: summary of energy levels used as input in this work (black dots with error bars), together with our model estimates using different regularization schemes (S1, S2, and S3). Right: illustration of the quantization condition as a function of the center-of-mass energy for the rest frame G_{1u} irrep. Red band highlights the area where the quantization condition is closely fulfilled, red circles indicate the prediction of UCHPT, and orange circles with error bars show the lattice results.

the space of meson-baryon channels with strangeness $S=-1$, as determined by the underlying $SU(3)$ symmetry

$$\mathcal{S} = \{K^- p, \bar{K}^0 n, \pi^0\Lambda, \pi^0\Sigma^0, \pi^+\Sigma^-, \pi^-\Sigma^+, \times \eta\Lambda, \eta\Sigma^0, K^+\Xi^-, K^0\Xi^0\}. \quad (2.7)$$

For lattice energy spectrum analysis, we further convert from the physical basis to the isospin basis and project onto channels with total isospin zero,

$$\mathcal{S}^{I=0} = \{\bar{K}N, \pi\Sigma, \eta\Lambda, K\Xi\}. \quad (2.8)$$

For phase convention and explicit forms of the projectors see, e.g., Ref. [39]. In predicting the finite-volume energy spectrum we compute the box matrix for the appropriate total momentum and irrep (a 4×4 diagonal matrix), and combine it with the corresponding 4×4 dense $\tilde{K}_E$ to evaluate the determinant in (2.4). An illustration of how the energy spectrum constrains the scattering amplitude is shown on the right part of Fig. 1 for the zero-momentum case (G_{1u} irrep).

In the spectrum we consider 14 energy levels, from all irreps dominated by $\ell=0$ lying below the first relevant three-particle threshold $\pi\pi\Lambda$. On the left part of Fig. 1 we show all the input energy levels together with our best estimates using three different regularizations S1, S2, and S3, as discussed later in Sec. IV.

C. Details of lattice calculation

The finite-volume lattice energy spectra have been generated using the D200 ensemble of CLS collaboration [40], which uses $2+1$ flavor of nonperturbatively improved Wilson fermions and Lüscher-Weisz gauge action. The pion mass is slightly higher than the physical one, and the kaon mass is slightly lower than the physical one. We summarize the details of the ensemble relevant to the present work in Table II. Correlation functions, including two-hadron interpolating fields at the source/sink with different combinations of momenta $[\pi(\vec{p}_1)\Sigma(\vec{p}_2)$, $\bar{K}(\vec{p}_1)N(\vec{p}_2)$ up to three lattice units of $\vec{p}_1+\vec{p}_2$ total momentum], were produced in order to determine all the energy levels in the isospin 0 sector below the lowest lying three-particle threshold ($\pi\pi\Lambda$). Correlation functions were evaluated using the stochastic Laplacian-Heaviside (sLapH) method [41,42]. The energy levels were obtained using the ratio method, i.e., taking the ratio of properly diagonalized correlation matrices (generalized eigenvalue problem principal correlators) with the single hadron correlators, directly determining the relevant energy shift [43]. The statistical errors are estimated via bootstrap resampling using 800 samples.

III. EXPERIMENTAL INPUT

Below we review all experimental input included in the present study. To have a more transparent picture of the

TABLE II. Properties of the D200 ensemble including the masses of the light meson and baryon octet at the isospin symmetric point.

L[fm]	a[fm]	M_π[GeV]	M_K[GeV]	M_η[GeV]	m_N[GeV]	m_Σ[GeV]	m_Λ[GeV]	m_Ξ[GeV]
4.05(4)	0.0633(7)	0.2036(8)	0.4864(5)	0.5511	0.979(11)	1.193(6)	1.132(4)	1.322(3)

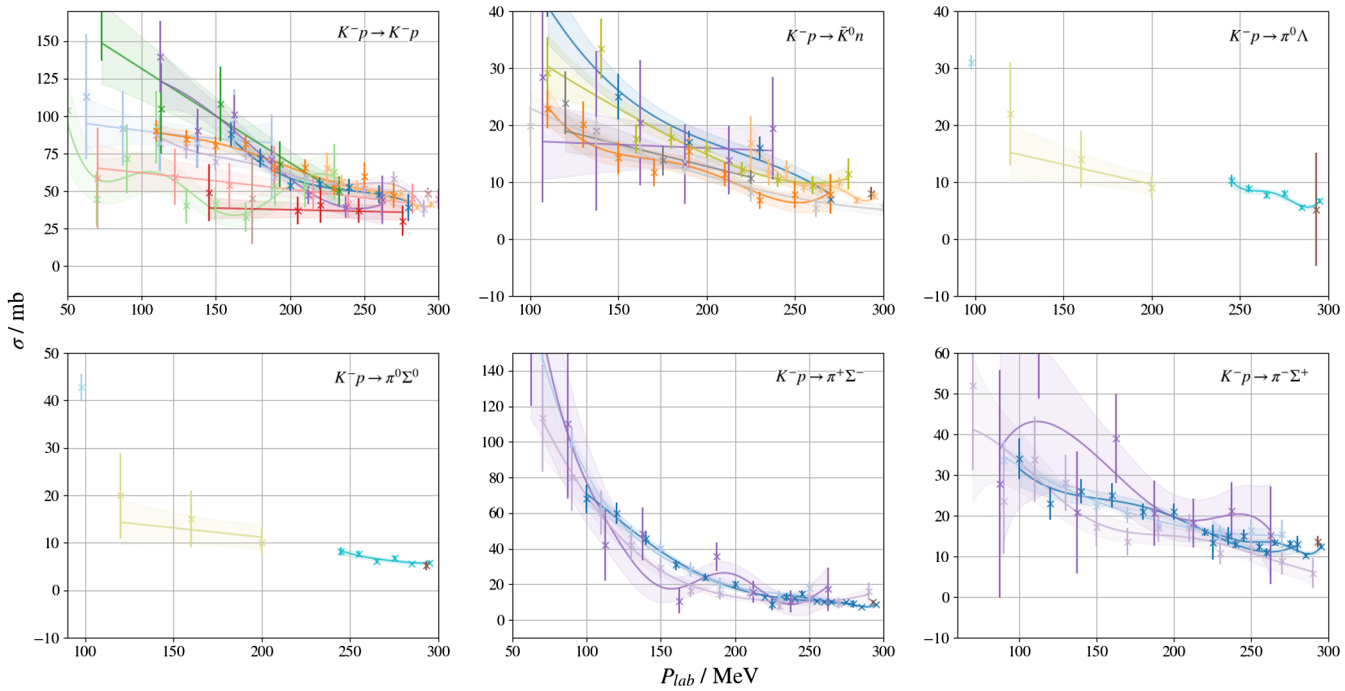

FIG. 2. Total cross sections considered in this work. Different colors distinguish between various experiments [52,54–57]. Shaded bands represent a Gaussian process fit, which is included to guide the eye [59].

systematic uncertainties discussed in Sec. IV, we restrict ourselves only to data which are directly related to the meson-baryon scattering amplitudes in the energy region most relevant for the $\Lambda(1380)$ and $\Lambda(1405)$ states. Other input from, e.g., photon-induced reactions [44–47], is not included, as it typically requires further parametrization of the reaction mechanism. For some studies of that type of data, see Refs. [48–51].

(i) *Cross sections:* Most of the experimental data in the energy region relevant for a study of the first resonance region stem from the time not long after the initiation of the first large experimental programs on production of kaons in the 1950s. For this, mostly data from bubble chamber setups at CERN, LBNL, BNL, or Bevatron were used until the mid 1980s. For a historical overview, see Ref. [9]. The data have, therefore, quite large error bars and in certain cases there are systematic discrepancies between different datasets. Encouragingly, in the 2020s, some progress occurred. As one of the most relevant recent developments in the field, AMADEUS collaboration [52] provided two new high-precision results based on data collected by KLOE collaboration [53] on the $K^-p \to \pi\Sigma^0$ and $K^-p \to \pi\Lambda$ total cross sections. The impact of these data has been studied within a UCHPT model in Ref. [35]. In the energy range of interest, i.e., kaon momentum in the laboratory frame below $P_{\mathrm{LAB}} \leq 300$ MeV, there are 252 total cross section data points [52,54–57] (83, 47, 11, 11, 51, and 49, corresponding to $K^-p \to K^-p$, $K^-p \to \bar{K}^0 n$, $K^-p \to \pi^0\Lambda$, $K^-p \to \pi^0\Sigma^0$, $K^-p \to \pi^+\Sigma^-$, and $K^-p \to \pi^-\Sigma^+$ transitions).[1] These data can be related to the partial-wave $f_{\ell\pm}$ derived form a given model. Neglecting higher partial waves, the explicit formula for the transition $\phi_\alpha B_\alpha \to \phi_\beta B_\beta$ reads

$$\sigma_{\alpha\beta} = 4\pi \frac{p_\beta(s)}{p_\alpha(s)} |f_{0+,\alpha\beta}(s)|^2, \tag{3.1}$$

where p_α refers to p_{cm} in the meson baryon channel α. For formulas including higher partial waves, we refer the reader to Refs. [36,58].

By plotting the cross section data with different colors for separate experiments (along with a corresponding Gaussian process fit if applicable), as we have in Fig. 2, it is readily seen that for several channels (K^-p, $\bar{K}^0 n$, and $\pi^-\Sigma^+$), the data are not only widely varying at some energies, but are even inconsistent. This is likely due to the effect of different systematic uncertainties in each experiment. By using squares of residuals to determine a χ^2 statistic, as is typically employed in analyses including this work, there is a chance that fits are drawn to the average of values, some of which are systematically wrong.

[1]The total cross section data in digitalized form can be accessed under: https://github.com/maxim-mai/Experimental-Data/tree/master/Lambda1405.

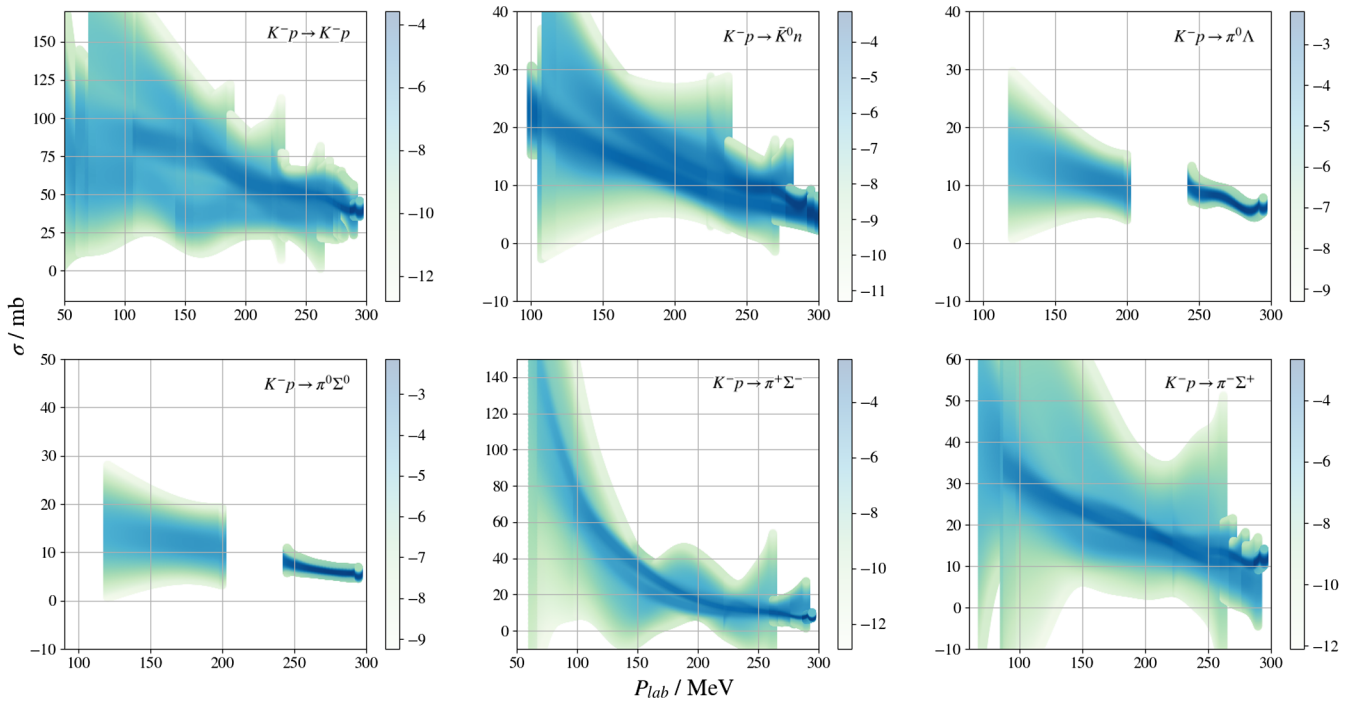

FIG. 3. Log probability surfaces derived from the data illustrated in Fig. 2.

This issue is further illustrated in Fig. 3, where the log probability surfaces for the data in Fig. 2 are depicted. The procedure for generating these surfaces is described in [59]. Particularly in the case of the $K^-p \to \bar{K}^0 n$ channel, the multiple bands suggest inconsistent data.

Note also that we consider the scattering data for energies high enough so that the Coulomb effect in the charged channels can be neglected.

(ii) *Threshold data:* At the K^-p threshold, several ratios of the cross sections were measured some decades ago [60,61]. Specifically, the values are $\gamma = 2.38 \pm 0.04$, $R_c = 0.664 \pm 0.011$, and $R_n = 0.189 \pm 0.015$, which are related to the total cross section ratios as

$$\gamma = \frac{\Gamma_{K^-p\to\pi^+\Sigma^-}}{\Gamma_{K^-p\to\pi^-\Sigma^+}}, \qquad R_c = \frac{\Gamma_{K^-p\to\text{charged states}}}{\Gamma_{K^-p\to\text{all final states}}},$$
$$R_n = \frac{\Gamma_{K^-p\to\pi^0\Lambda}}{\Gamma_{K^-p\to\text{neutral states}}}. \tag{3.2}$$

Additionally, in a more recent kaonic hydrogen experiment at DAPHNE, SIDDHARTA collaboration [62] determined to a very high precision the energy shift and width due to strong interaction of the K^-p system, i.e., $\Delta E = 283 \pm 42$ eV and $\Gamma/2 = 271 \pm 55$ eV. The complex energy shift in kaonic hydrogen is related to the K^-p scattering length through the modified Deser formula [63] (and similarly for kaonic deuterium [64]),

$$\Delta E - i\Gamma/2 = -2\alpha^3\mu_c^2 a_{K^-p}(1 - 2a_{K^-p}\alpha\mu_c(\ln\alpha - 1)), \tag{3.3}$$

where $\alpha \simeq 1/137$ is the fine-structure constant, and μ_c is the reduced mass of the K^-p system. For the discussion of higher-order corrections, see Refs. [65,66]. We note that, recently, a new measurement of the kaonic deuteron system has been performed [67] as well, which, however, is not part of this work. We wish to note that while older values (γ, R_c, R_n) offer very little constraint on the scattering amplitude, the SIDDHARTA results, indeed, do and should, thus, always be taken into account. A dedicated discussion can be found in Ref. [9].

(iii) *AMADEUS:* One of the latest experimental data points was taken by AMADEUS collaboration [68]. Through the analysis of K^- absorption processes on ^{4}He, the modulus of $|f_{0+}^{\pi^-\Lambda\to K^-n}(\sqrt{s} = 1.4\ \text{GeV})|$ was extracted to high precision as 0.334 ± 0.018 fm. This is given in terms of Höhler's partial waves $f_{\ell\pm}$ as

$$f_{0+}^{\pi^-\Lambda\to K^-n} = \frac{1}{\sqrt{2}}\left(-f_{0+}^{\pi^0\Lambda\to K^-p} + f_{0+}^{\pi^0\Lambda\to\bar{K}^0 n}\right). \tag{3.4}$$

IV. EFFECTIVE FIELD THEORY AND UNITARIZED CHIRAL PERTURBATION APPROACH

Lattice QCD provides a systematic way to access QCD Green's functions in the nonperturbative regime. In the

intermediate steps, however, the methodology introduces by construction several approximations to the real world (for a pedagogical introduction, see Ref. [69]). Specifically, the calculation is performed with quarks occupying only intersections of typically cubic and finite-volume lattice in Euclidean space-time (imaginary time). Additionally, a scale needs to be set defining the obtained quantities in physical units, since the computer algorithm does not have a notion of units. Finally, on a more practical side, quarks are often heavier than the physical ones for two reasons: (i) the physical pion appears in nature to be very light, which means very large lattice volumes are required to fit it in, and (ii) systems with heavier-than-physical pions have inelastic thresholds pushed to higher energies, which effectively extends the range of applicability of the existing two- and three-body quantization conditions [24,70,71].

For the present case, scale-setting continuum extrapolation can be assumed to be addressed in the provided finite-volume energy eigenvalues [20,21]. A procedure for the finite-volume mapping including the related breakdown of rotational symmetry is discussed in Sec. II B. What remains is to establish a connection between the heavier-than-physical pion mass results from the lattice with the experimental ones, often referred to as *chiral extrapolation*. As the name suggests, the key point here is to use chiral symmetry to provide guidance on how hadron-hadron interactions behave with the changing pion mass. Specifically, we use CHPT extended to the meson-baryon sector [72–76] to define a three-flavor meson-baryon interaction kernel at leading and next-to-leading order. However, since the energy regime of interest is large, nonperturbative effects are unavoidable. For the explicit calculation and breakdown of the convergence of the perturbative expansion, see, e.g., Ref. [77]. Therefore, the interaction kernel is iterated through a unitarization approach described in the following Sec. IV B. This means that the extrapolation of the model-independent lattice QCD results to the physical point (physical quark masses) is not accomplished through model-independent CHPT but a unitarized, somewhat model-dependent approach. This model dependence of the obtained results is one of the key questions we wish to discuss in this paper.

There is a plethora of approaches aiming to extend the range of applicability of the chiral series to the energy region of the Λ(1405). An in-depth description of those, including their differences and similarities, is provided in the review in [9]. For alternative approaches, see also Refs. [78–82]. To make the model dependence discussion more transparent, we rely here on one class of models described there, one which unites the simplicity of an algebraic formulation (vs., e.g., more sophisticated diagrammatic four-dimensional integral equations of Refs. [33,34]) with the phenomenological flexibility, resulting in a wide range of applications [7,12,83–85].

A. Chiral Lagrangian and interaction kernel

The general form of the chiral meson-baryon Lagrangian is written as an infinite series

$$\mathcal{L}_{\phi B} = \mathcal{L}^{(1)}_{\phi B} + \mathcal{L}^{(2)}_{\phi B} + \mathcal{L}^{(3)}_{\phi B} + \ldots \tag{4.1}$$

of infinitely many terms ordered in Lagrangians with a fixed chiral order denoted above by the superscript. For the specific case of meson-baryon scattering, the leading-order (LO) Lagrangian contains three independent structures,

$$\begin{aligned}\mathcal{L}^{(1)}_{\phi B} = {} & \langle \bar{B}(i\gamma_\mu D^\mu - m_0)B\rangle + \frac{D}{2}\langle \bar{B}\gamma_\mu\gamma_5\{u^\mu, B\}\rangle \\ & + \frac{F}{2}\langle \bar{B}\gamma_\mu\gamma_5[u^\mu, B]\rangle,\end{aligned} \tag{4.2}$$

whereas the next-to-leading-order Lagrangian [86] in its minimal form contains 14 independent structures [87],

$$\begin{aligned}\mathcal{L}^{(2)}_{\phi B} = {} & b_0\langle \bar{B}B\rangle\langle\chi_+\rangle + b_D\langle \bar{B}\{\chi_+, B\}\rangle + b_F\langle \bar{B}[\chi_+, B]\rangle \\ & + b_1\langle \bar{B}[u_\mu, [u^\mu, B]]\rangle + b_2\langle \bar{B}[u_\mu, \{u^\mu, B\}]\rangle + b_3\langle \bar{B}\{u_\mu, \{u^\mu, B\}\}\rangle + b_4\langle \bar{B}B\rangle\langle u_\mu u^\mu\rangle \\ & + i(b_5\langle \bar{B}\sigma^{\mu\nu}[[u_\mu, u_\nu], B]\rangle + b_6\langle \bar{B}\sigma^{\mu\nu}\{[u_\mu, u_\nu], B\}\rangle + b_7\langle \bar{B}\sigma^{\mu\nu}u_\mu\rangle\langle u_\nu B\rangle) \\ & + \frac{ib_8}{2m_0}(\langle \bar{B}\gamma^\mu[u_\mu, [u_\nu, [D^\nu, B]]]\rangle + \langle \bar{B}\gamma^\mu[D_\nu, [u^\nu, [u_\mu, B]]]\rangle) \\ & + \frac{ib_9}{2m_0}(\langle \bar{B}\gamma^\mu[u_\mu, \{u_\nu, [D^\nu, B]\}]\rangle + \langle \bar{B}\gamma^\mu[D_\nu, \{u^\nu, [u_\mu, B]\}]\rangle) \\ & + \frac{ib_{10}}{2m_0}(\langle \bar{B}\gamma^\mu\{u_\mu, \{u_\nu, [D^\nu, B]\}\}\rangle + \langle \bar{B}\gamma^\mu[D_\nu, \{u^\nu, \{u_\mu, B\}\}]\rangle) \\ & + \frac{ib_{11}}{2m_0}(2\langle \bar{B}\gamma^\mu[D_\nu, B]\rangle\langle u_\mu u^\nu\rangle + \langle \bar{B}\gamma^\mu B\rangle\langle [D_\nu, u_\mu]u^\nu + u_\mu[D_\nu, u^\nu]\rangle),\end{aligned} \tag{4.3}$$

where $\langle\ldots\rangle$ denotes the trace in flavor space, $D_\mu B \coloneqq \partial_\mu B + \frac{1}{2}[[u^\dagger, \partial_\mu u], B]$, m_0 is the baryon octet mass in the chiral limit, and D and F are the axial coupling constants. The next-to-leading-order (NLO) low-energy constants (LECs) b_i split into the so-called symmetry breakers $b_{0,D,F}$, parametrizing the explicit chiral symmetry breaking through the nonvanishing quark masses and $\{b_i | i = 1, \ldots, 11\}$, being referred to as dynamical LECs. All external currents except the scalar one are set to zero and

$$U = \exp\left(i\frac{\phi}{F_0}\right), \qquad u^2 \coloneqq U, \qquad u^\mu \coloneqq iu^\dagger\partial^\mu u + iu\partial^\mu u^\dagger,$$
$$\chi_\pm \coloneqq u^\dagger\chi u^\dagger \pm u\chi^\dagger u, \qquad \chi \coloneqq 2B_0\ \mathrm{diag}(m_u, m_d, m_s), \tag{4.4}$$

where F_0 and B_0 denote the pion decay constant and the constant related to the quark condensate in the chiral limit, respectively. The ground state octet mesons (Goldstone bosons of the theory) and baryons are included through

$$\phi = \sqrt{2}\begin{pmatrix} \frac{\pi^0}{\sqrt{2}} + \frac{\eta}{\sqrt{6}} & \pi^+ & K^+ \\ \pi^- & -\frac{\pi^0}{\sqrt{2}} + \frac{\eta}{\sqrt{6}} & K^0 \\ K^- & \bar{K}^0 & -\frac{2}{\sqrt{6}}\eta \end{pmatrix}, \qquad B = \begin{pmatrix} \frac{\Sigma^0}{\sqrt{2}} + \frac{\Lambda}{\sqrt{6}} & \Sigma^+ & p \\ \Sigma^- & -\frac{\Sigma^0}{\sqrt{2}} + \frac{\Lambda}{\sqrt{6}} & n \\ \Xi^- & \Xi^0 & -\frac{2}{\sqrt{6}}\Lambda \end{pmatrix}. \tag{4.5}$$

The above general Lagrangian defines all the Feynman diagrams, as shown in Ref. [77], calculating meson-baryon scattering in three-flavor CHPT. The completeness of momentum structures plays a crucial role, for instance, when constructing unitary gauge-invariant models for meson photoproduction [88–90], and warrants full accounting of all chiral logarithms. This may indeed become relevant when approaching the chiral limit, as discussed and shown in Ref. [91]. It was shown, however, in Ref. [34] that for antikaon-nucleon scattering in the physical region not too far from the two-body thresholds, such effects are subdominant. An approach neglecting such effects was studied in Ref. [50] and later including coupled-channel S- and P-waves in Ref. [35].

Instead of this path, we proceed here with a closely related but computationally less expensive approach. It relies on calculating the chiral potential V and iterating it to restore two-body unitarity. We use the normalization of Refs. [12,85] and study three types of meson-baryon potentials,

$$\mathrm{M1}:\ V_{\alpha\beta}(s) = V^{\mathrm{WT}}_{\alpha\beta}(s), \tag{4.6}$$

$$\mathrm{M2}:\ V_{\alpha\beta}(s) = V^{\mathrm{WT}}_{\alpha\beta}(s) + V^{\mathrm{BORN}s}_{\alpha\beta} + V^{\mathrm{BORN}u}_{\alpha\beta}(s), \tag{4.7}$$

$$\mathrm{M3}:\ V_{\alpha\beta}(s) = V^{\mathrm{WT}}_{\alpha\beta}(s) + V^{\mathrm{BORN}s}_{\alpha\beta} + V^{\mathrm{BORN}u}_{\alpha\beta}(s) + V^{\mathrm{NLO}}_{\alpha\beta}(s), \tag{4.8}$$

where α/β collect the indices of the in/outgoing meson-baryon states $\mathcal{S}$. Here, WT denotes the time-honored Weinberg-Tomozawa term and BORNx (x=u, s) the s- and u-channel Born terms, respectively. Specifically, for the total strangeness $S = -1$, the relevant channels are listed in (2.7). All potentials except $V^{\mathrm{NLO}}_{\alpha\beta}(s)$ are obtained from the LO chiral Lagrangian Eq. (4.2), while the latter is deduced from the relevant part of the NLO Lagrangian,

$$\begin{aligned}\mathcal{L}^{(2)}_{\phi B} = {} & b_0\langle\bar{B}B\rangle\langle\chi_+\rangle + b_D\langle\bar{B}\{\chi_+, B\}\rangle + b_F\langle\bar{B}[\chi_+, B]\rangle \\ & + d_1\langle\bar{B}\{u_\mu, [u^\mu, B]\}\rangle + d_2\langle\bar{B}[u_\mu, \{u^\mu, B\}]\rangle \\ & + d_3\langle\bar{B}u_\mu\rangle\langle Bu^\mu\rangle + d_4\langle\bar{B}B\rangle\langle u_\mu u^\mu\rangle.\end{aligned} \tag{4.9}$$

It is notable that only the potentials in M2 and M3 include all terms at the given chiral order, namely, leading and next-to-leading, respectively. Still, in the M1 potential, the so-called Weinberg-Tomozawa term already captures the major aspects of the dynamics of the system correctly, but is at odds with the most recent threshold data [62] even after the unitarization procedure, see, e.g., Ref. [12], or to foreshadow the results discussed later, see M1SxP fits in Fig. 7.

Explicitly,[2] the above required potentials read as

[2]These formulas are quite standard in the literature. However, a certain amount of typos and convention inconsistencies also became standard. To avoid this, explicit formulas are provided here.

$$
\begin{aligned}
V^{\mathrm{WT}}_{(ai)(bj)}(s) &= -\frac{\mathcal{N}_a\mathcal{N}_b}{8F_iF_j}C^{\mathrm{WT}}_{(ai)(bj)}(2\sqrt{s}-m_a-m_b),\\
V^{\mathrm{BORNs}}_{(ai)(bj)}(s) &= \frac{\mathcal{N}_a\mathcal{N}_b}{12F_iF_j}\sum_{c=1}^{8}C^{[DF]}_{(bj)(c)}C^{[DF]}_{(ai)(c)}\frac{1}{\sqrt{s}+m_c}(s-\sqrt{s}(m_a+m_b)+m_am_b),\\
V^{\mathrm{BORNu}}_{(ai)(bj)}(s) &= -\frac{\mathcal{N}_a\mathcal{N}_b}{12F_iF_j}\sum_{c=1}^{8}C^{[DF]}_{(ic)(b)}C^{[DF]}_{(jc)(a)}\left[\sqrt{s}+m_c-\frac{(m_a+m_c)(m_b+m_c)}{2\mathcal{N}_a^2\mathcal{N}_b^2}(\sqrt{s}+m_a+m_b-m_c)\right.\\
&\quad+\left(\sqrt{s}+m_c-m_a-m_b-\frac{s+m_c^2-M_i^2-M_j^2-2E_aE_b}{2\mathcal{N}_a^2\mathcal{N}_b^2}(\sqrt{s}+m_a+m_b-m_c)\right)\\
&\quad\left.\times\frac{(m_a+m_c)(m_b+m_c)}{4p_{bj}p_{ai}}\ln\left(\frac{s+m_c^2-M_i^2-M_j^2-2E_aE_b-2p_{bj}p_{ai}}{s+m_c^2-M_i^2-M_j^2-2E_aE_b+2p_{bj}p_{ai}}\right)\right],\\
V^{\mathrm{NLO}}_{(ai)(bj)}(s) &= \frac{\mathcal{N}_i\mathcal{N}_j}{F_iF_j}\left(C^{[b_0b_Db_F]}_{(ai)(bj)}-2C^{[d_1d_2d_3d_4]}_{ij}\left(E_iE_j+\frac{p_{bj}^2p_{ai}^2}{3\mathcal{N}_a^2\mathcal{N}_b^2}\right)\right).
\end{aligned}
\tag{4.10}
$$

Here, we have explicitly written out the baryon/meson octet indices $\{a,b,c\}/\{i,j\}$ of the corresponding channel. Further, s is the total energy squared, $\mathcal{N}_a=\sqrt{m_a+E_a}$, $E_a=\sqrt{m_a^2+p_{ai}^2}$, $E_i=\sqrt{M_i^2+p_{ai}^2}$, and $p_{ai}=\sqrt{(s-(M_i+m_a)^2)(s-(M_i-m_a)^2)}/(2\sqrt{s})$. Meson and baryon masses are denoted by M and m, respectively. The coefficient matrices C^{WT}, $C^{[DF]}$, $C^{[b_0b_Db_F]}$, and $C^{[d_1d_2d_3d_4]}$ are obtained from Eq. (4.9) but can also be obtained from the Appendix of Ref. [85]. The first matrix contains the LECs $F_{\pi,K,\eta}$, which appear explicitly in the denominator, while the latter three matrices include additional LECs, with the pertinent parameters put into the superscript square brackets, for convenience. Note that the leading-order LECs D,F are fixed, and only the b_i,d_i are to be determined by the fits. Additionally, $C^{[b_0b_Db_F]}$ depends explicitly on the quark masses, given in terms of the meson masses.

B. Unitarization procedure and connection to observables

With the interaction kernel at hand, a nonperturbative amplitude can be constructed. This typically involves some sort of resummation of an infinite set of diagrams. Usually guided by the S-matrix unitarity, typical methods are the full four-dimensional Bethe-Salpeter, three-dimensional reduced Lippmann-Schwinger equations, N/D, or other dispersive tools. Using the above defined on-shell potentials projected to the S-wave in Eq. (4.10), the Bethe-Salpeter integral equation indeed reduces to an algebraic matrix equation (with respect to the channel space $\mathcal{S}$),

$$
\begin{aligned}
T(s) &= -V(s)+T(s)G(s)V(s) = -V(s)-V(s)G(s)V(s)\\
&\quad -V(s)G(s)V(s)G(s)V(s)-\cdots\\
&= -V(s)\frac{\mathbb{1}}{1-V(s)G(s)}.
\end{aligned}
\tag{4.11}
$$

The infinite series on the right-hand side of the first line is written out to show the connection to an infinite set of loop diagrams. Clearly, this set is still incomplete compared to all possible diagrams in CHPT to all orders. This is one of the sources of the model dependence acquired in this step. For further details, see the dedicated review in [9].

The meson-baryon one-loop (channel α) function is defined as

$$
G_\alpha(s)=\int\frac{d^4l}{(2\pi)^4}\frac{i}{(l^2-M_\alpha^2+i\epsilon)((P-l)^2-m_\alpha^2+i\epsilon)},
\tag{4.12}
$$

which has an imaginary part $\mathrm{Im}\,G_\alpha(s)=-p_\alpha/(8\pi\sqrt{s})$. Therefore, the T-matrix, indeed, automatically fulfills the partial-wave unitarity $\mathrm{Disc}\,T(s)=ip_\alpha/(4\pi\sqrt{s})|T(s)|^2$ for energy between $s=(m_\alpha+M_\alpha)^2$ and the next higher two-body threshold. For an introductory discussion of the S-matrix theory for hadron spectroscopy, see the review in [92]. This also allows one to relate the T-matrix to the K-matrix form used in Sec. II B. In terms of the Höhler partial wave [36,37] f_{0+} relevant for this study [cf. Eq. (2.3)],

$$
f_{0+}(s)=\frac{1}{8\pi\sqrt{s}}T(s),\qquad f_{0+}(s)=\frac{1}{\tilde{K}_E^{-1}(s)-ip}.
\tag{4.13}
$$

Here, all quantities are matrices with respect to the channel space, i.e., $\tilde{K}_E\in\mathbb{R}^{\mathcal{S}\times\mathcal{S}}$ and $p\coloneqq\mathrm{Diag}\{p_\alpha|\alpha\in\mathcal{S}\}$. The above nomenclature allows for straightforward relations to the observables. For example, the scattering length is simply given by $a=f_{0+}((m+M)^2)$ or total cross sections, as shown in Eq. (3.1).

C. Regularization schemes

The four-dimensional meson-baryon loop integral G is log-divergent and can be tamed in various ways using, e.g., a momentum cutoff or dimensional regularization. In the latter, and most frequently utilized form [7,12,84,85,93,94], the loop function reads ($\alpha \in \mathcal{S}$)

$$G_\alpha(\sqrt{s}) = a_\alpha + \frac{1}{32\pi^2}\left(\log\left(\frac{m_\alpha^2}{\mu^2}\right) + \log\left(\frac{M_\alpha^2}{\mu^2}\right) - \frac{m_\alpha^2 - M_\alpha^2}{s}\log\left(\frac{M_\alpha^2}{m_\alpha^2}\right) - 2 - \frac{8p_\alpha}{\sqrt{s}}\operatorname{arctanh}\left(\frac{2\sqrt{s}p_\alpha}{(m_\alpha + M_\alpha)^2 - s}\right)\right). \tag{4.14}$$

For the analysis of the experimental data, all masses are taken to their physical values, while the regularization scale dependence is moved into the subtraction constants a_α channel-by-channel for a fixed scale μ. Note that this is the equivalent of promoting the regularization scale μ to channel-by-channel μ_α [34]. Since isospin breaking effects are far smaller than the available experimental precision, no distinction is made between subtraction constants in the same particle type, leaving one with six free subtraction constants $\{a_{\bar{K}N}, a_{\pi\Lambda}, a_{\pi\Sigma}, a_{\eta\Lambda}, a_{\eta\Sigma}, a_{K\Xi}\}$, which are treated commonly as additional free parameters of the theory. Note that at the lattice point, isospin symmetry is exact and input is available for $I = 0$ only. There, only four subtraction constants matter corresponding to the channels in Eq. (2.8).

Besides the choice of the resummation procedure and the choice of the interaction potential, there is yet another issue where a choice has to be made, namely, the regularization procedure, which is also leading to systematic uncertainties in the UCHPT approach. In view of the recent experimental and more importantly lattice QCD progress, the main phenomenological drawback of this is that by losing connection to the usual perturbative chiral expansion, the LECs cannot be compared easily between different approaches or to the perturbatively determined values. More importantly, chiral extrapolations of the amplitudes from unphysical (lattice QCD) to physical quark masses will differ from one approach to another, which was already observed in Ref. [95]. Specifically, in contrast to the LECs, it is not clear how the subtraction constants depend on the quark masses since they absorb higher-order terms.

So far, removing the model dependence from these approaches entirely seems rather unrealistic. Thus, one cannot escape the imperative of quantifying how these above choices reflect themselves on observables or on obtained predictions, such as resonance pole positions or chiral extrapolations of the amplitudes. Therefore, in addition to the various choices of the interaction kernel, we employ three types of regularization schemes widely used in the literature:

(S1) No assumption about the quark mass dependence of the subtraction constants. For each available quark mass setup and for fixed $\mu = 1$ GeV, we fit a new set $\{a_\alpha\}$ to the available data. Through this, no extrapolation is possible, but the maximal possible freedom of the model is achieved. Note that seven LECs are still quark mass independent.

(S2) As proposed in Refs. [84,96], one fixes the subtraction constants by demanding

$$T(\sqrt{s} = m) = V(\sqrt{s} = m) \Leftrightarrow G(\sqrt{s} = m, a(\mu)) = 0. \tag{4.15}$$

This was recently employed in Ref. [95] and boils down to

$$a_\alpha = -\frac{1}{32\pi^2}\left(\log\left(\frac{m_\alpha^2 M_\alpha^2}{\mu^4}\right) - \frac{m_\alpha^2 - M_\alpha^2}{s}\log\left(\frac{M_\alpha^2}{m_\alpha^2}\right) - 2 - \frac{8p_\alpha}{\sqrt{s}}\operatorname{arctanh}\left(\frac{2\sqrt{s}p_\alpha}{(m_\alpha + M_\alpha)^2 - s}\right)\right)\Bigg|_{\sqrt{s}=m_p,\mu=m_\alpha}. \tag{4.16}$$

Technically, this scheme is advantageous by reducing the number of free parameters, while connecting at the same time the lattice point (unphysical quark masses) with the physical ones.

(S3) Another scheme was proposed in Ref. [93]. Similarly to S2, it sets a constraint on the loop function but at a different matching point. In particular, it is imposed that at the two-body threshold the dimensionally and cutoff (hard cutoff Λ) regularized loop functions are identical. After matching the different expressions of the loop functions, this boils down to

$$a_\alpha = \frac{1}{16\pi^2}\left(1 - \frac{2}{M_\alpha + m_\alpha}\left(m_\alpha \log\left(1 + \sqrt{1 + \frac{m_\alpha^2}{\Lambda^2}}\right) + M_\alpha \log\left(1 + \sqrt{1 + \frac{M_\alpha^2}{\Lambda^2}}\right)\right) + \log\left(\frac{\mu^2}{\Lambda^2}\right)\right). \tag{4.17}$$

We fix again $\mu = 1$ GeV, but fit a common channel-independent parameter Λ for either lattice, experimental, or both points simultaneously.

In summary, the regularization scheme S1 makes no assumptions about the quark mass dependence of the subtraction constants but defines six free parameters (a's) per quark mass setup, and lacks predictive power outside of the fitted quark mass regions. Schemes S2 (no free parameters) and S3 (one free parameter), on the other hand, make a certain assumption about the form of the loop integrals resulting in a higher predictive power also at other than fitted quark mass scenarios. We note that the S1 scheme is similar/equivalent to fitting regularization scales

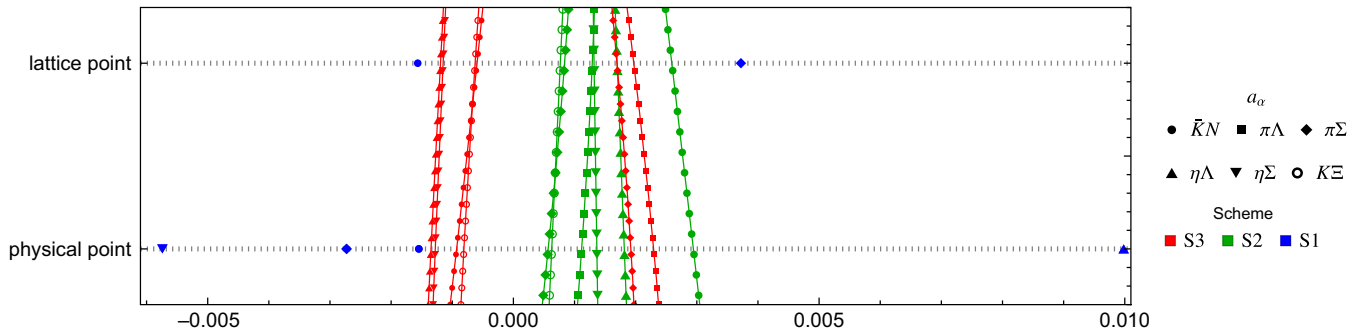

FIG. 4. Comparison of subtraction constants obtained from global fits using different regularization schemes (S1, S2, and S3) at different quark masses. Scheme S1 only provides values at the given quark masses obtained from global fits F_{17} (blue). S2 and S3 type subtraction constants are per construction pion mass dependent.

[97,98] that can be matched to those used in dimensional regularization, see, e.g., Eq. (2.13) in [99].

We will confront each scheme with the lattice and experimental data below. The resulting subtraction constants of the best fits to combined lattice and experimental data are collected as a function of the hadron masses extrapolated linearly ($m = x m_{\rm phys} + (1-x) m_{\rm latt}$ for any generic hadron mass m and $x \in [0,1]$) between the physical and lattice points in Fig. 4. We observe that S3 and S2 have a similar order of magnitude of the determined constants, while most of the fitted constants (scheme S1) are, indeed, substantially larger. Among different variations of the scheme S1 fits (different starting points of the fits), we observe some clustering in a few cases, but mostly the obtained values are very uncertain. This indicates that either S1 has too many/redundant parameters or the data are not allowing to fix them uniquely due to possible inconsistencies. For further details, see Sec. V C.

D. Synthesis and evaluation of the UCHPT framework

The considered approach is based on CHPT in such a way that it matches CHPT amplitudes at the leading and next-to-leading orders, when projecting to the S-wave. It captures part of the nonperturbative dynamics of the full CHPT to all orders but depends on the way the truncation of higher orders is made. This results in a certain model dependence, which is quantified in this work by varying the following:

(i) Truncation order of the interaction kernel: M1$[F_\pi, F_K, F_\eta]$, M2$[F_\pi, F_K, F_\eta, D, F]$, and M3$[F_\pi, F_K, F_\eta, b_0, b_d, b_f, d_1, d_2, d_3, d_4]$. The free parameters are given in the square brackets, and these are the quark-mass-independent LECs. Note that the leading-order LECs are kept fixed as $D = 0.8$, $F = 0.46$, and $F^{\rm phys}_{\pi,K,\eta} = \{92.4, 110.0, 118.8\}$ MeV and $F^{\rm latt}_{\pi,K,\eta} = \{93.2, 108.2, 121.1\}$ MeV.

(ii) Regularization scheme: S1$[a_1, a_2, a_3, a_4, a_5, a_6]$, S2$[-]$, and S3$[\Lambda]$. The free parameters are listed in the square brackets. Note that Λ is quark mass independent while the a's need to be fitted per quark mass setup. At the unphysical point we have only four $[a_1, a_3, a_4, a_6]$ because only the isoscalar channel is available.

(iii) Data: We will study if new lattice results [20,21] (a) allow to fix the parameters of the models by themselves, making reliable predictions for the physical point, and (b) are consistent with experimental data. Here, various combinations of lattice QCD and/or experimental results will be used to fit the free parameters described before.

Finally, we wish to discuss another yet mostly ignored limitation of the this and all current UCHPT approaches with respect to the intermediate three-body states. Specifically, in meson-baryon systems, processes such as $\pi\Sigma \to \Lambda$ are allowed. Thus, an initial meson-baryon system can couple to the meson-meson-baryon state in the intermediate step, e.g., $\pi\Sigma \to \pi\pi\Lambda \to \pi\Sigma$, etc. Technically, this leads to new singularity structures [9,92] violating the simple unitarity condition spelled out before in Eq. (4.12).

There are several types of new singularities. Most prominently, there is the *right-hand cut*, occurring when the total energy is sufficient or higher than the sum of the masses of all three particles in question, e.g., $s \geq (2M_\pi + m_\Lambda)^2$. The positions of the branch points of these cuts are depicted as red dashed lines in the right panel of Fig. 5, including physical and unphysical (the one employed by BaSc collaboration [20,21], $M_\pi \approx 200$ MeV) quark mass scenarios. One observes clearly that the $\pi\pi\Lambda$ cut indeed is far above the estimated pole positions of $\Lambda(1405)$ when unphysical quark masses are employed. However, extrapolating down to the physical point, this cut starts at lower energies and ultimately is just between the estimated pole positions of the $\Lambda(1380)$ and the $\Lambda(1405)$. Thus, one cannot avoid the conclusion that the position of the latter state determined in the literature must carry a systematic, yet unknown uncertainty related to the neglected three-body states. Besides such phenomenological implications, this will also play a crucial role in future physical point lattice QCD simulations. The development

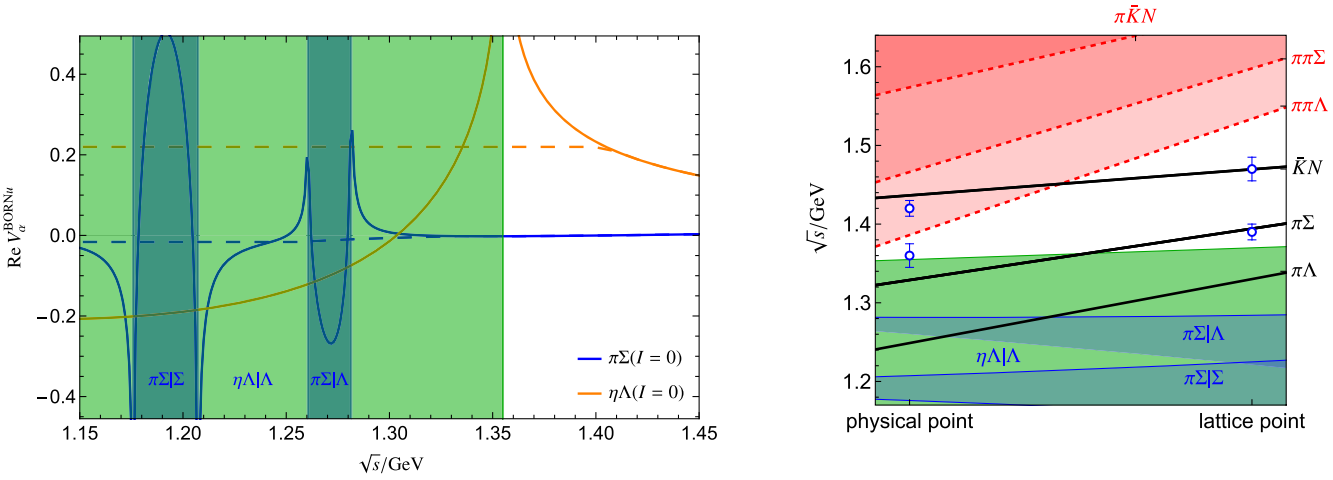

FIG. 5. Three-body-related singularities for the physical and unphysical quark mass setups. Left: singularities of the u-channel Born diagram in Eq. (4.10) projected to $I = 0$ for the initial/final states, as specified in the legend for physical quark masses. Long-dashed lines represent the potential implemented in the UCHPT amplitude mitigating the appearance of u-channel left-hand cuts. Right: relevant short left-hand cut associated with the u-channel exchange (green, blue areas), cf. left figure. Black solid and red dashed lines denote the position of the right-hand cut branching points with respect to two- and three-body states, respectively. The energy region with no allowed three-body on-shell states is the remaining white area. Blue dots with error bars denote the averaged result from the global analysis discussed in Sec. VI.

of pertinent tools, such as three-body scattering amplitudes and three-body quantization conditions, has progressed strongly over the last few years [100] but will need another update in the future. Some steps in this direction were made recently for the similar case of the $\pi\pi N$ channel in relation to the Roper resonance, see Ref. [101] and references therein.

The exchange of a baryon in the u-channel also leads to the occurrence of the left-hand cut or, more specifically, the baryon short left-hand cut (sometimes called the short baryon cut). For an in-depth discussion of such cuts, see Ref. [102]. Recently, studies of this type of singularities also became quite popular in the context of heavy meson scattering, such as DD^* or BB^*. The reason is that the left-hand cut lies there (in particular) for the unphysical pion mass scenarios on the lattice close to the two-body threshold, see, e.g., Refs. [103–108]. Thus, not accounting for the left-hand cut leads to problems most apparent when dealing with the finite-volume lattice QCD spectrum, see, e.g., [109–111]. For $S = -1$, the short left-hand cut occurs through, e.g., Λ or Σ exchange in the $\pi\Sigma \to \pi\Sigma$ transition, referred to as $\pi\Sigma|\Lambda$ and $\pi\Sigma|\Sigma$. Another example relevant for the isoscalar channel is $\eta\Lambda|\Lambda$. Indeed, such transitions are included in the UCHPT models (M2 and M3) via the chiral potential $V^{\mathrm{BORN}u}$ from Eq. (4.10). For a general transition $\phi_1 B_1 \to \phi_2 B_2$ including u-channel exchange of a baryon B_x, the limits of the singular region are given by

$$s = \frac{1}{2m_x^2}\Big(M_1^2M_2^2 - M_2^2m_2^2 + M_1^2m_x^2 + M_2^2m_x^2 + m_2^2m_x^2 - m_x^4 + m_1^2(-M_1^2 + m_2^2 + m_x^2), \tag{4.18}$$

$$\pm\sqrt{(m_1^4 + (M_2^2 - m_x^2)^2 - 2m_1^2(M_2^2 + m_x^2))(M_1^4 + (m_2^2 - m_x^2)^2 - 2M_1^2(m_2^2 + m_x^2))}\Big). \tag{4.19}$$

For $I = 0$ transitions, this is depicted in the left panel of Fig. 5 by the shaded regions. There, one clearly sees that the chiral potential (the real part is plotted), indeed, has singularities in the shaded region. On the right, the same critical regions are depicted as a function of the quark mass extrapolated from the physical to the lattice point. We note that in the $\pi\Sigma$ channel, this occurs at rather small energies, well below the region of interest for the $\Lambda(1380)$ and $\Lambda(1405)$. However, Λ exchange in the $\eta\Lambda \to \eta\Lambda$ transition is only slightly below the $\Lambda(1380)$ bound state at the lattice point. Ultimately, this leads to a complex-valued K-matrix, Eq. (4.13), invalidating a simple application of Lüscher's quantization condition. Practically, in the current state-of-the-art of the coupled-channel UCHPT models, this is avoided by replacing the potential slightly above the critical region by a constant. The modified and used one-baryon exchange potential is depicted by the long-dashed line in the left panel of Fig. 5. So far, the coverage and precision of

experimental as well as lattice results is not sensible to these effects. However, in the long run, we expect that an extension of modern three-body formalisms like FVU [71] or RFT [70] to such cases will be a better choice. These have been shown recently of being capable of dealing with strangeness channels [112–114], dealing with left-hand cuts [110], and extracting resonance pole positions for three-body states [115–119] from experimental and lattice QCD spectra.

V. ANALYSIS

A. Pilot study: Finite-volume spectrum from UCHPT and experiment

Before fitting the free parameters of the models, we wish to check if the finite-volume spectrum obtained from available models already matches the lattice QCD spectrum [20,21]. Specifically, we consider contemporary models of next-to-leading chiral order, including diagrammatic or potential unitarization formalisms [12,35,50]. These models, referred to as $\mathrm{UCHPT}_{\mathrm{NLO}}$, represent a fair spread (including M3 type models) of assumptions made in the derivation, sampling qualitatively possible model dependence, as discussed in Sec. IV. We also include M1 ($\mathrm{UCHPT}_{\mathrm{WT}}$) and M2 ($\mathrm{UCHPT}_{\mathrm{LO}}$) type models available from Ref. [12]. All considered models rely on the scheme S1 with subtraction constants a_α assumed to be quark mass independent. All considered models describe at least the experimental data compiled in Sec. III with similar quality ($\chi^2_{\mathrm{dof}} \approx 1$).

The finite-volume spectrum is predicted through the Lüscher formalism [24,25] implemented as discussed in Sec. II B. The central values of the predicted energy eigenvalues in relevant irreps are depicted in Fig. 6 together with the lattice QCD results. We observe that (ignoring correlations at the moment), for the most part, all NLO but also WT and LO models agree with the provided spectrum. There are, however, stark exceptions to this observation, like the second and third levels of G_{1u} where some NLO models predict a different finite-volume spectrum. Further examples are the third level of the $G(3)$ irrep or the fourth lowest level of the $G(1)$ irrep, which do not agree with either of the model predictions. It is noteworthy that the spread of the predictions for the NLO models is indeed expected since these models provide a better description of the experimental data for the price of larger numbers of free parameters. Their predictions vary stronger than those of the WT or LO models.

Overall, we cannot escape the conclusion that new precise lattice results will provide an important constraint on the models.

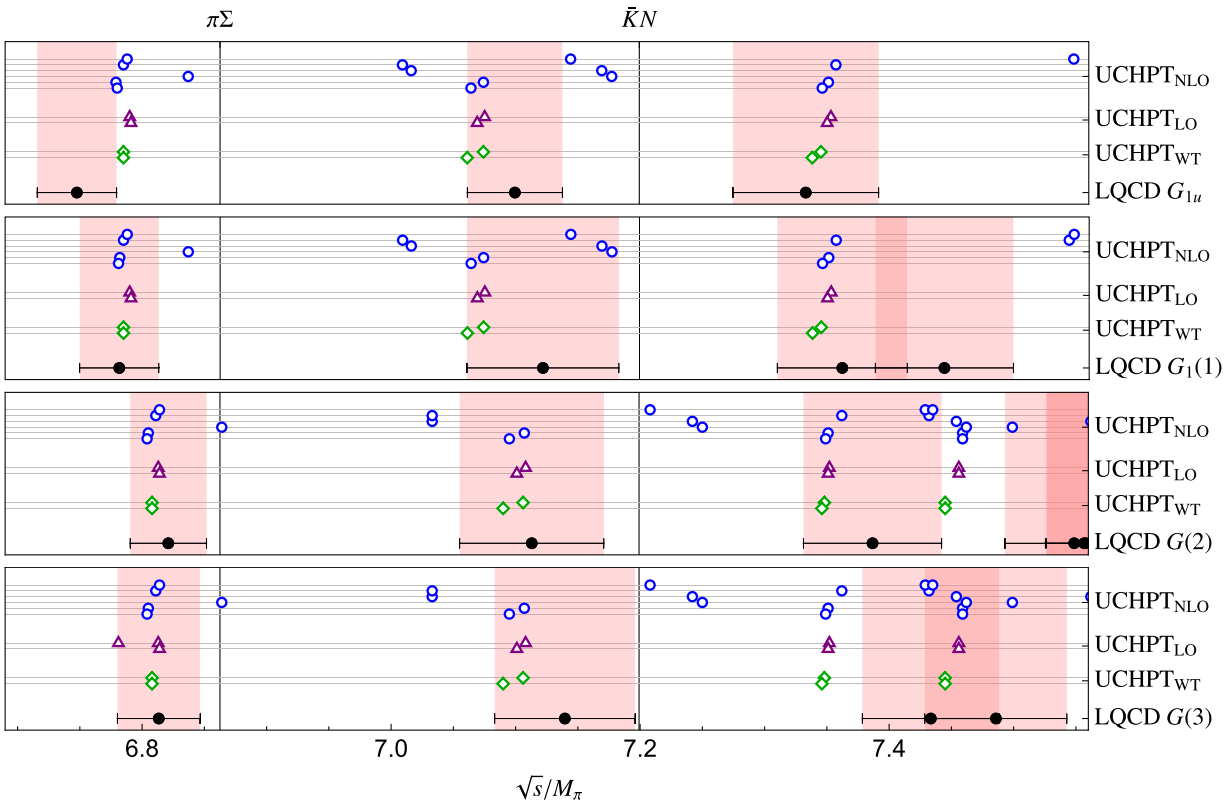

FIG. 6. Fit-free prediction of the finite-volume spectrum relying on the contemporary WT (M1), LO (M2), and NLO type UCHPT models [12,35,50]. Pink vertical bands show the lattice QCD results [20,21] for relevant irreps: G_{1u}, $G_1(1)$, $G(2)$, and $G(3)$.

B. Fit details: Loss function and degrees of freedom

Stemming from quite different time periods and being results of vastly different experimental techniques, the quality of the experimental data summarized in Sec. III is very different. More so if one considers combined analysis of lattice QCD finite-volume spectra (Sec. II) as adequate input for the UCHPT fits. Thus, a simple χ^2 statistic as a measure of fit quality is not sufficient and modifications are in order.

As an example, consider one of the most modern experimental data inputs, the energy shift and width of the kaonic hydrogen, in comparison with the oldest data available, the total cross sections for the $K^- p \to MB$. The former consists of only two quantities measured at 10–20% accuracy at the $K^- p$ threshold. The latter data include 252 data points at a few 10's% statistical uncertainty depending on the channel and the kinematics, which also carries considerable systematic uncertainties due to bin sizes and possible inconsistencies of the data. Using traditional χ^2 definition aggregating both sources together would, thus, simply make the modern SIDDHARTA data entirely insignificant despite its superior quality. Lattice finite-volume spectra consist also of only 14 points and, thus, would appear as an insignificant contribution to the total χ^2. In such cases of asymmetric data distribution among different observables, a weighted χ^2 definition is more customary,

$$\chi^2_{\rm dof} = \frac{\sum_a N_a}{A((\sum_a N_a) - N_{\rm par})}\chi^2_{\rm wt}$$

$$\text{with} \quad \chi^2_{\rm wt} = \sum_{a=1}^{A} \frac{\chi^2_a}{N_a}$$

$$\text{with} \quad \chi^2_a = \sum_{n=1,m=1}^{N_a} (f^a_n(\overrightarrow{\aleph}) - \hat{f}^a_n)[\hat{C}^{-1}_a]_{nm}(f^a_m(\overrightarrow{\aleph}) - \hat{f}^a_m). \tag{5.1}$$

Here, we denote with a/A the index/number of observables, and $\overrightarrow{\aleph}$ is the parameter vector of the model. Its size $N_{\rm par}$ can be read off from Fig. 7. n/N_a is the index/number of data in

Fit	UCHPT type	$N_{\rm data\|exp.+lat.+m}$	$N_{\rm par.}$	$\chi^2_{\rm dof}$	AIC	BIC
F_{19}	M1S1L	$0+14+0$	3	1.36	7.4	9.3
F_{31}	M1S2L	$0+14+0$	0	2.89	2.9	2.9
F_{18}	M1S3L	$0+14+0$	1	4.42	6.4	7.1
F_{20}	M2S1L	$0+14+0$	3	1.42	7.4	9.3
F_{32}	M2S2L	$0+14+0$	0	2.68	2.7	2.7
F_{25}	M2S3L	$0+14+0$	1	3.54	5.5	6.2
F_{01}	M3S1L	$0+14+4$	10	0.96	21.0	29.9
F_{15}	M3S2L	$0+14+4$	7	0.90	14.9	21.1
F_{10}	M3S3L	$0+14+4$	8	0.92	16.9	24.0
F_{21}	M1S1P	$258+0+0$	6	4.23	16.2	37.5
F_{28}	M1S2P	$258+0+0$	0	25.58	25.6	25.6
F_{27}	M1S3P	$258+0+0$	1	30.28	32.3	35.8
F_{22}	M2S1P	$258+0+0$	6	8.87	20.9	42.2
F_{29}	M2S2P	$258+0+0$	0	48.16	48.2	48.2
F_{26}	M2S3P	$258+0+0$	1	18.69	20.7	24.2
F_{30}	M3S1P	$258+0+0$	16	1.51	33.5	90.4
F_{13}	M3S2P	$258+0+0$	7	1.85	15.8	40.6
F_{11}	M3S3P	$258+0+0$	8	1.50	17.5	45.9
F_{24}	M1S3PL	$258+14+0$	1	27.56	29.6	33.2
F_{23}	M2S3PL	$258+14+0$	1	17.82	19.8	23.4
F_{17}	M3S1PL	$258+14+4$	16	1.44	33.4	91.4
F_{16}	M3S2PL	$258+14+4$	7	2.11	16.1	41.5
F_{12}	M3S3PL	$258+14+4$	8	2.23	18.2	47.2

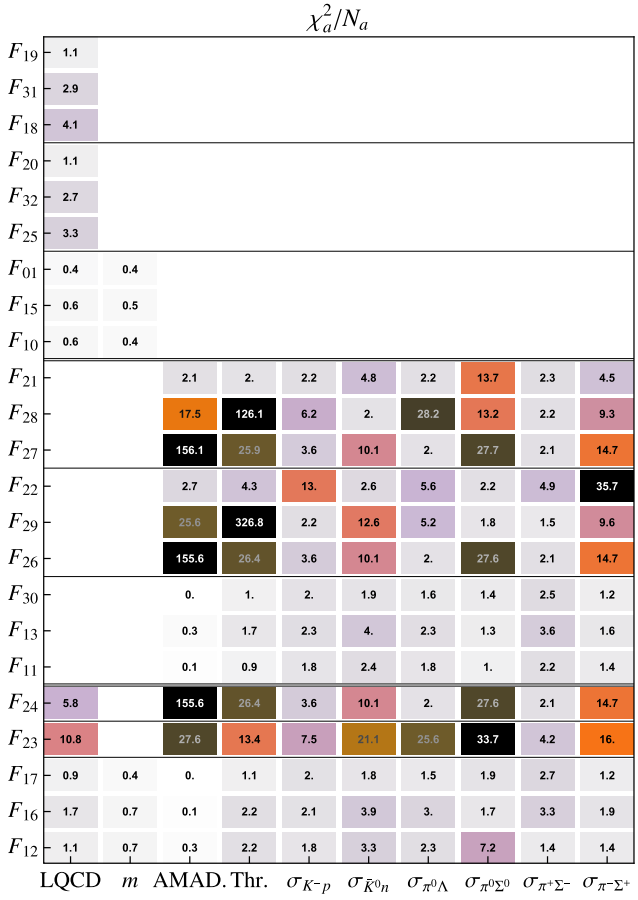

FIG. 7. Left: summary of the fit results minimizing $\chi^2_{\rm dof}$ while using various model types, regularization schemes, and data subsets. The last two columns show AIC and BIC values from Eq. (5.2), where results with large $\chi^2_{\rm dof}$ are grayed out. Right: minimized χ^2 from fits in the table left-hand side, separated by the data type normalized by the number of data in that observable. Here, "LQCD," "AMAD," and "Thr." refer to lattice, AMADEUS, and threshold data discussed in Secs. II and III.

the data type a, $f^a/\hat{f}^a$ is the model/datum result of the corresponding observable type a, and $\hat{C}$ is the covariance matrix of the data. Note that in most cases, except lattice QCD, the latter is simply provided by a diagonal matrix of the form $[\hat{C}_a]_{nm} = \delta_{nm}(\hat{\sigma}_n^a)^2$, where $\hat{\sigma}_n^a$ is the error for each datum $\hat{f}_n^a$. The total number of data is denoted by $N_{\text{data}} = \sum_a N_a$.

The above χ^2_{dof} is minimized in the fit with respect to k parameters. However, given the various choices of interaction kernel (M1, M2, and M3) and regularization scheme (S1, S2, and S3), this analysis is both a *parameter estimation* and *model comparison* problem. Comparing models with different parameters should involve penalizing models with more parameters.

A full model comparison would involve the estimation of Bayes factors via Markov chain Monte Carlo which, given the number of parameters of interest, would be too computationally expensive with the current code. A crude model comparison may be effected using an *information criterion* that attempts to balance goodness of fit against model complexity (see, for example, [120] for an example in an adjacent research area). Such criteria make use of the (log) maximum likelihood, with some adjustment for the number of parameters and size of the dataset. We use the Akaike information criterion (*AIC*) [121] and the Bayes information criterion [122] (*BIC*), but we note that care must be taken in interpreting the numbers calculated for *AIC*/*BIC* too seriously, and we use them only as a guide for revealing gross features.

For a given maximum log-likelihood $\log L_{\max}$, the information criteria are defined as

$$AIC = -2\log L_{\max} + 2N_{\text{par}}$$
$$\text{and} \quad BIC = N_{\text{par}}\log N_{\text{data}} - 2\log L_{\max}. \tag{5.2}$$

Comparing *AIC*/*BIC* values for different models is only valid for fits to the same data points, but if this condition is true then the differences in *AIC* or *BIC* values between models can be related to the relative probability of a model being true. In our case, we use the χ^2_{dof}, as defined in Eq. (5.1) as $-2\log L_{\max}$, and values are displayed in Fig. 7. There, results for fits with too large χ^2_{dof} are grayed out and, furthermore, sensible comparisons between different models can only be made for fits with an equal number of data.

C. Fit discussion

subsec:fit-discussion Following the description of the χ^2_{dof} analysis, this section provides additional technical details of the fitting procedures used in this work. In the fits, subtraction constants and LECs will be constrained using the two-hadron interacting spectrum and experimental quantities. In addition, the parameters, related to the explicit chiral symmetry breaking b_0, b_D, and b_F, can be constrained using the lattice QCD estimation of single baryon masses provided by BaSc collaboration [20]. The NLO CHPT formulas for the baryon masses read as follows [87,123]:

$$m_N = m_0 - 2(b_0 + 2b_F)M_\pi^2 - 4(b_0 + b_D - b_F)M_K^2, \tag{5.3}$$

$$m_\Lambda = m_0 - \frac{2}{3}(3b_0 - 2b_D)M_\pi^2 - \frac{4}{3}(3b_0 + 4b_D - b_F)M_K^2, \tag{5.4}$$

$$m_\Sigma = m_0 - 2(b_0 + 2b_D)M_\pi^2 - 4b_0 M_K^2, \tag{5.5}$$

$$m_\Xi = m_0 - 2(b_0 - 2b_F)M_\pi^2 - 4(b_0 + b_D + b_F)M_K^2, \tag{5.6}$$

where the low-energy constants b_0, b_D, and b_F have been discussed before, and m_0 is the baryon octet mass in the chiral limit. In practice we avoid fitting m_0 directly with explicitly constructing the mass differences between the lattice and the physical points. In summary, we have 272 [258(experimental) + 14(lattice finite-volume multihadron) + 4(lattice finite-volume single baryon)] data points and construct a correlated χ^2_{dof}, as described in Sec. V B.

In the fits, we use Nelder-Mead minimization and check for absolute convergence by performing the fits using different initial conditions. We are fitting models (M1, etc.) with increasing computational complexity using regularization S1, S2, and S3, including lattice and/or experimental data. In the end, the best fits are selected using each regularization S1, S2, and S3 using all of the available data. The pole positions are computed for each fit individually and can be found in the Appendix.

The same model parameters are constrained through the lattice and experimental data, although in the former case via the complex partial-wave amplitude f_{0+} and in the latter case via the real $|f_{0+}|^2$. Regularization S1 provides maximal freedom, enabling a completely independent set of subtraction constants at the physical and lattice points. However, in the case of the lattice data the projection to the isospin zero channel eliminates the dependence through subtraction constants, $a_{\pi\Lambda}, a_{\eta\Sigma}$. In addition, during our numerical investigation we found out that the fit to the lattice data is insensitive to $a_{K\Xi}$.

To check the robustness of our fits, we select M3S1PL (F_{17}) and test its behavior under different random initial conditions. In this case, the minimization is performed in a 16-dimensional parameter space, and we examine whether and how the global minimum is consistently reached. The results are shown in Fig. 8. In the left panel, we show the convergence of χ^2_{dof} as a function of the iteration number. In all cases, χ^2_{dof} converges to the same minimum value, indicating consistent fit quality across different initializations. In the middle panel, we present the convergence of the parameter b_0, which shows only a small spread in its final values. The right panel displays the convergence of the subtraction constants $a_{\eta\Sigma}$ at the physical point, where two

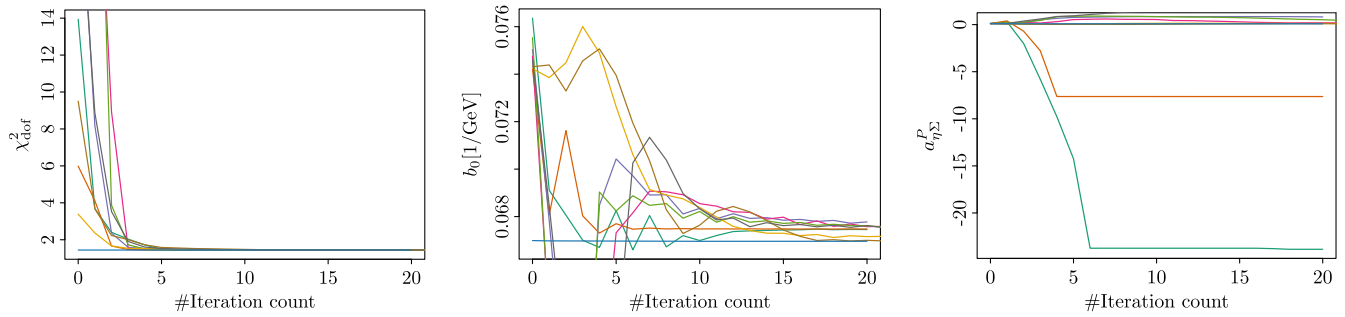

FIG. 8. Convergence check of Fit 17 (M3S1PL) using nine different sets of initial parameters. Left: evolution of $\chi^2_{\rm dof}$ as a function of iteration number. Middle: convergence behavior of the parameter b_0. Right: convergence behavior of the subtraction constant $a_{\eta\Sigma}$ at the physical point.

outlier trajectories are observed. We note that the spread of the values for $a_{\eta\Sigma}$ is the largest among all fitting parameters. However, as seen in the left panel from the $\chi^2_{\rm dof}$ values, the data are described well by all of the solutions, including the outlier ones. For the final fit selection, we choose the one where all subtraction constants are smaller than 0.05 in absolute value, guided by naturalness arguments, although all solutions lead approximately to the same two-pole structure.

In the left panel of Fig. 9 we show the fitted spectrum for all different available models and regularization schemes. We would like to point out that leading chiral order models M1 and M2 give very similar results, with the regularization S1 providing the best $\chi^2_{\rm dof}$ estimate. Note that in this

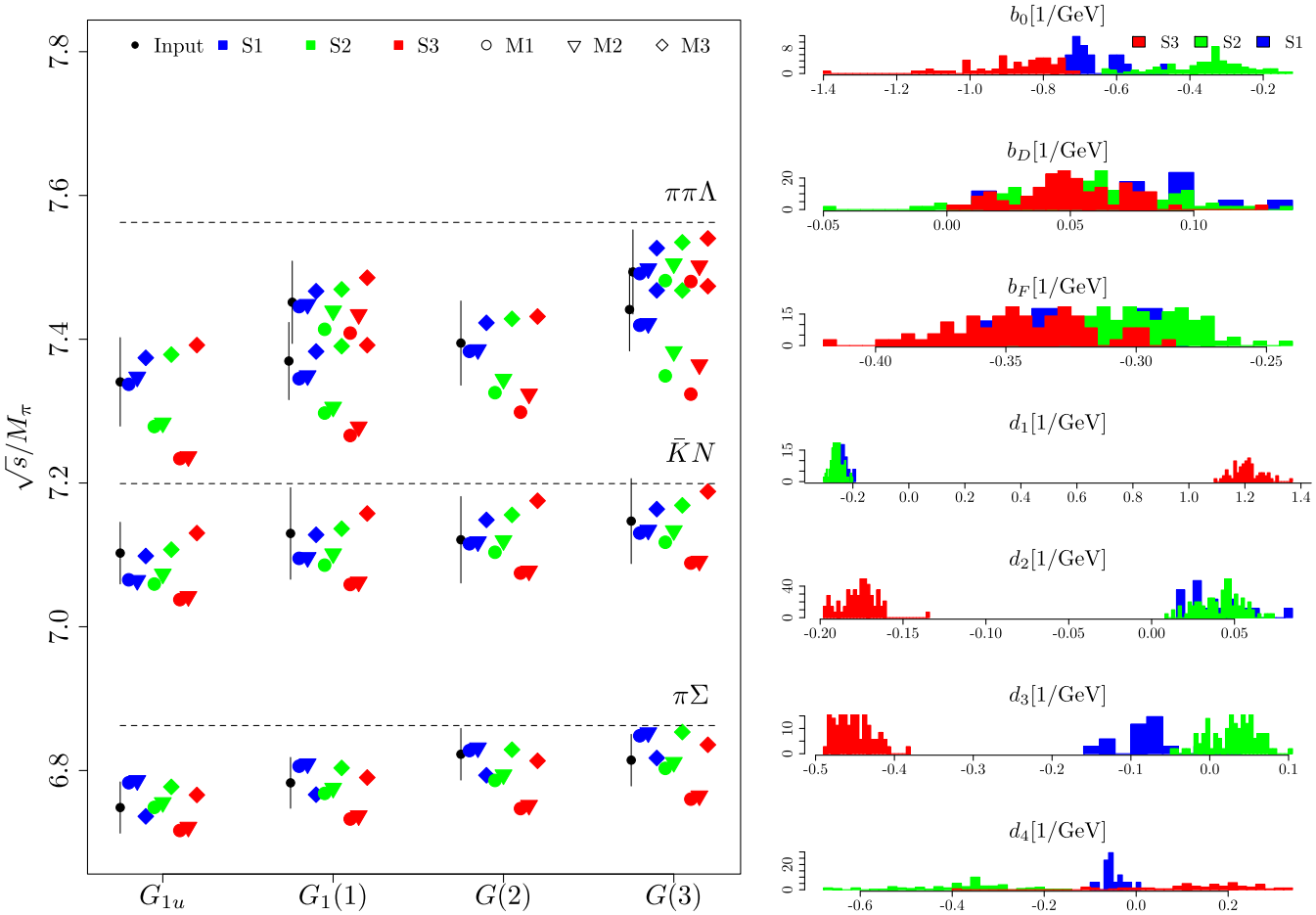

FIG. 9. Left: model (M1, M2, and M3) predictions for the lattice spectrum using different regularizations (S1, S2, and S3). Fits were done using only the lattice data. More detailed results including cross-correlations are provided for each fit in the Appendix. Individual χ^2 values can be found in Fig. 7. Right: distribution of low-energy constants for the best combined fits for three different schemes.

case, S3 has only one parameter, whereas the S2 prediction is parameter-free. In the right part of Fig. 9 we show the bootstrap samples' distribution of the LECs using the three different regularizations, fitting all the available data. Dynamical LECs (d_1, d_2, d_3) do agree in S1 and S2 schemes, but show large statistical and systematic uncertainties in d_4. Our results for the symmetry breaking parameters (b_0, b_D, b_F) are compatible with those obtained in Ref. [124] using the corresponding CLS ensembles, and also quite close to the values obtained in perturbative calculations [77].

VI. RESULTS AND DISCUSSION

After having determined the best parameters of each model with respect to the lattice and experimental input, we turn to the main goal of the paper, extracting transition amplitudes and their analytic structures. In the relevant energy region, the former are holomorphic functions, except the meson-baryon right-hand cuts taken care of through the unitarization procedure (Sec. IV B) and possible poles on the unphysical Riemann sheets associated with excited hadrons, see, e.g., [5,6,92,125].

In dealing with the 10-channel problem, there are 2^{10} Riemann sheets associated with the right-hand meson-baryon cuts. There are various ways to label those. Most frequently [11,126], one denotes a Riemann sheet (full complex energy plane) by a sequence $[\pm\ldots\pm]$ referring to $\mathrm{sgn}(\mathrm{Im}(p_{\mathrm{cm}}(s)))$ in each two-body channel. For example, any experimental or lattice input is obtained on the real energy axis of the physical sheet $[+\cdots+]$. An unphysical sheet connected to the physical one between mass-ordered threshold $n-1$ and n is denoted by $[\underset{1}{-}\ldots\underset{n}{-}+\cdots+]$. Riemann sheets with mixed order of $\pm$ are sometimes referred to as hidden sheets, as they are connected to the physical real energy axis through a sequence of other sheets, see Fig. 3 in Ref. [5].

The pole positions of the Λ(1405) and Λ(1380) have been determined directly from lattice input using generic (EFT independent) tools [20,21], and from experimental results through UCHPT. While more can be said about the latter (see Fig. 7 from Ref. [9]), we use here as a reference the Particle data Group (PDG) and BaSc values (in MeV),

	Λ(1405)	Λ(1380)
physical point	$1417.7^{+6.1}_{-7.5} - i26.1^{+6.23}_{-8.2}$	$1325^{+15}_{-15} - i90^{+12}_{-18}$
	$1429^{+8}_{-7} - i12^{+2}_{-3}$	$1330^{+4}_{-5} - i56^{+17}_{-11}$
	$1434^{+2}_{-2} - i10^{+2}_{-1}$	$1388^{+9}_{-9} - i114^{+24}_{-25}$
	$1421^{+3}_{-2} - i19^{+8}_{-5}$	$1381^{+18}_{-6} - i81^{+19}_{-8}$
lattice point	$1455^{+21}_{-21} - i12^{+6}_{-6}$	1392^{+18}_{-18}

(6.1)

All these poles are obtained on the Riemann sheet $[++----++++]$ with respect to the two-body channels $\{K^-p,\ \bar{K}^0n,\ \pi^0\Lambda,\ \pi^0\Sigma^0,\ \pi^+\Sigma^-,\ \pi^-\Sigma^+,\ \eta\Lambda,\ \eta\Sigma^0,\ K^+\Xi^-,\ K^0\Xi^0\}$, as in Eq. (2.7).

A. From the lattice to the physical point

First, let us consider the case of lattice QCD results being the only input to the UCHPT approach. Indeed, we have seen in Sec. V A that the former is indeed a nontrivial input.

The M1 models F_{19}, F_{31}, and F_{18} in Fig. 7 provide an approximate description of the lattice results, including only few free fit parameters, as described in Sec. V C. The S2 scheme provides such description quality even without any fits. Similarly, the M2 type (F_{20}, F_{32}, and F_{25}) provides similar or slightly better fits to the data with no additional parameters. This shows that the exchange diagrams (Born terms) do matter in the description of the finite-volume spectrum. Regarding the isoscalar pole structure, at the lattice point we observe (see the plots, Figs. 15–41, in Appendix A) that all models provide the Λ(1405) narrow pole and the Λ(1380) broad pole. In a few but not all cases, the latter becomes a virtual bound state, as also obtained by the BaSc (K-matrix) analysis.[3] More importantly, the S1 type of models predict a resonance Λ(1380) with non-negligible width, having better χ^2_{dof} than the other fits. Extrapolating to the physical point, while neglecting the quark mass dependence of the subtraction constants in the S1, as in Sec. V A, we observe again a clear two-pole structure with the spread of poles due to variations of the model types reflecting the spread of the reference values. Regarding the isovector states, all models except M1S1 do predict a state whose position, however, varies strongly with the model type.

Models of the M3 type (F_{01}, F_{15}, and F_{10} in Fig. 7) have larger flexibility and do indeed provide an excellent

[3]An interesting data-driven nonparametric approach based on Nevanlinna interpolation was proposed recently in Ref. [127].

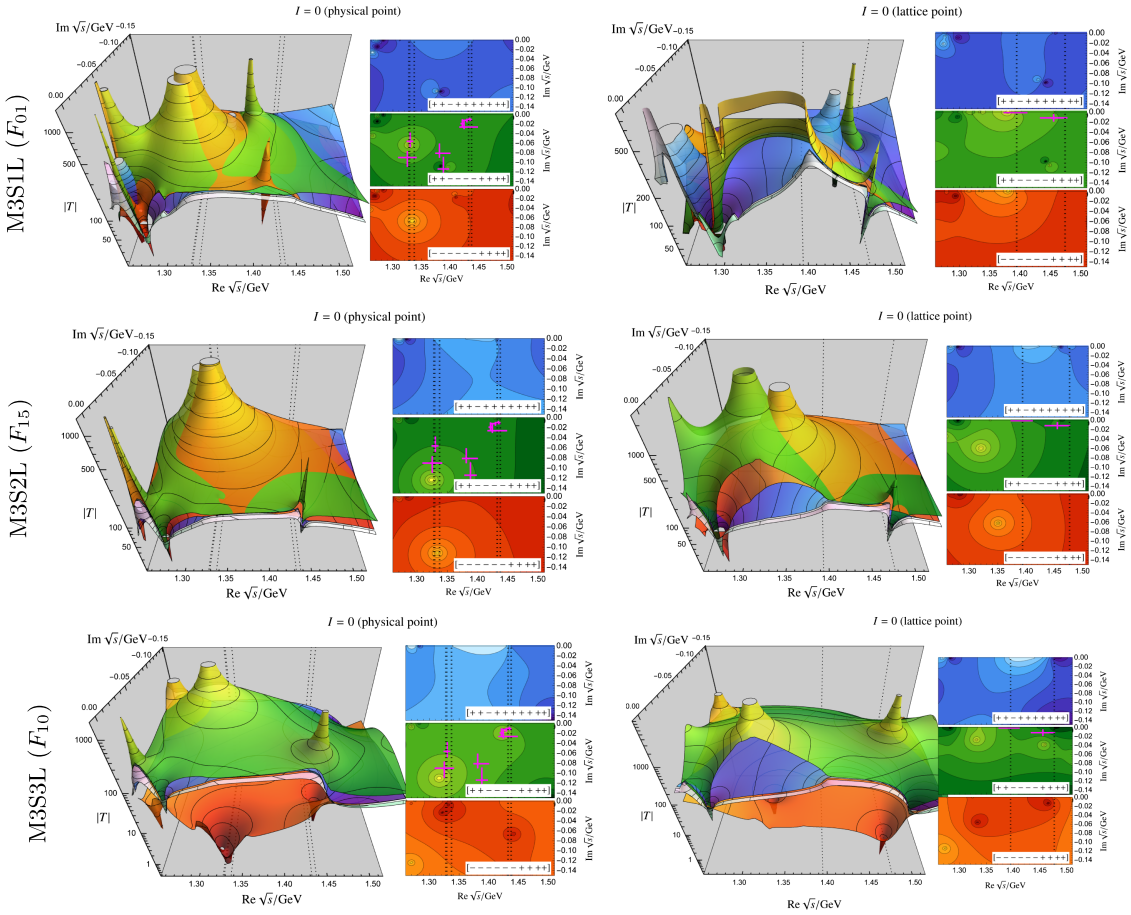

FIG. 10. Isoscalar scattering amplitude next to the physical (light pink surface for Im $\sqrt{s} > 0$ in the 3D plot) and unphysical Riemann sheets (color coded) of the solutions (M3Sx type) fitted only to the lattice QCD results. Extrapolation to the physical point is shown in the left column. More details of the fit and predictions thereof can be found in Appendix A.

description of the lattice input ($\chi^2_{\text{dof}} \approx 1$), see Fig. 7. On the most relevant sheet $[++---++++]$, we do again observe two poles both for the lattice point and after an extrapolation also at the physical point, see Fig. 10. However, all pole positions vary strongly between different models. For example, F_{01} does agree with the reference values in Eq. (6.1) on the $\Lambda(1380)$ pole position, but not on the corresponding $\Lambda(1405)$ value. Similar observations hold for the F_{10} and F_{15} fits. Interestingly, all chiral extrapolations to the physical point provide a similar prediction for the $\Lambda(1380)$, which also qualitatively agrees with the reference values in Eq. (6.1). The position of the $\Lambda(1405)$ pole is on the other side, not well predicted at the physical point.

We conclude that a combination of currently available lattice QCD finite-volume spectra combined with the modern UCHPT approaches does indeed provide proof for the existence of two states, $\Lambda(1405)$ and $\Lambda(1380)$. However, it also seems that the pole positions are not yet fixed when taking into account systematic uncertainties of the UCHPT approaches. Information criteria from Sec. V B seem to prefer the S2 and S3 types of fits due to the strong weight on the number of parameters.

B. From the physical to the lattice point

Obviously, it is also possible to inverse the procedure of the last section, using only experimental data as input then predicting the pertinent lattice point results. One motivation behind this is to test the predictive power of the UCHPT approaches outside of the fitted quark mass domain.

The M1 and M2 types of models do not allow an adequate description of the experimental data, as shown in Fig. 7. A look at the separated contributions to the χ^2 value with respect to different observable types reveals that this is mostly due to the threshold values including the so-important SIDDHARTA results [62] and very recent AMADEUS data [52,68]. The corresponding extracted isoscalar and isovector pole positions can be found in Appendix B (see Figs. 42–66). Clearly, since the models are at odds with the data, the results scatter erratically and should not be overinterpreted.

The most flexible model type M3 (F_{30}, F_{13}, and F_{11}) provides a reasonable description of all experimental data ($\chi^2_{\text{dof}} \approx 1.5$), as shown in Fig. 7. Again, S2 and S3 are favored due to the *AIC* and *BIC*. At the physical point, we observe again the two-pole structure of the isoscalar states

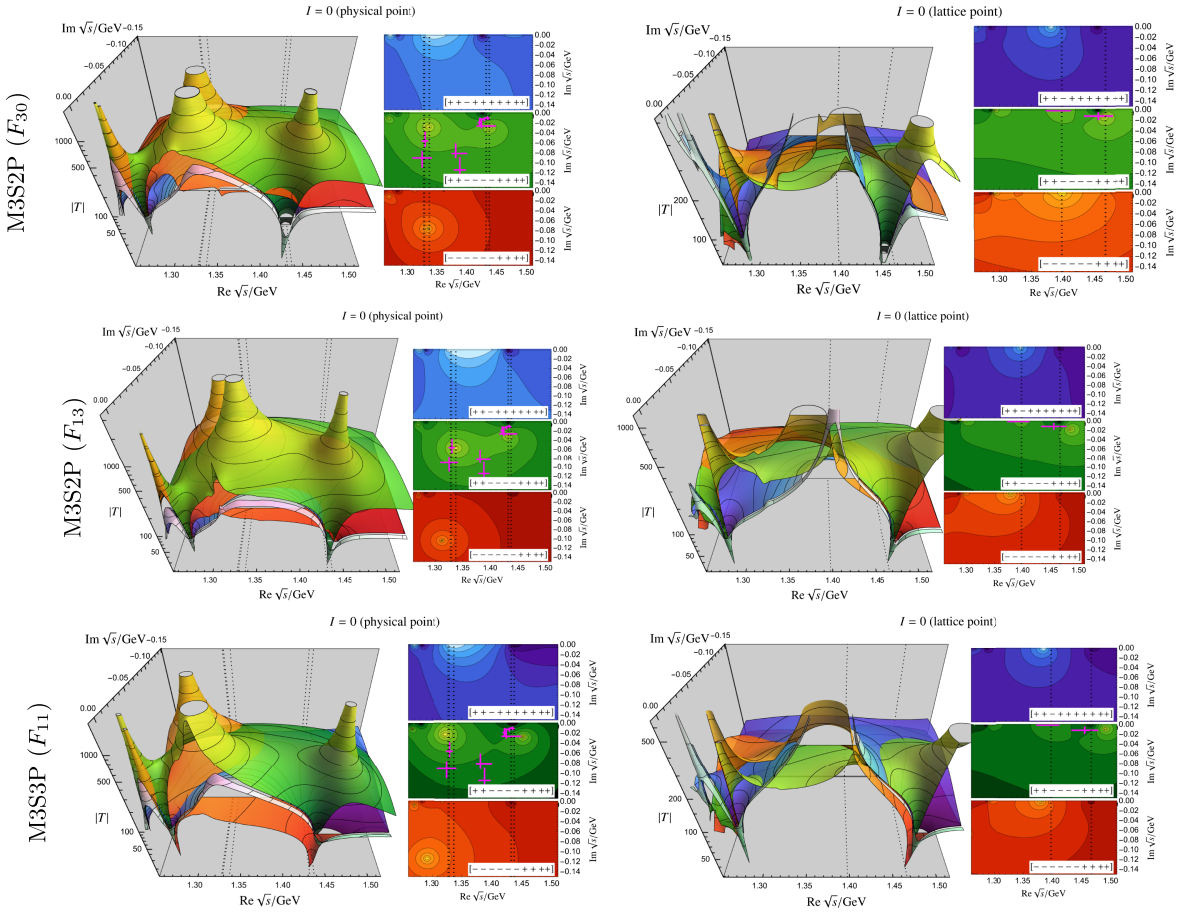

FIG. 11. Isoscalar scattering amplitude next to the physical (light pink surface for Im $\sqrt{s} > 0$ in the 3D plot) and unphysical Riemann sheets (color coded) of the solutions (M3Sx type) fitted only to the experimental input. Extrapolation to the lattice point is shown in the right column. More details of the fit and predictions thereof can be found in Appendix B.

with well-fixed Λ(1405) and less determined Λ(1380) poles, see Fig. 11. At the lattice point, all three solutions (F_{30}, F_{13}, and F_{11}) provide a prediction of the pole structure, which indeed overlaps with the BaSc determination [20] within $\approx 2\sigma$. Comparing this to the pertinent observation of the previous Sec. VI A, it is reasonable to conclude that experimental data provide more strict constraints on the UCHPT approaches than the recent lattice QCD results. In the isovector case, poles are predicted in each model type for the lattice point. Their positions vary strongly with the chosen model type. At the physical point, even less can be concluded with certainty. Indeed, this confirms the results of the previous metastudy [11] of various unitary models, leading to vastly different predictions in the isovector case. Whether this can be mitigated through combined use of the lattice and experimental input is discussed in the next section.

C. Combined analysis at the lattice and physical point

We have previously seen (Secs. VI A and VI B) that both lattice and experimental input can be successfully fit through the UCHPT model, providing in some cases also sensible predictions outside of the fitted range. Still, a more detailed examination also shows that uncertainties are sizable. Thus, a combined fit to lattice and experimental input is performed in this work for the first time.

First, as shown in Sec. VI C, Weinberg-Tomozawa and leading chiral order UCHPT model (M1 and M2) types are effectively ruled out by not being able to describe the (near)-threshold SIDDHARTA and AMADEUS data. For completeness the results of the combined fit can be found in Fig. 7. Note that only the S3 type needs to be refit to the combined input, while S1 and S2 types decouple χ^2 contributions from lattice and experiment data when no NLO parameters (b's) are used.

The results of the M3 type models for all three regularization schemes, S1, S2, and S3, are provided in the last three rows (see F_{17}, F_{16}, and F_{12}) of Fig. 7. Overall, a good χ^2_{dof} is obtained with a relatively flat distribution of the individual contributions from different observables, see the right panel of Fig. 7. The biggest contributions come from cross section data, which again points to the systematic uncertainties within experimental data discussed

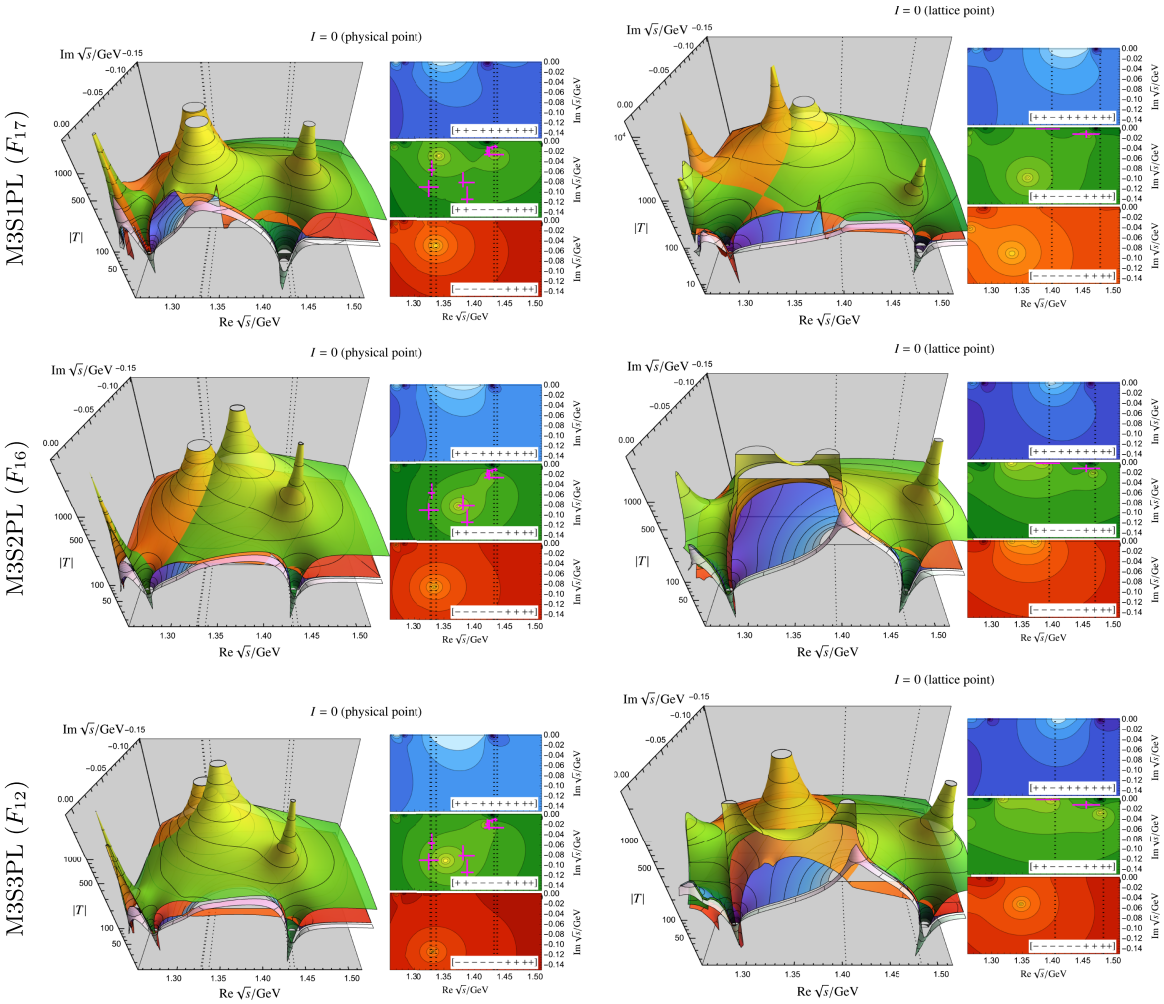

FIG. 12. Isoscalar scattering amplitude next to the physical (light pink surface for Im $\sqrt{s} > 0$ in the 3D plot) and unphysical Riemann sheets (color coded) of the M3Sx type approaches fitted to the lattice and experimental input. More details of the fit and predictions thereof can be found in Appendix C.

in Sec. III. Further details of the fit are provided in Appendix C (see Figs. 67–81).

Figure 12 shows the isoscalar pole positions on the relevant unphysical Riemann sheets for the lattice and physical points. All, except the lower pole [$\Lambda(1380)$] of the M3S1 type at the lattice point, agree with the reference values (magenta in the figure). Notable is, however, that because of the unknown quark mass dependence, the subtraction constants a in the S1 type are fitted separately for lattice and physical points. One consequence of this is that the fit is too volatile, depending strongly on the starting values, as discussed in Sec. V C. Secondly, this fit is also disfavored in comparison to S2 and S3 by both information criteria despite smaller χ^2_{dof}.

To further examine the uncertainty associated with the pole positions, we resample the obtained fits by varying the input according to the provided (statistical) uncertainties. In the lattice QCD case, this is directly accomplished using provided bootstrap samples, whereas in the experimental case parametric bootstrap samples are generated by drawing synthetic datasets from uncorrelated, Gaussian-distributed data points, using the reported central values as the means and the quoted uncertainties as the standard deviations. The final result is provided in the summary plot in Fig. 13, where systematic (model types) and statistical errors (resampling) are included and compared to the reference values from the literature. Note that the latter were obtained through fits to either experimental or lattice input. The physical point result agrees nicely with the previous phenomenological fits also reflecting the large uncertainty of the $\Lambda(1380)$ pole positions. The $\Lambda(1405)$ is narrowed down to a very small region. At the lattice point, the position of the latter state supports the CHPT-independent determination of the lattice collaboration (BaSc [20,21]) but tends to be slightly larger in real and imaginary parts. In fits S2 (F_{16}) and S3 (F_{12}), the $\Lambda(1380)$ is found for all bootstrap samples on the real axis just below the $\pi\Sigma$ threshold. Note

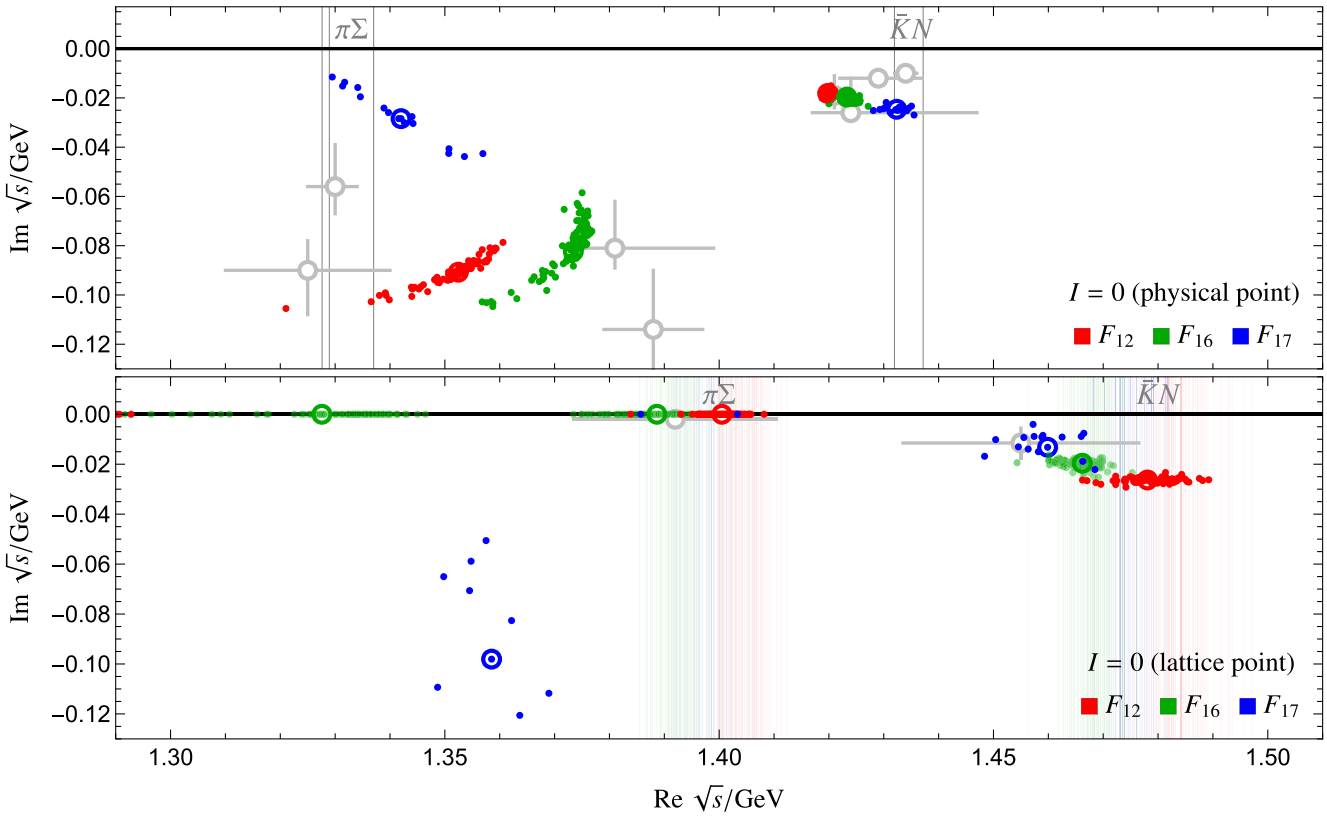

FIG. 13. Pole positions for $I = 0$ using best global fit models M3S1 (fit F_{17}), M3S2 (fit F_{16}), and M3S3 (fit F_{12}). Pole positions are obtained on the $[++----++++]$ Riemann sheet for physical and unphysical (cf. $M_\pi \approx 200$ MeV, etc.) quark masses. Circled pole positions are central fits compared to resampled fits, as described in the main text. Vertical lines show positions of the two-body thresholds (resampled for the lattice point). Gray dots show the reference values from fits to either lattice or experimental input [12,13,20,50].

that thresholds at the lattice point are also subject to resampling, which is very important to keep track of. Individual thresholds are represented by the color-coded vertical lines. We also observe a second virtual bound-state pole (cf. $\sqrt{s} \approx 1.33$ for F_{16}), which is required due to analyticity. For a related discussion in the context of this and other excited hadrons, see, e.g., Refs. [95,128–133]. Numerical values are provided in Table I. A critical observation is, however, that there is a non-negligible set of solutions (S1 type, F_{17}) predicting a $\Lambda(1380)$ resonance pole away from the real axis. We have checked explicitly that the poles are smoothly varying when moving along a linearized trajectory between the lattice and physical points. While disfavored by the *AIC* or *BIC*, the existence of such solutions draws at least a shadow of a doubt that the pole positions of the $\Lambda(1380)$ state are resolved through the currently available (lattice and experimental) input. Of course the existence of both poles is undisputed by this and seems to be now solidified by the combination of UCHPT, lattice, and experimental inputs.

As a final observation we also provide predictions of the pole positions for the isovector case, including systematic and statistical uncertainties. The result is depicted in Fig. 14, referring again to the Riemann sheet $[++----++++]$ connected to the physical real axis between $\pi\Sigma$ and $\bar{K}N$ thresholds. At the physical point, we observe for all fit types a broad state with a width of around $\Gamma \approx 200$–400 MeV and mass above 1300 MeV. Solution F_{17} provides a second state with a lower width, which is possibly a sign of an overfit. Other states far above the $\bar{K}N$ threshold also exist but their influence on the observables at real energies is expected to be negligible. At the lattice point the poles mostly do not move much, except for the narrow F_{17} pole. Presumably, this is simply due to the large widths of the found states, which, therefore, have little effect on the real energy axis, where the input either from the experiment or lattice is provided. Numerical values are provided in Table I. We conclude that the existence of the isovector, negative-strangeness excited baryon state is very likely, but because of its large width its position is currently very hard to resolve. Turning this argument around, this means that lattice results in this sector are highly desired.

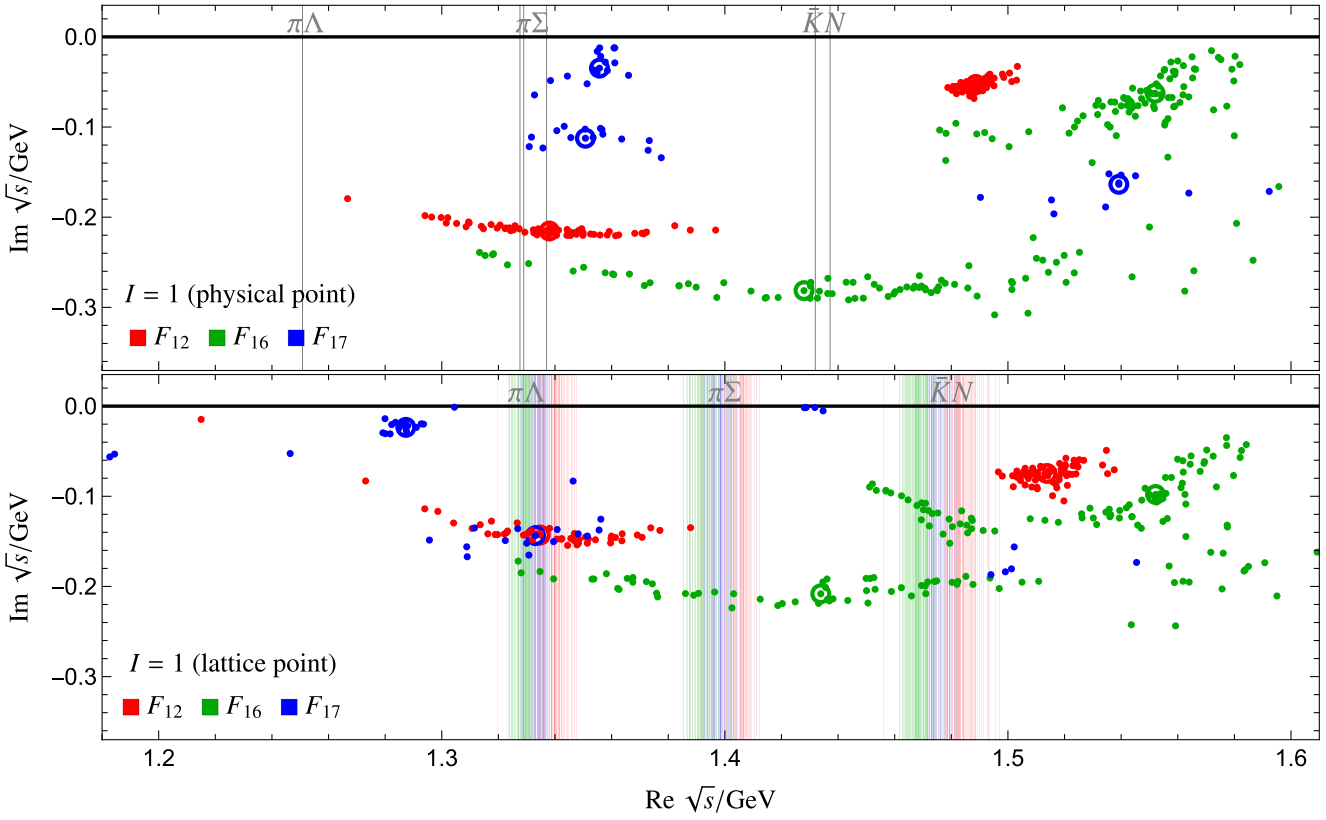

FIG. 14. Pole positions for $I = 1$ using best global fit models M3S1 (fit F_{17}), M3S2 (fit F_{16}), and M3S3 (fit F_{12}). Pole positions are obtained on the $[++---++++]$ Riemann sheet for physical and unphysical (cf. $M_\pi \approx 200$ MeV, etc.) quark masses. Circled pole positions are central fits compared to resampled fits, as described in the main text. Vertical lines show the positions of the two-body thresholds (resampled for the lattice point).

ACKNOWLEDGMENTS

We thank BaSc collaboration for providing details of the lattice calculation, and Peter Bruns, Fernando Romero-López, Miguel Salg, Juan Fernandez de la Garza, Feng-Kun Guo, and Christoph Hanhart for entertaining and useful discussions. The work of M. M. was funded through the Heisenberg Programme by the Deutsche Forschungsgemeinschaft (DFG, German Research Foundation)—532635001. The work of U. G. M. was supported in part by the CAS President's International Fellowship Initiative (PIFI) (Grant No. 2025PD0022) by the MKW NRW under the funding code NW21-024-A, and by the Deutsche Forschungsgemeinschaft (DFG, German Research Foundation) as part of the CRC 1639 NuMeriQS, Project No. 511713970. The work of F. P. was supported by the projects PulseQCD, DeNuTra, and MuonHVP (EXCELLENCE/0524/0269, EXCELLENCE/524/0455, and EXCELLENCE/524/0017), cofinanced by the European Regional Development Fund and the Republic of Cyprus through the Research and Innovation Foundation. R. F. F., P. H., D. G. I., and B. M. were supported by the United Kingdom's Science and Technology Facilities Council (STFC), Grant No. ST/Y000315/1.

DATA AVAILABILITY

The data that support the findings of this article are openly available [134], embargo periods may apply.

APPENDIX A: DETAILED FIT RESULTS: FITS TO THE LATTICE INPUT

1. M1S1L (F_{19})

χ^2_{dof}	1.36
$a_{\bar{K}N}$	2.108217e-03
$a_{\pi\Lambda}$	-1.079700e-01
$a_{\pi\Sigma}$	2.108217e-03
$a_{\eta\Lambda}$	2.939451e-04
$a_{\eta\Sigma}$	2.163700e-01
$a_{K\Xi}$	3.948000e-02

FIG. 15. Subtraction constants at the lattice point for M1S1L (F_{19}).

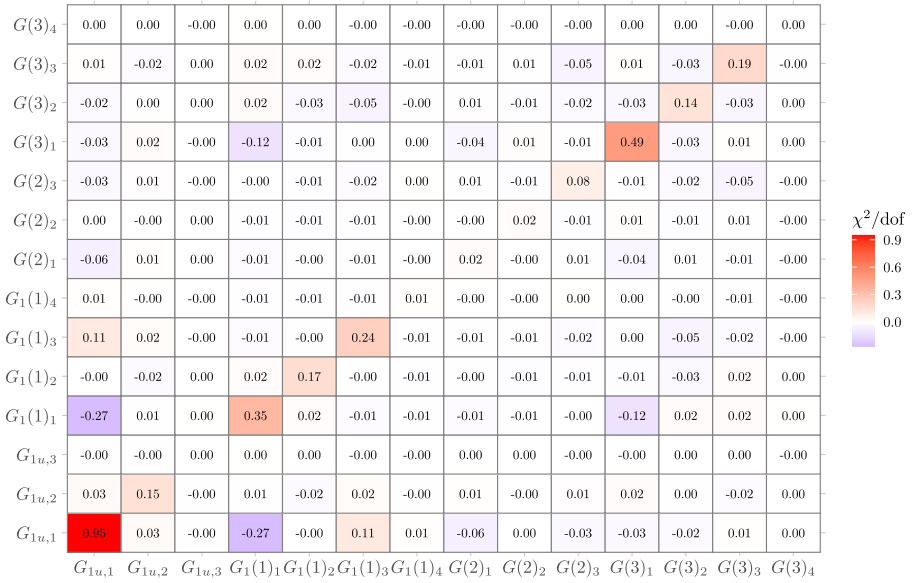

FIG. 16. Heat map of correlated $\chi^2_{\mathrm{dof},ij}$, highlighting the relative impact of each energy level on the total fit quality.

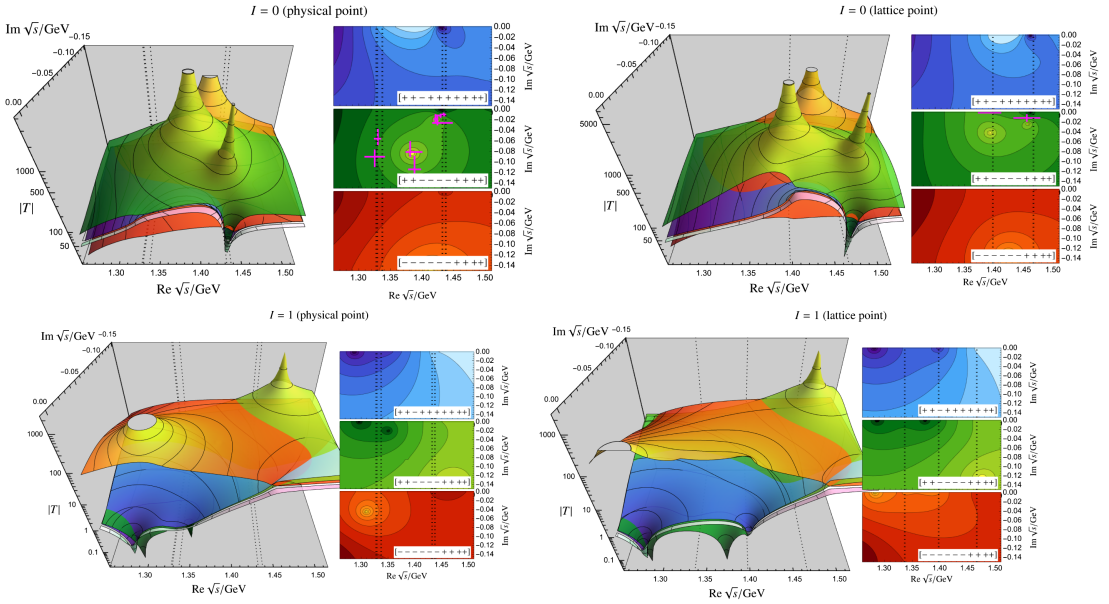

FIG. 17. Isoscalar and isovector projected absolute value of the $\pi\Sigma \to \pi\Sigma$ scattering amplitude on the unphysical second Riemann sheets. Nomenclature as in the main text. Magenta crosses represent literature values from Refs. [20,21] for the lattice point and Refs. [12,13,50].

2. M1S2L (F_{31})

χ^2_{dof}	2.89

FIG. 18. Total χ^2_{dof} for the parameter-free M1S2L (F_{31}).

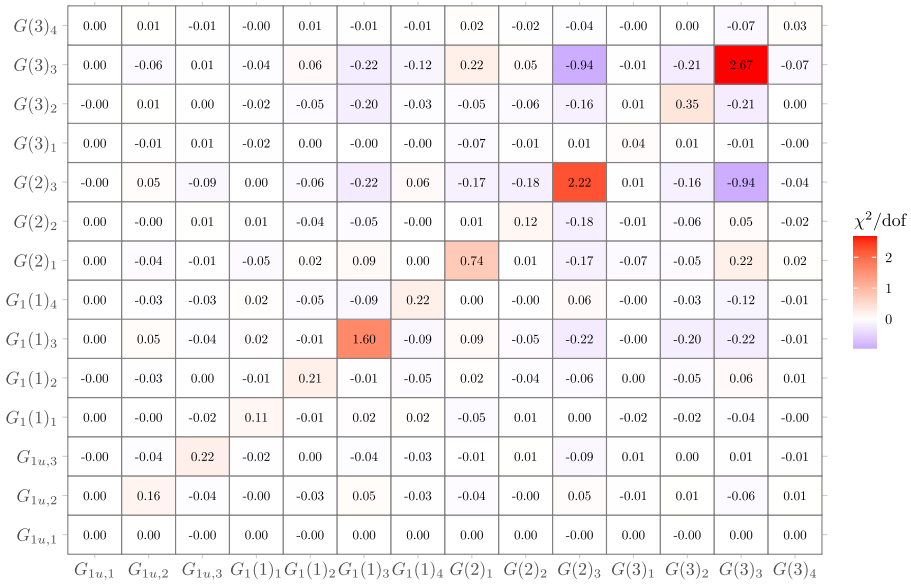

FIG. 19. Heat map of correlated $\chi^2_{\text{dof},ij}$, highlighting the relative impact of each energy level on the total fit quality.

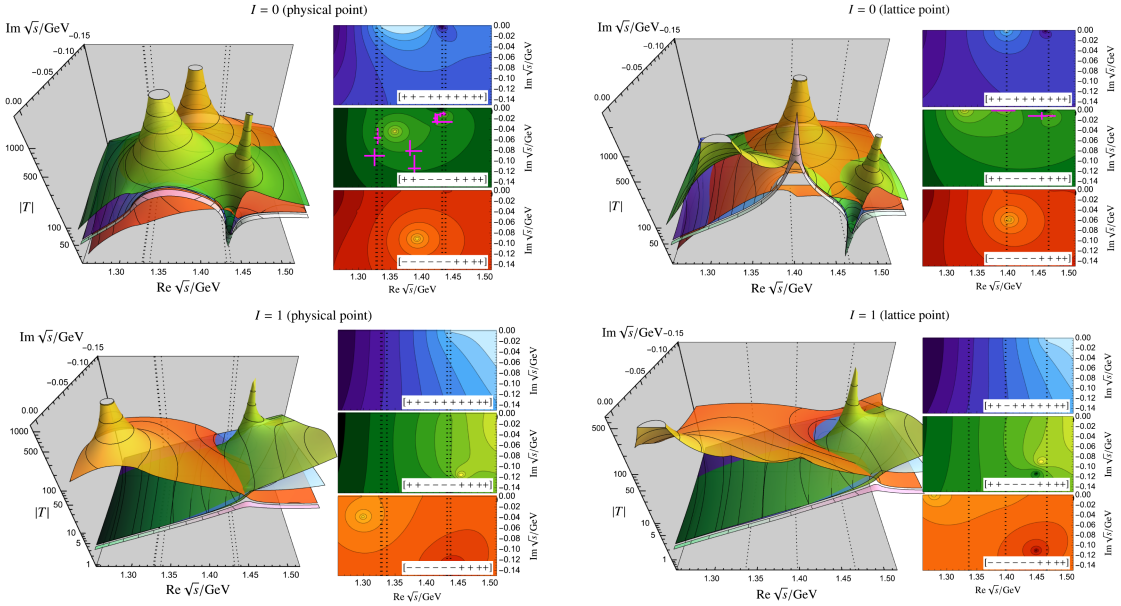

FIG. 20. Isoscalar and isovector projected absolute value of the $\pi\Sigma \to \pi\Sigma$ scattering amplitude on the unphysical second Riemann sheets. Nomenclature as in the main text. Magenta crosses represent literature values from Refs. [20,21] for the lattice point and Refs. [12,13,50] for the physical point.

3. M1S3L (F_{18})

χ^2_{dof}	4.42
Λ[GeV]	0.6892541

FIG. 21. Total χ^2_{dof} and the Λ parameter for M1S3L (F_{18}).

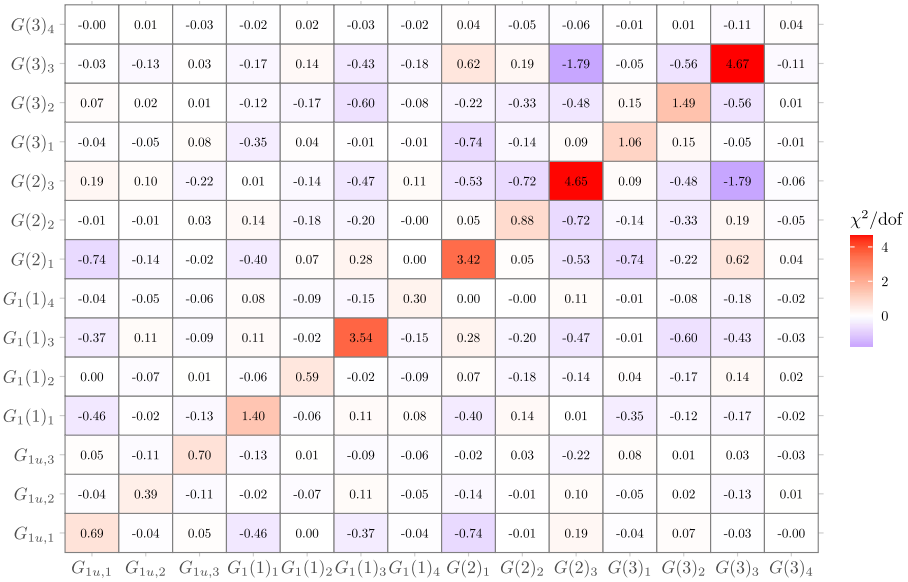

FIG. 22. Heat map of correlated $\chi^2_{\mathrm{dof},ij}$, highlighting the relative impact of each energy level on the total fit quality.

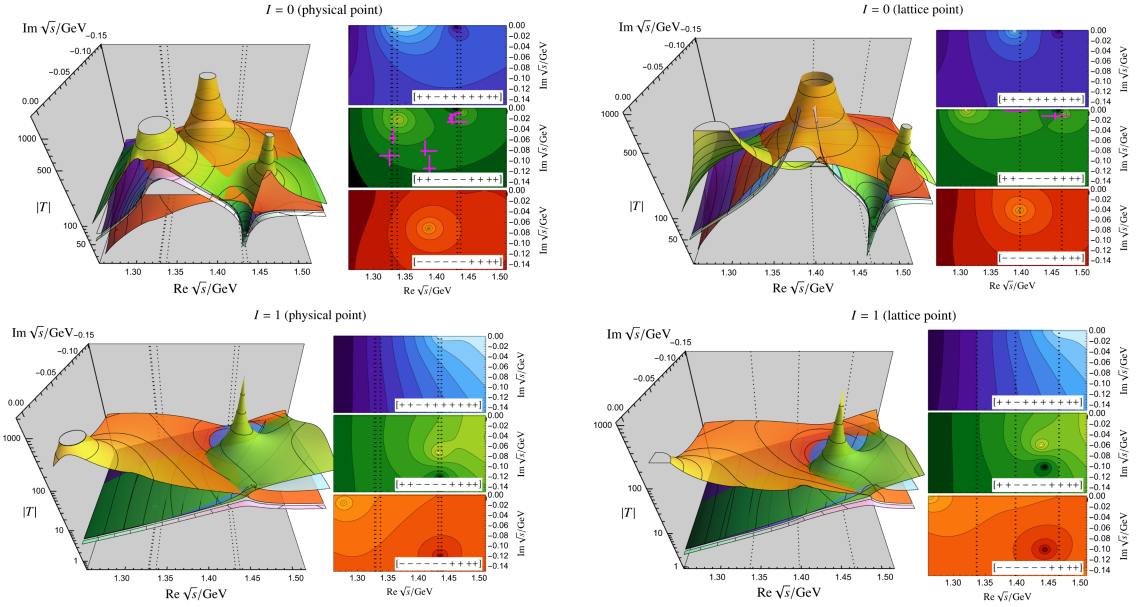

FIG. 23. Isoscalar and isovector projected absolute value of the $\pi\Sigma \to \pi\Sigma$ scattering amplitude on the unphysical second Riemann sheets. Nomenclature as in the main text. Magenta crosses represent literature values from Refs. [20,21] for the lattice point and Refs. [12,13,50] for the physical point.

4. M2S1L (F_{20})

χ^2_{dof}	1.42
$a_{\bar{K}N}$	2.249408e-03
$a_{\pi\Lambda}$	-1.079700e-01
$a_{\pi\Sigma}$	2.249408e-03
$a_{\eta\Lambda}$	-5.364455e-03
$a_{\eta\Sigma}$	2.163700e-01
$a_{K\Xi}$	3.948000e-02

FIG. 24. Subtraction constants at the lattice point for the M2S1L (F_{20}).

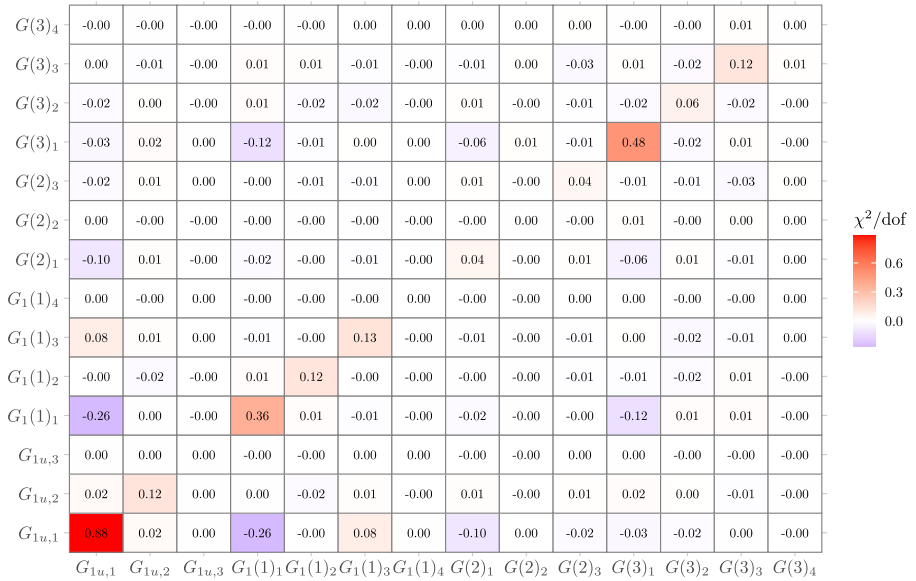

FIG. 25. Heat map of correlated $\chi^2_{\text{dof},ij}$, highlighting the relative impact of each energy level on the total fit quality.

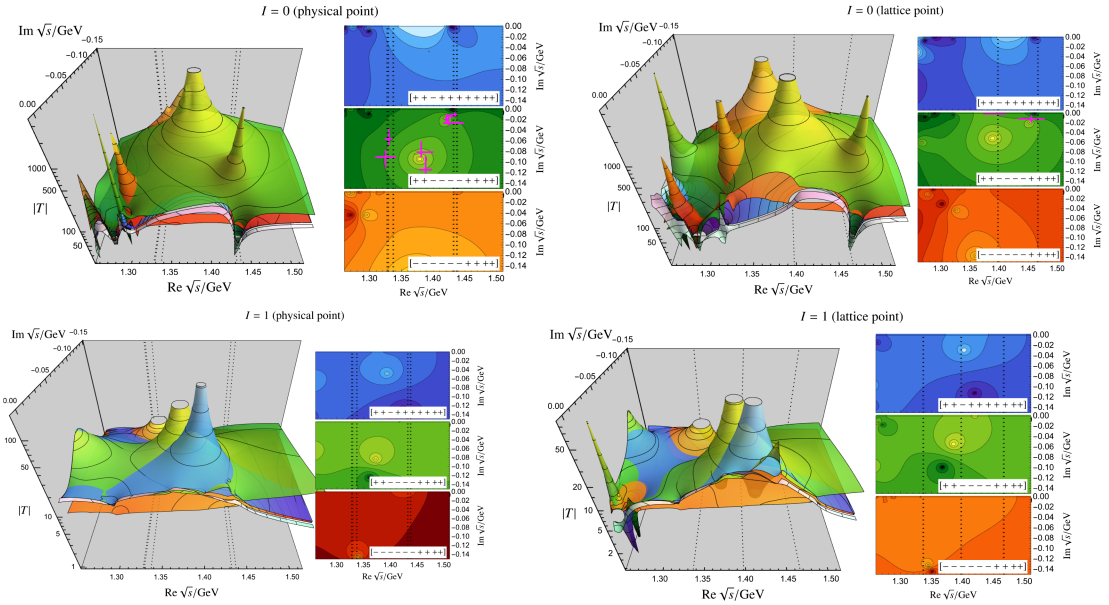

FIG. 26. Isoscalar and isovector projected absolute value of the $\pi\Sigma \to \pi\Sigma$ scattering amplitude on the unphysical second Riemann sheets. Nomenclature as in the main text. Magenta crosses represent literature values from Refs. [20,21] for the lattice point and Refs. [12,13,50] for the physical point.

5. M2S2L (F_{32})

χ^2_{dof}	2.68

FIG. 27. Total χ^2_{dof} for the parameter-free M2S2L (F_{32}).

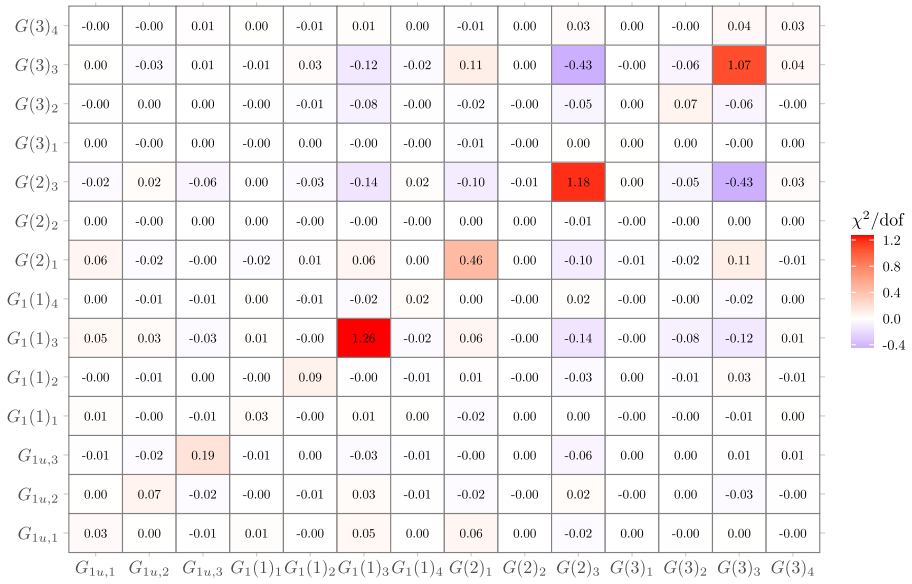

FIG. 28. Heat map of correlated $\chi^2_{\mathrm{dof},ij}$, highlighting the relative impact of each energy level on the total fit quality.

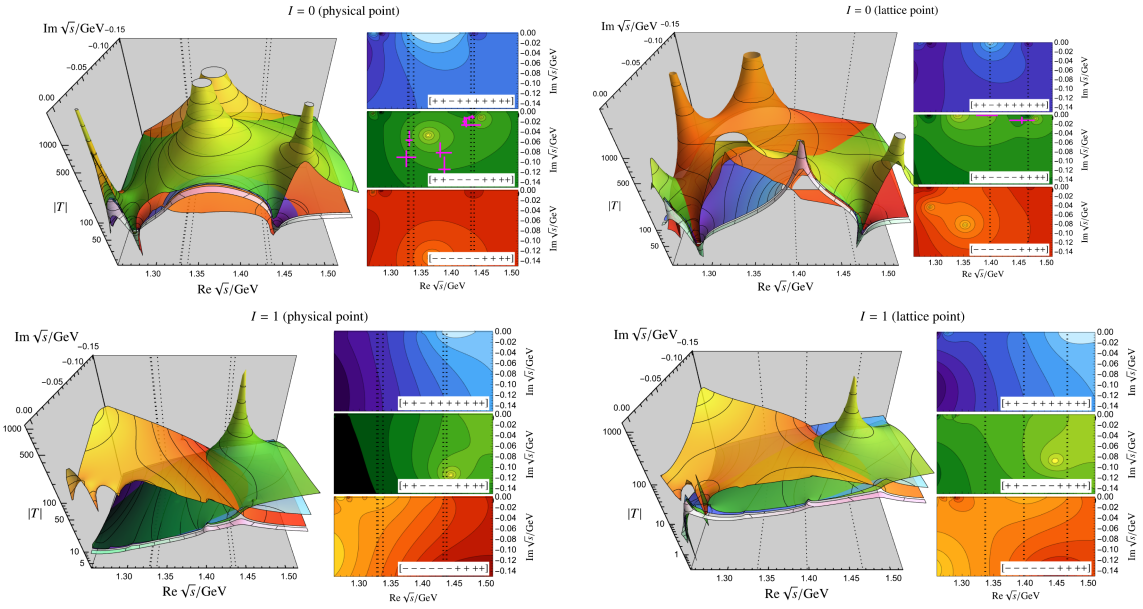

FIG. 29. Isoscalar and isovector projected absolute value of the $\pi\Sigma \to \pi\Sigma$ scattering amplitude on the unphysical second Riemann sheets. Nomenclature as in the main text. Magenta crosses represent literature values from Refs. [20,21] for the lattice point and Refs. [12,13,50] for the physical point.

6. M2S3L (F_{25})

χ^2_{dof}	3.54
Λ[GeV]	0.7054119

FIG. 30. Total χ^2_{dof} and the Λ parameter for M2S3L (F_{18}).

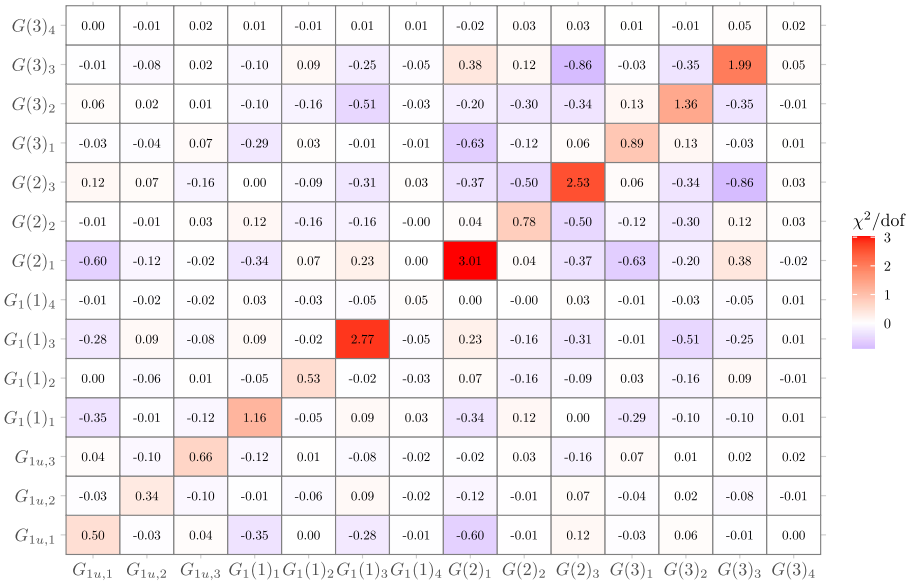

FIG. 31. Heat map of correlated $\chi^2_{\mathrm{dof},ij}$, highlighting the relative impact of each energy level on the total fit quality.

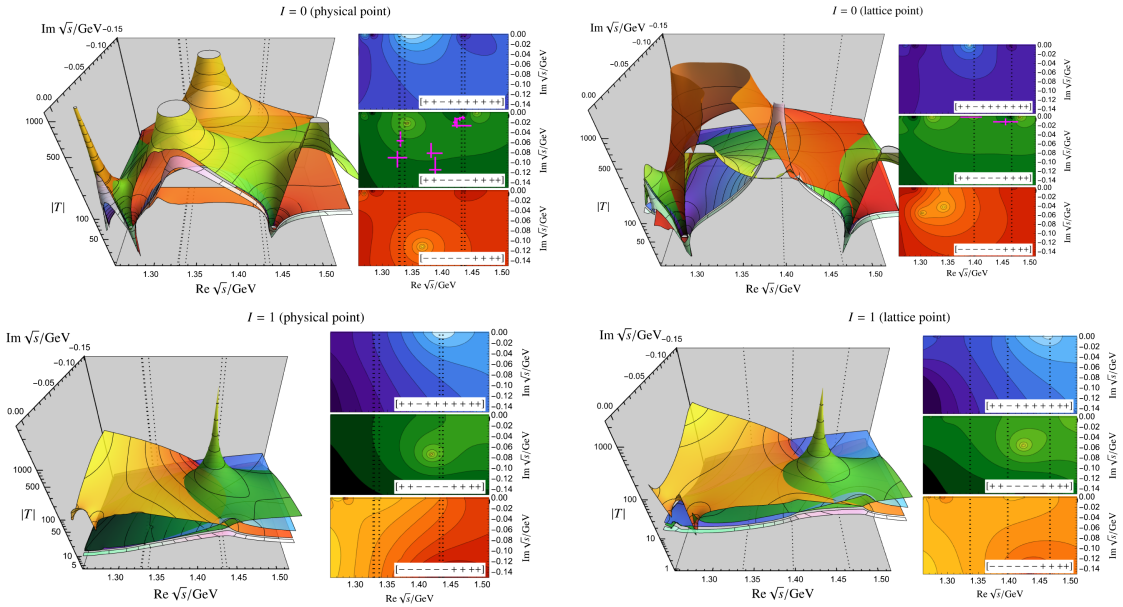

FIG. 32. Isoscalar and isovector projected absolute value of the $\pi\Sigma \to \pi\Sigma$ scattering amplitude on the unphysical second Riemann sheets. Nomenclature as in the main text. Magenta crosses represent literature values from Refs. [20,21] for the lattice point and Refs. [12,13,50] for the physical point.

7. M3S1L (F_{01})

χ^2_{dof}	0.96
$a_{\bar{K}N}$	-4.088304e-03
$a_{\pi\Lambda}$	-1.079700e-01
$a_{\pi\Sigma}$	-4.088304e-03
$a_{\eta\Lambda}$	3.560274e-03
$a_{\eta\Sigma}$	2.163700e-01
$a_{K\Xi}$	3.948000e-02
$b_0[1/\text{GeV}]$	-4.730918e-01
$b_D[1/\text{GeV}]$	8.116358e-02
$b_F[1/\text{GeV}]$	-3.145407e-01
$d_1[1/\text{GeV}]$	3.526983e-01
$d_2[1/\text{GeV}]$	-7.041922e-02
$d_3[1/\text{GeV}]$	-2.002697e-01
$d_4[1/\text{GeV}]$	-5.572205e-01

FIG. 33. The total χ^2_{dof}, subtraction constants at the lattice point, and LECs for M3S1L (F_{01}).

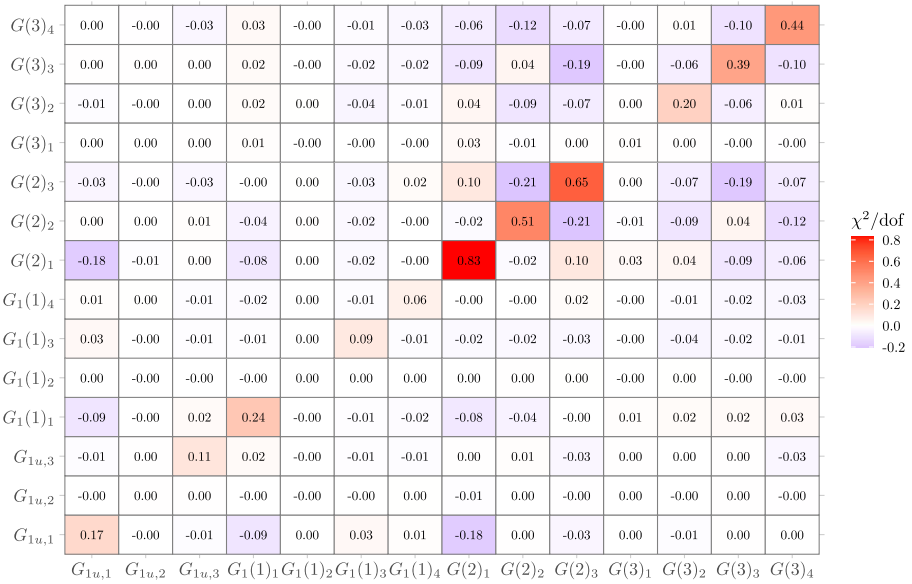

FIG. 34. Heat map of correlated $\chi^2_{\text{dof},ij}$, highlighting the relative impact of each energy level on the total fit quality.

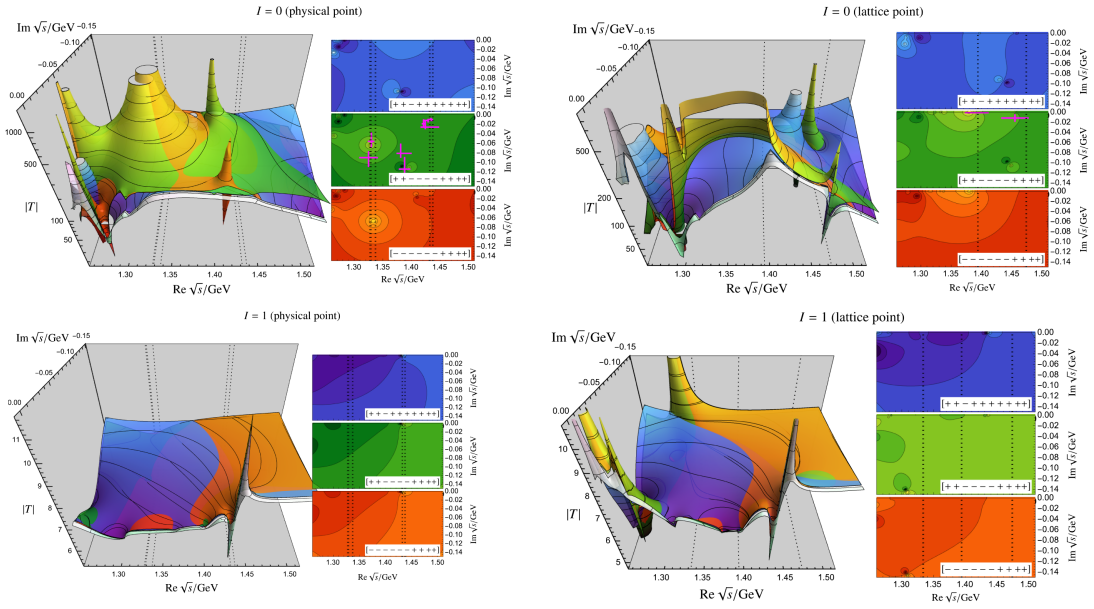

FIG. 35. Isoscalar and isovector projected absolute value of the $\pi\Sigma \to \pi\Sigma$ scattering amplitude on the unphysical second Riemann sheets. Nomenclature as in the main text. Magenta crosses represent literature values from Refs. [20,21] for the lattice point and Refs. [12,13,50] for the physical point.

8. M3S2L (F_{15})

$\chi^2_{\rm dof}$	0.90
$b_0[1/\mathrm{GeV}]$	-5.349500e-01
$b_D[1/\mathrm{GeV}]$	9.599595e-02
$b_F[1/\mathrm{GeV}]$	-3.256764e-01
$d_1[1/\mathrm{GeV}]$	-8.386487e-01
$d_2[1/\mathrm{GeV}]$	1.518967e-01
$d_3[1/\mathrm{GeV}]$	-4.546126e-01
$d_4[1/\mathrm{GeV}]$	7.207285e-03

FIG. 36. The total $\chi^2_{\rm dof}$ and LECs for M3S2L (F_{15}).

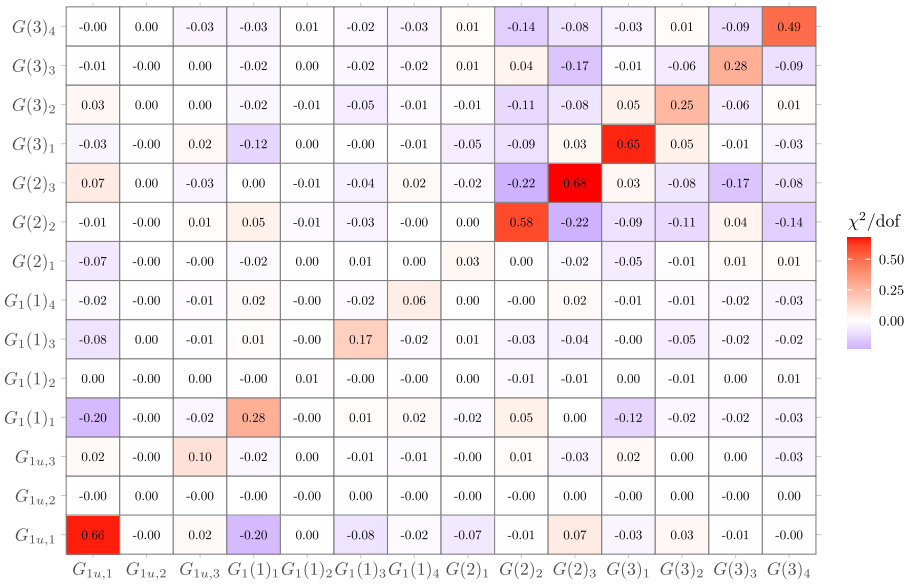

FIG. 37. Heat map of correlated $\chi^2_{{\rm dof},ij}$, highlighting the relative impact of each energy level on the total fit quality.

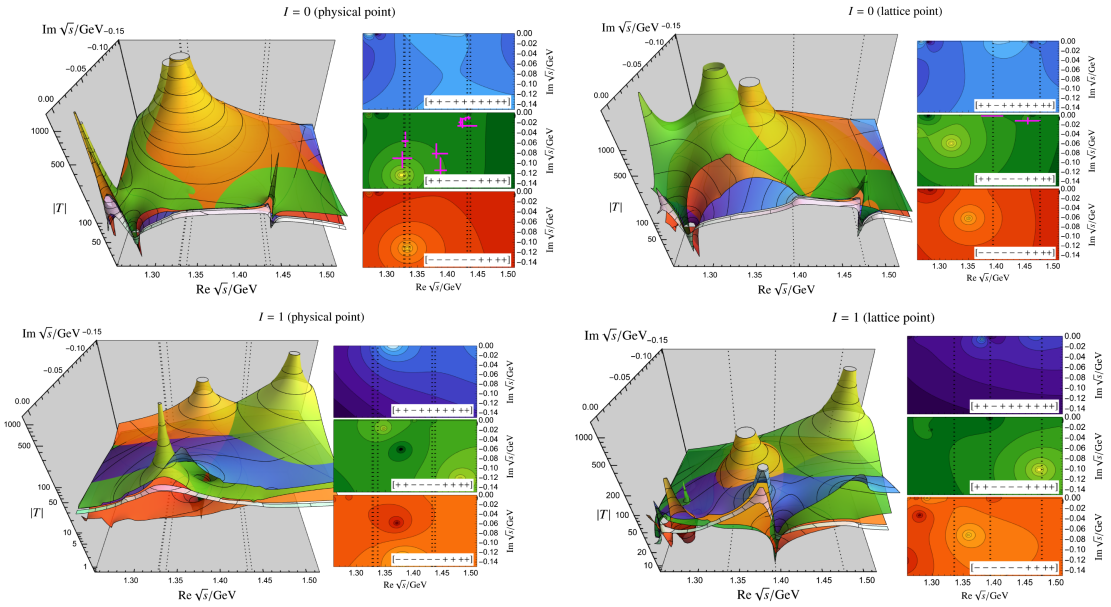

FIG. 38. Isoscalar and isovector projected absolute value of the $\pi\Sigma \to \pi\Sigma$ scattering amplitude on the unphysical second Riemann sheets. Nomenclature as in the main text. Magenta crosses represent literature values from Refs. [20,21] for the lattice point and Refs. [12,13,50] for the physical point.

9. M3S3L (F_{10})

$\chi^2_{\rm dof}$	0.92
Λ[GeV]	0.63786229
b_0[1/GeV]	-5.493596e-01
b_D[1/GeV]	8.601840e-02
b_F[1/GeV]	-3.226791e-01
d_1[1/GeV]	2.079492e+00
d_2[1/GeV]	-6.344862e-02
d_3[1/GeV]	3.538223e-01
d_4[1/GeV]	-2.262594e+00

FIG. 39. The total $\chi^2_{\rm dof}$, Λ parameter, and LECs for M3S3L (F_{10}).

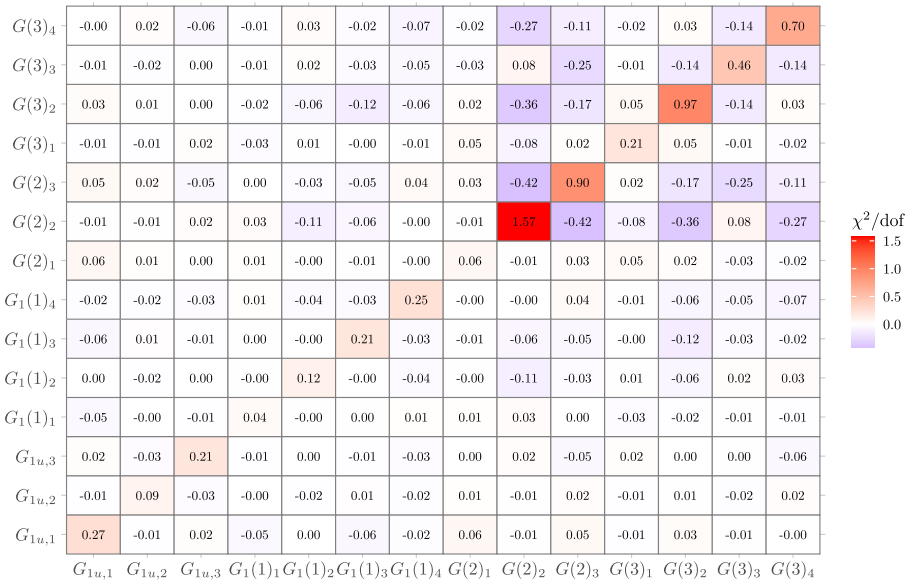

FIG. 40. Heat map of correlated $\chi^2_{{\rm dof},ij}$, highlighting the relative impact of each energy level on the total fit quality.

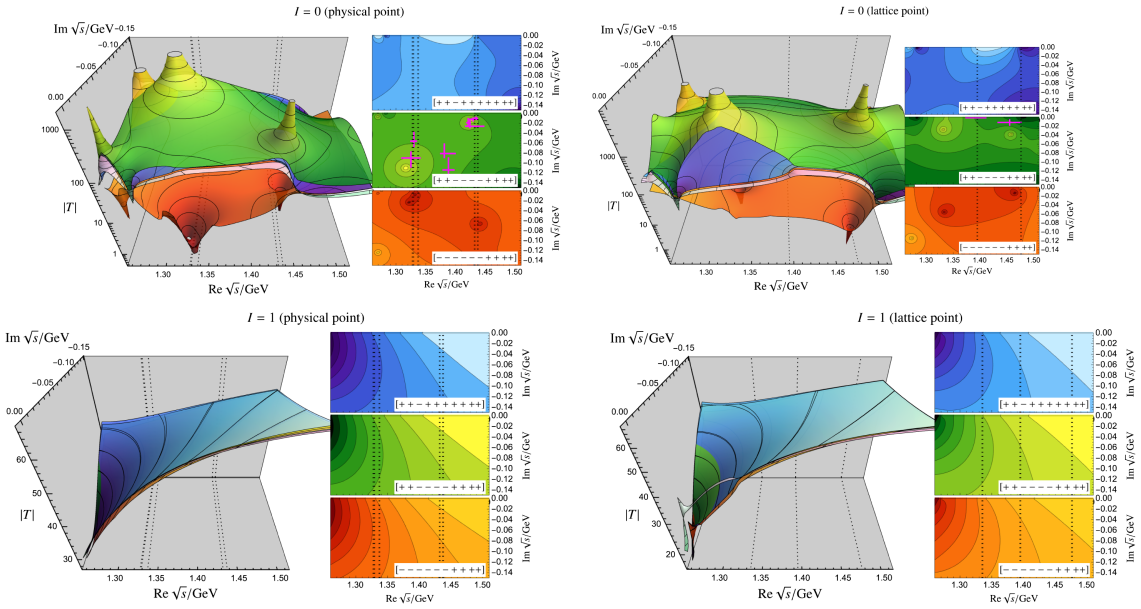

FIG. 41. Isoscalar and isovector projected absolute value of the $\pi\Sigma \to \pi\Sigma$ scattering amplitude on the unphysical second Riemann sheets. Nomenclature as in the main text. Magenta crosses represent literature values from Refs. [20,21] for the lattice point and Refs. [12,13,50] for the physical point.

APPENDIX B: DETAILED FIT RESULTS: FITS TO THE EXPERIMENTAL DATA

1. M1S1P (F_{21})

χ^2_{dof}	4.23
$a_{\bar{K}N}$	-2.348949e-03
$a_{\bar{K}N}$	-2.348949e-03
$a_{\pi\Lambda}$	3.881548e-01
$a_{\pi\Sigma}$	8.779599e-04
$a_{\pi\Sigma}$	8.779599e-04
$a_{\pi\Sigma}$	8.779599e-04
$a_{\eta\Lambda}$	1.527930e-03
$a_{\eta\Sigma}$	-7.466124e-01
$a_{K\Xi}$	-8.510607e-03
$a_{K\Xi}$	-8.510607e-03

FIG. 42. The total χ^2_{dof}, as defined in Eq. (5.1), and subtraction constants for M1S1P (F_{21}).

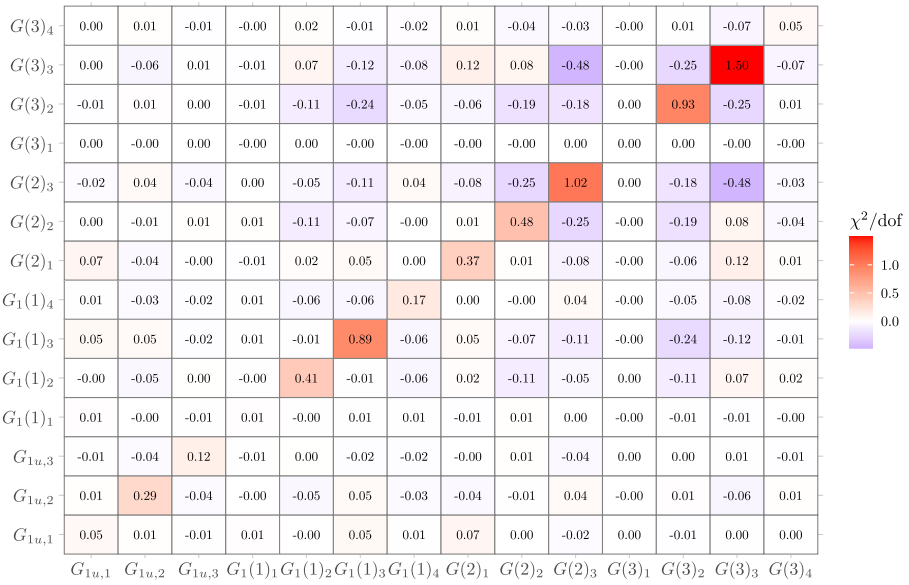

FIG. 43. Heat map of correlated $\chi^2{}_{ij}/14$, highlighting the relative impact of each energy level on the total fit quality.

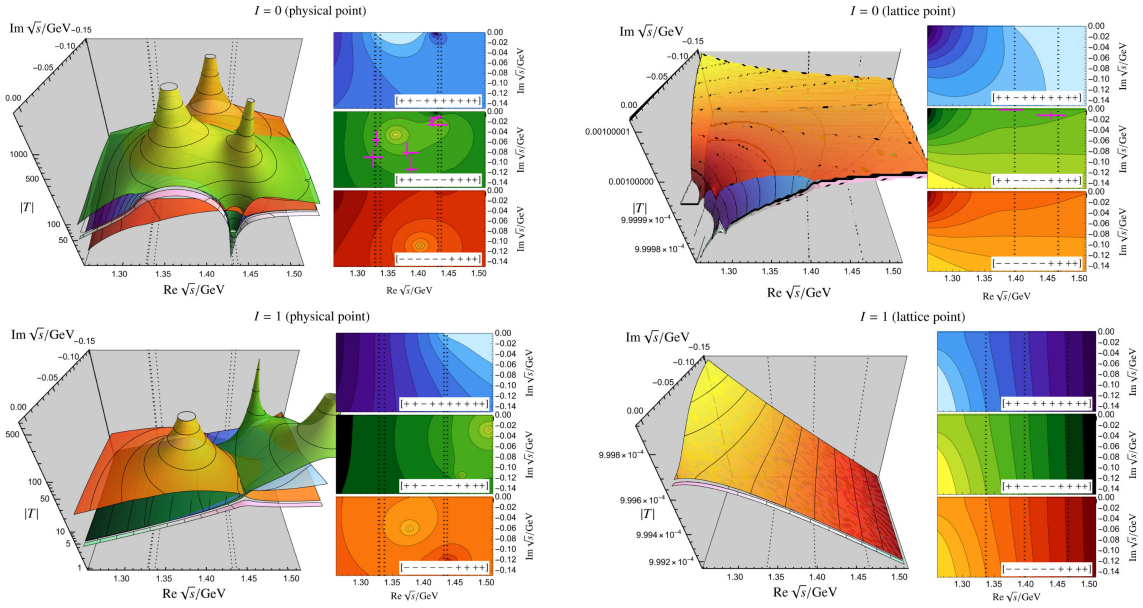

FIG. 44. Isoscalar and isovector projected absolute value of the $\pi\Sigma \to \pi\Sigma$ scattering amplitude on the unphysical second Riemann sheets. Nomenclature as in the main text. Magenta crosses represent literature values from Refs. [20,21] for the lattice point and Refs. [12,13,50] for the physical point.

2. M1S2P (F_{28})

χ^2_{dof}	25.57

FIG. 45. The total χ^2_{dof}, as defined in Eq. (5.1), for the parameter-free fit M1S2P (F_{28}).

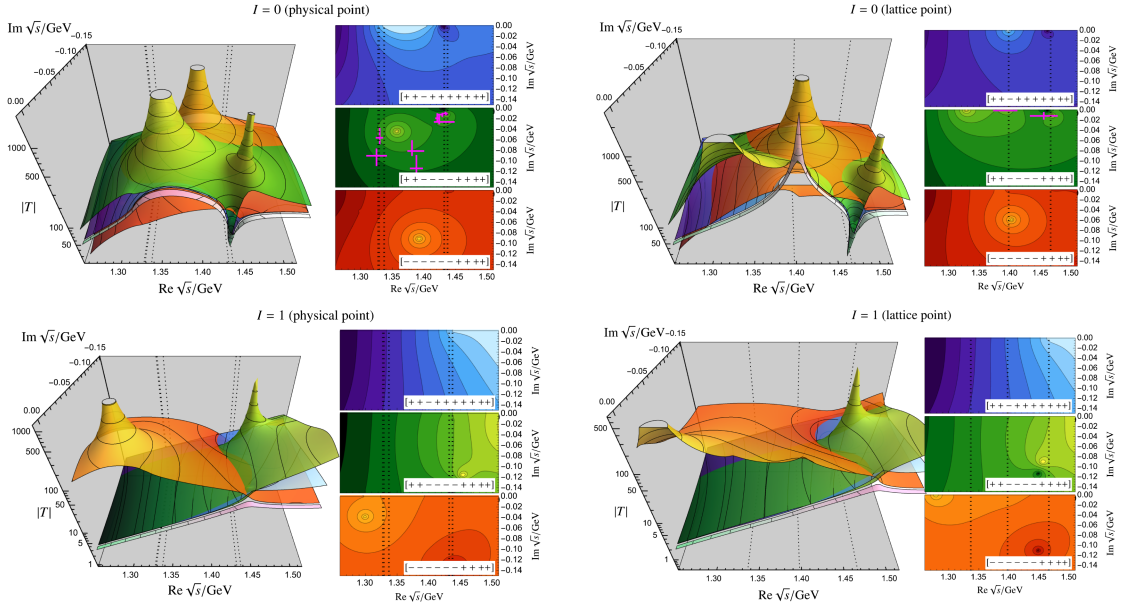

FIG. 46. Isoscalar and isovector projected absolute value of the $\pi\Sigma \to \pi\Sigma$ scattering amplitude on the unphysical second Riemann sheets. Nomenclature as in the main text. Magenta crosses represent literature values from Refs. [20,21] for the lattice point and Refs. [12,13,50] for the physical point.

3. M1S3P (F_{27})

χ^2_{dof}	30.28266
Λ[GeV]	0.8111258

FIG. 47. The total χ^2_{dof}, as defined in Eq. (5.1), and Λ parameter for M1S3P (F_{27}).

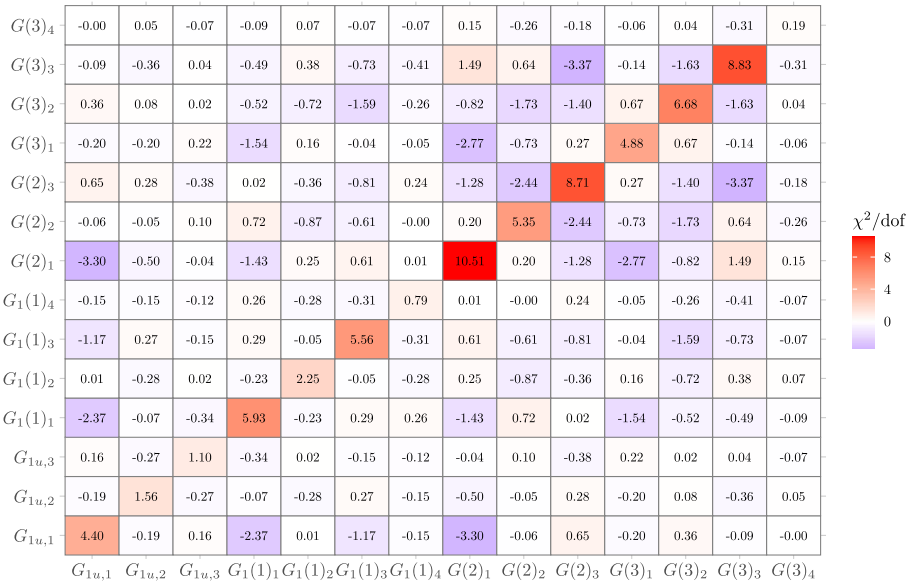

FIG. 48. Heat map of correlated $\chi^2{}_{ij}/14$, highlighting the relative impact of each energy level on the total fit quality.

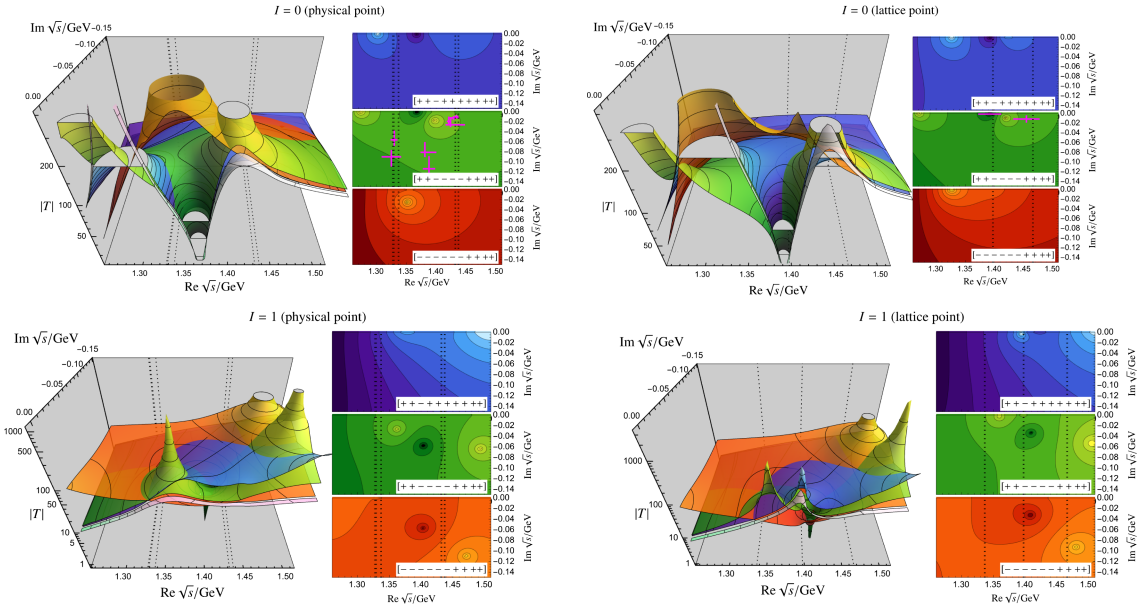

FIG. 49. Isoscalar and isovector projected absolute value of the $\pi\Sigma \to \pi\Sigma$ scattering amplitude on the unphysical second Riemann sheets. Nomenclature as in the main text. Magenta crosses represent literature values from Refs. [20,21] for the lattice point and Refs. [12,13,50] for the physical point.

4. M2S1P (F_{22})

$\chi^2_{\rm dof}$	8.86
$a_{\bar{K}N}$	-1.670707e-03
$a_{\pi\Lambda}$	2.465099e-02
$a_{\pi\Sigma}$	-3.528238e-03
$a_{\eta\Lambda}$	-5.376287e-03
$a_{\eta\Sigma}$	-1.070200e-02
$a_{K\Xi}$	-1.305735e-02

FIG. 50. The total $\chi^2_{\rm dof}$, as defined in Eq. (5.1), and subtraction constants for M2S1P (F_{22}).

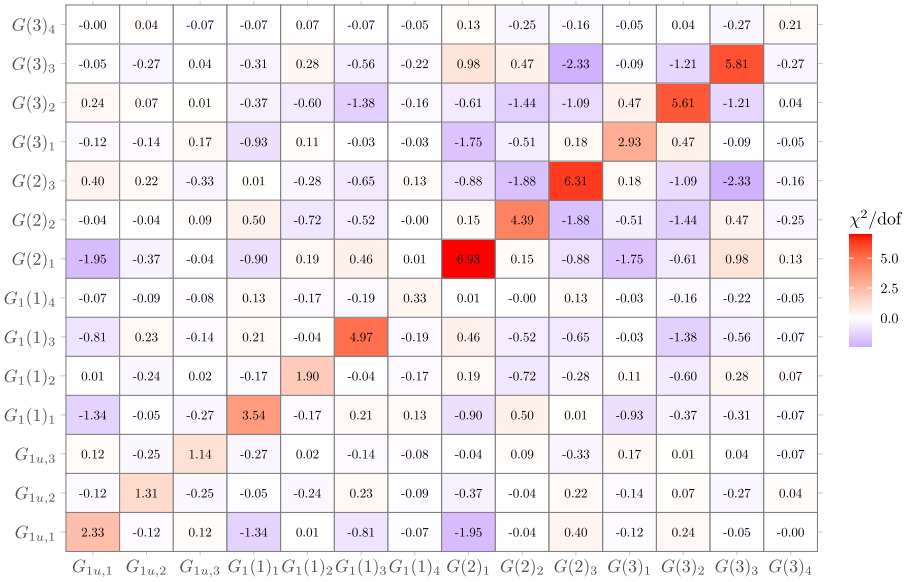

FIG. 51. Heat map of correlated $\chi^2{}_{ij}/14$, highlighting the relative impact of each energy level on the total fit quality.

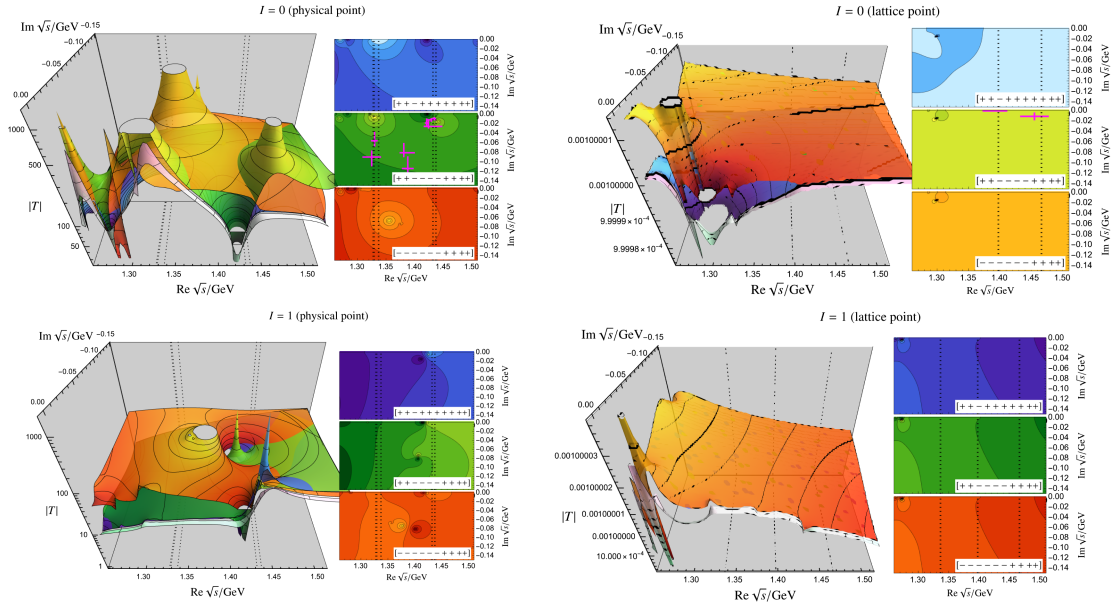

FIG. 52. Isoscalar and isovector projected absolute value of the $\pi\Sigma \to \pi\Sigma$ scattering amplitude on the unphysical second Riemann sheets. Nomenclature as in the main text. Magenta crosses represent literature values from Refs. [20,21] for the lattice point and Refs. [12,13,50] for the physical point.

5. M2S2P (F_{29})

χ^2_{dof}	48.15

FIG. 53. The total χ^2_{dof}, as defined in Eq. (5.1), for the parameter-free fit, M2S2P (F_{29}).

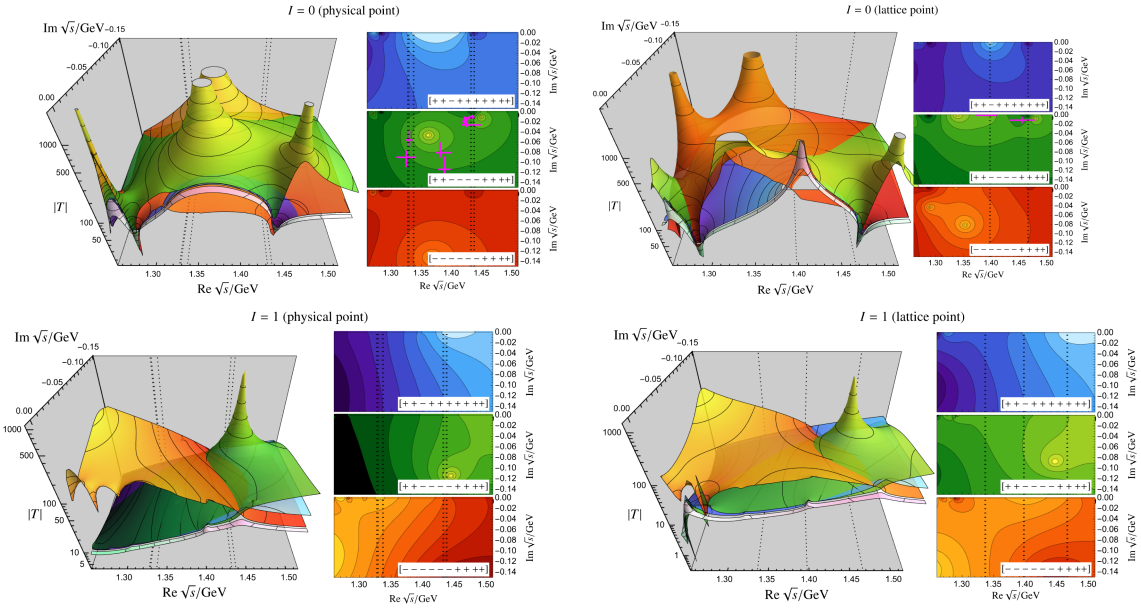

FIG. 54. Isoscalar and isovector projected absolute value of the $\pi\Sigma \to \pi\Sigma$ scattering amplitude on the unphysical second Riemann sheets. Nomenclature as in the main text. Magenta crosses represent literature values from Refs. [20,21] for the lattice point and Refs. [12,13,50] for the physical point.

6. M2S3P (F_{26})

$\chi^2_{\rm dof}$	18.69
Λ[GeV]	1.087866

FIG. 55. The total $\chi^2_{\rm dof}$, as defined in Eq. (5.1), and the Λ parameter for M2S3P (F_{26}).

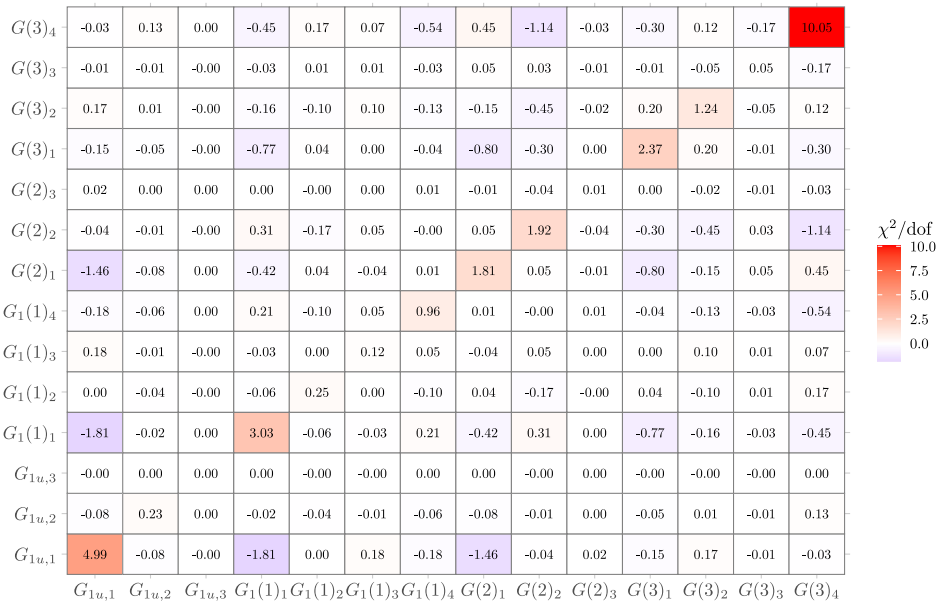

FIG. 56. Heat map of correlated $\chi^2_{{\rm dof},ij}$, highlighting the relative impact of each energy level on the total fit quality.

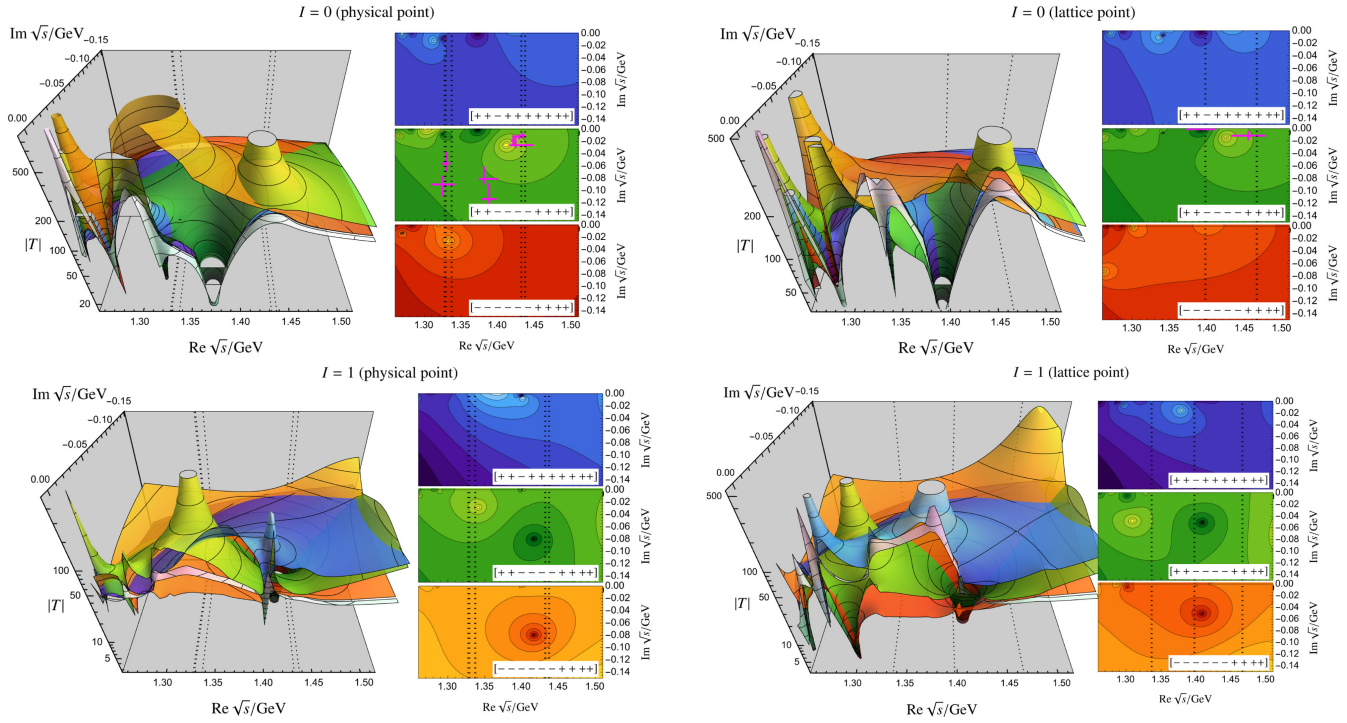

FIG. 57. Isoscalar and isovector projected absolute value of the $\pi\Sigma \to \pi\Sigma$ scattering amplitude on the unphysical second Riemann sheets. Nomenclature as in the main text. Magenta crosses represent literature values from Refs. [20,21] for the lattice point and Refs. [12,13,50] for the physical point.

7. M3S1P (F_{30})

χ^2_{dof}	1.51
$a_{\bar{K}N}$	8.684939e-05
$a_{\pi\Lambda}$	6.602418e-02
$a_{\pi\Sigma}$	-3.019298e-03
$a_{\eta\Lambda}$	6.760390e-03
$a_{\eta\Sigma}$	-6.407026e-03
$a_{K\Xi}$	3.279341e-03
$b_0[1/\text{GeV}]$	-6.277105e-01
$b_D[1/\text{GeV}]$	-3.489336e-01
$b_F[1/\text{GeV}]$	-2.942295e-01
$d_1[1/\text{GeV}]$	-1.759572e-01
$d_2[1/\text{GeV}]$	-1.042583e-01
$d_3[1/\text{GeV}]$	-4.012072e-01
$d_4[1/\text{GeV}]$	-1.576405e-01

FIG. 58. The total χ^2_{dof}, as defined in Eq. (5.1), subtraction constants, and LECs for M3S1P (F_{30}).

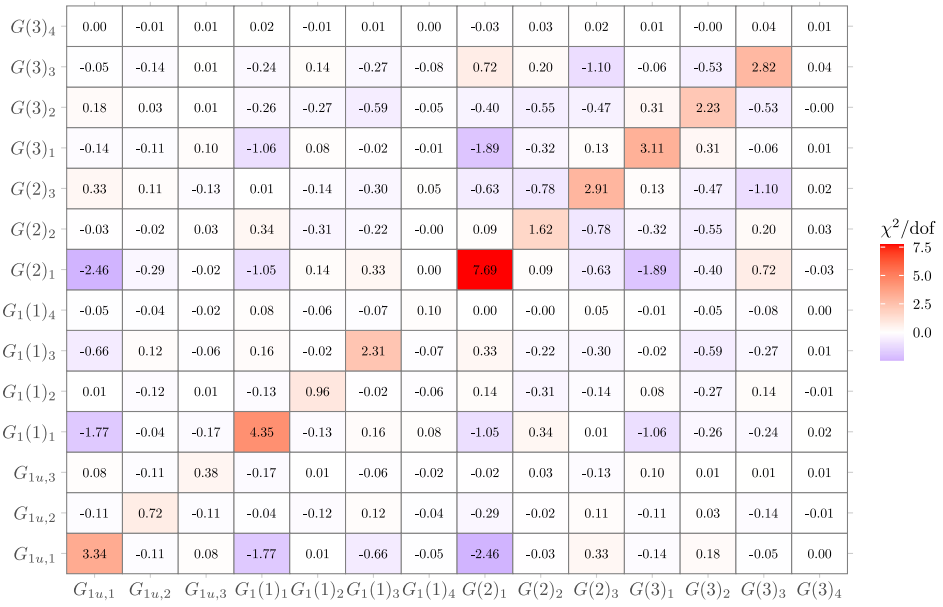

FIG. 59. Heat map of correlated $\chi^2_{\text{dof},ij}$, highlighting the relative impact of each energy level on the total fit quality.

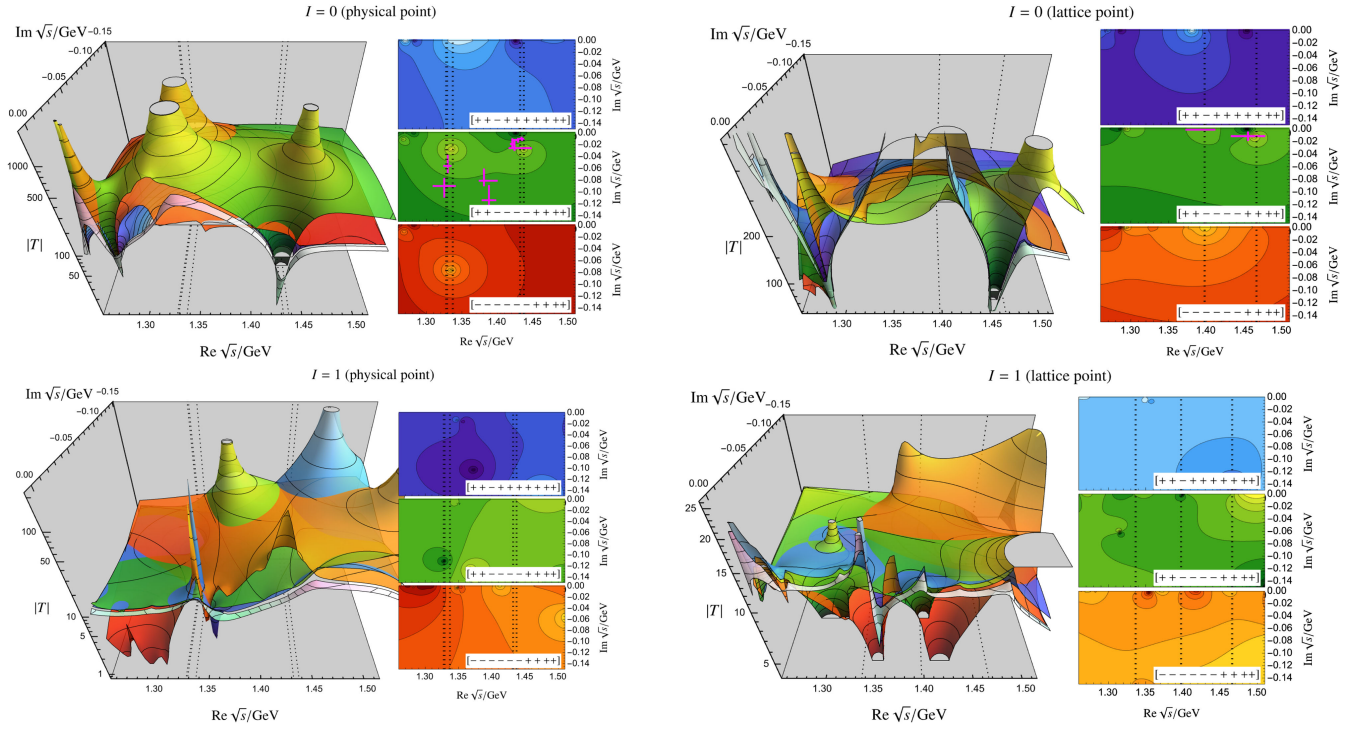

FIG. 60. Isoscalar and isovector projected absolute value of the $\pi\Sigma \to \pi\Sigma$ scattering amplitude on the unphysical second Riemann sheets. Nomenclature as in the main text. Magenta crosses represent literature values from Refs. [20,21] for the lattice point and Refs. [12,13,50] for the physical point.

8. M3S2P (F_{13})

$\chi^2_{\rm dof}$	0.90
$b_0[1/\text{GeV}]$	-5.349500e-01
$b_D[1/\text{GeV}]$	9.599595e-02
$b_F[1/\text{GeV}]$	-3.256764e-01
$d_1[1/\text{GeV}]$	-8.386487e-01
$d_2[1/\text{GeV}]$	1.518967e-01
$d_3[1/\text{GeV}]$	-4.546126e-01
$d_4[1/\text{GeV}]$	7.207285e-03

FIG. 61. The total $\chi^2_{\rm dof}$, as defined in Eq. (5.1), and LECs for Fit 13 (M3S2P).

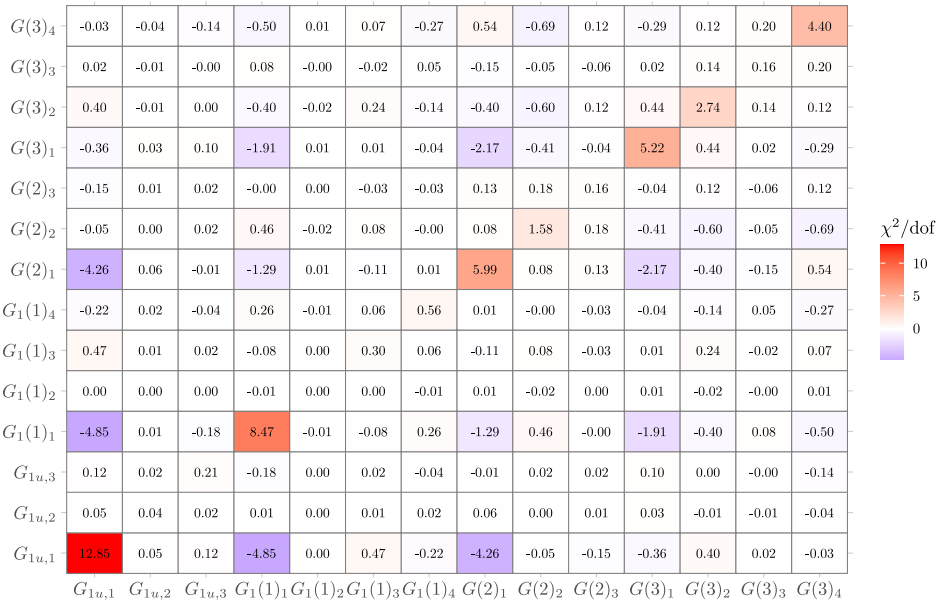

FIG. 62. Heat map of correlated $\chi^2_{{\rm dof},ij}$, highlighting the relative impact of each energy level on the total fit quality.

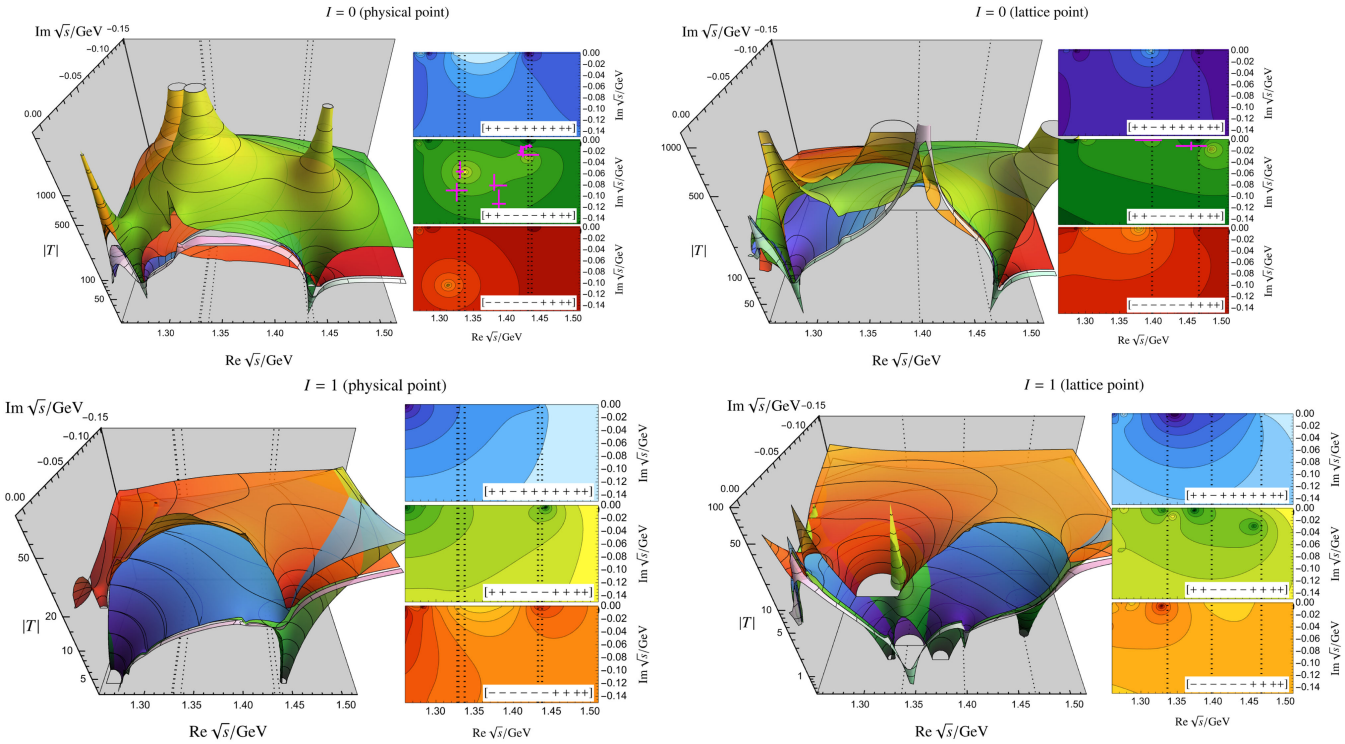

FIG. 63. Isoscalar and isovector projected absolute value of the $\pi\Sigma \to \pi\Sigma$ scattering amplitude on the unphysical second Riemann sheets. Nomenclature as in the main text. Magenta crosses represent literature values from Refs. [20,21] for the lattice point and Refs. [12,13,50] for the physical point.

9. M3S3P (F_{11})

χ^2_{dof}	1.46
Λ[GeV]	0.6802625
b_0[1/GeV]	-5.440114e-01
b_D[1/GeV]	-8.008565e-01
b_F[1/GeV]	-4.127402e-01
d_1[1/GeV]	-4.572182e-01
d_2[1/GeV]	-2.716873e-01
d_3[1/GeV]	-6.182698e-01
d_4[1/GeV]	-9.100890e-01

FIG. 64. The total χ^2_{dof}, as defined in Eq. (5.1), Λ parameter, and LECs for M3S3P (F_{11}).

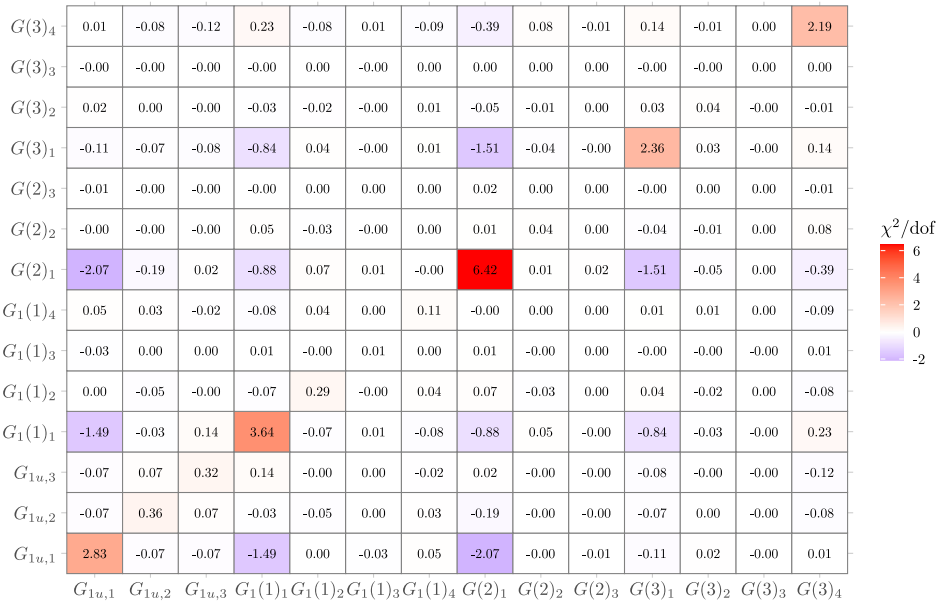

FIG. 65. Heat map of correlated $\chi^2_{\text{dof},ij}$, highlighting the relative impact of each energy level on the total fit quality.

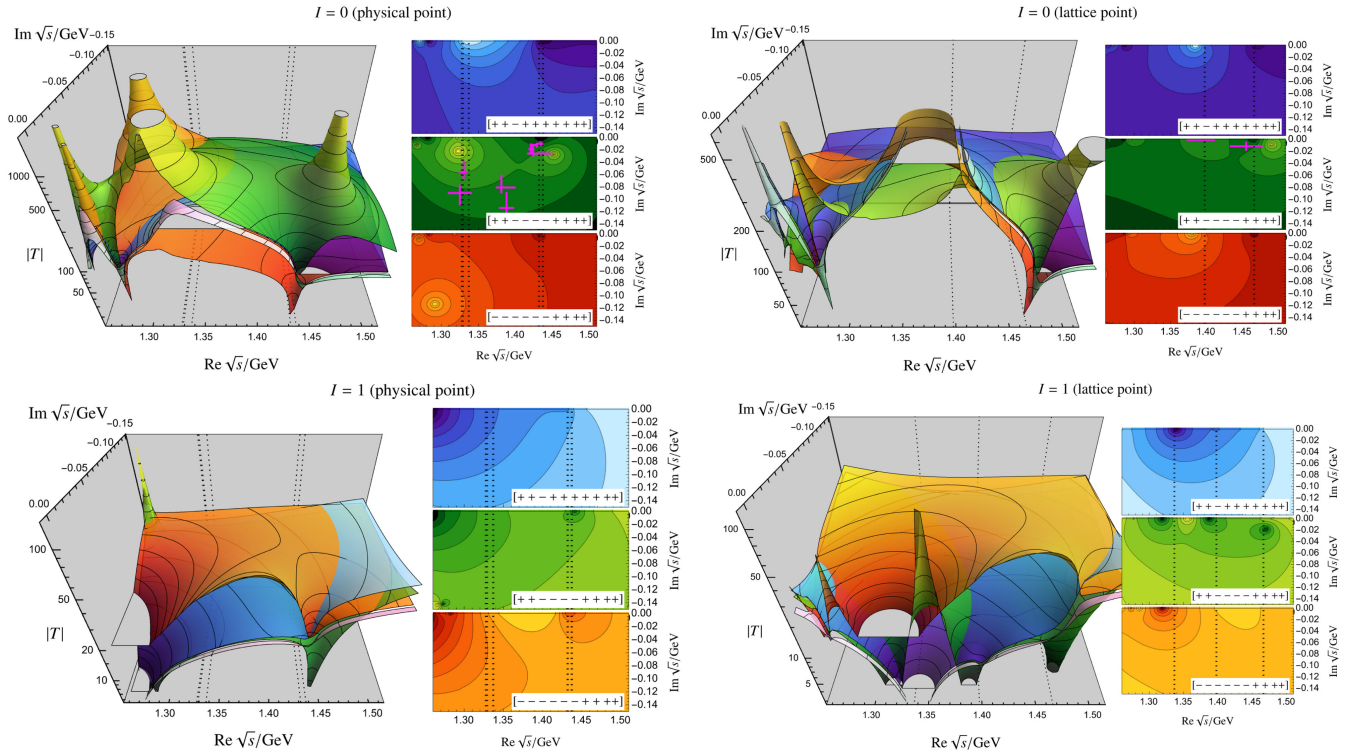

FIG. 66. Isoscalar and isovector projected absolute value of the $\pi\Sigma \to \pi\Sigma$ scattering amplitude on the unphysical second Riemann sheets. Nomenclature as in the main text. Magenta crosses represent literature values from Refs. [20,21] for the lattice point and Refs. [12,13,50] for the physical point.

APPENDIX C: DETAILED FIT RESULTS: COMBINED FITS TO THE EXPERIMENTAL DATA AND LATTICE INPUT

1. M1S3PL (F_{24})

χ^2_{dof}	27.56447
Λ[GeV]	0.8106917

FIG. 67. The total χ^2_{dof}, as defined in Eq. (5.1), and the Λ parameter for M1S3PL (F_{24}).

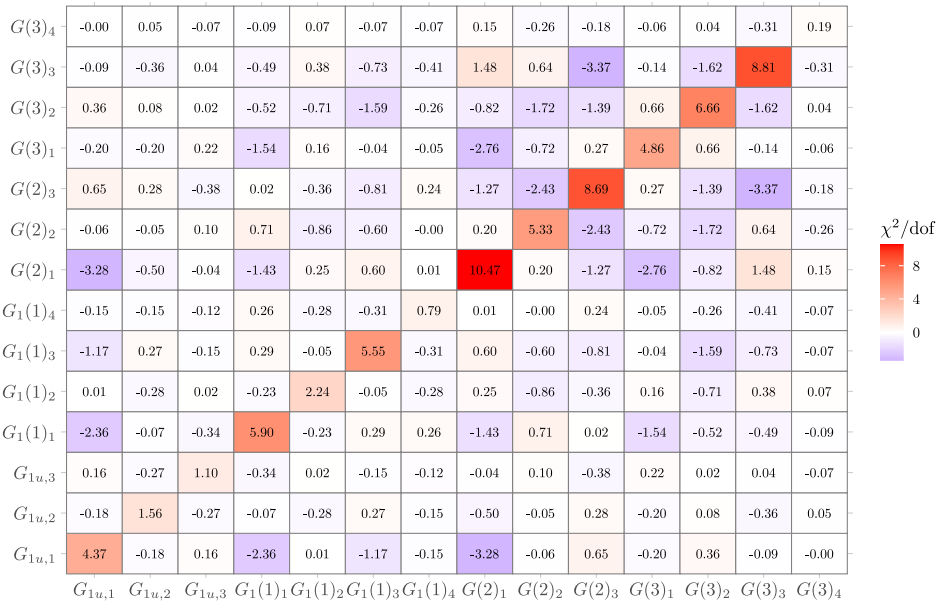

FIG. 68. Heat map of correlated $\chi^2_{\text{dof},ij}$, highlighting the relative impact of each energy level on the total fit quality.

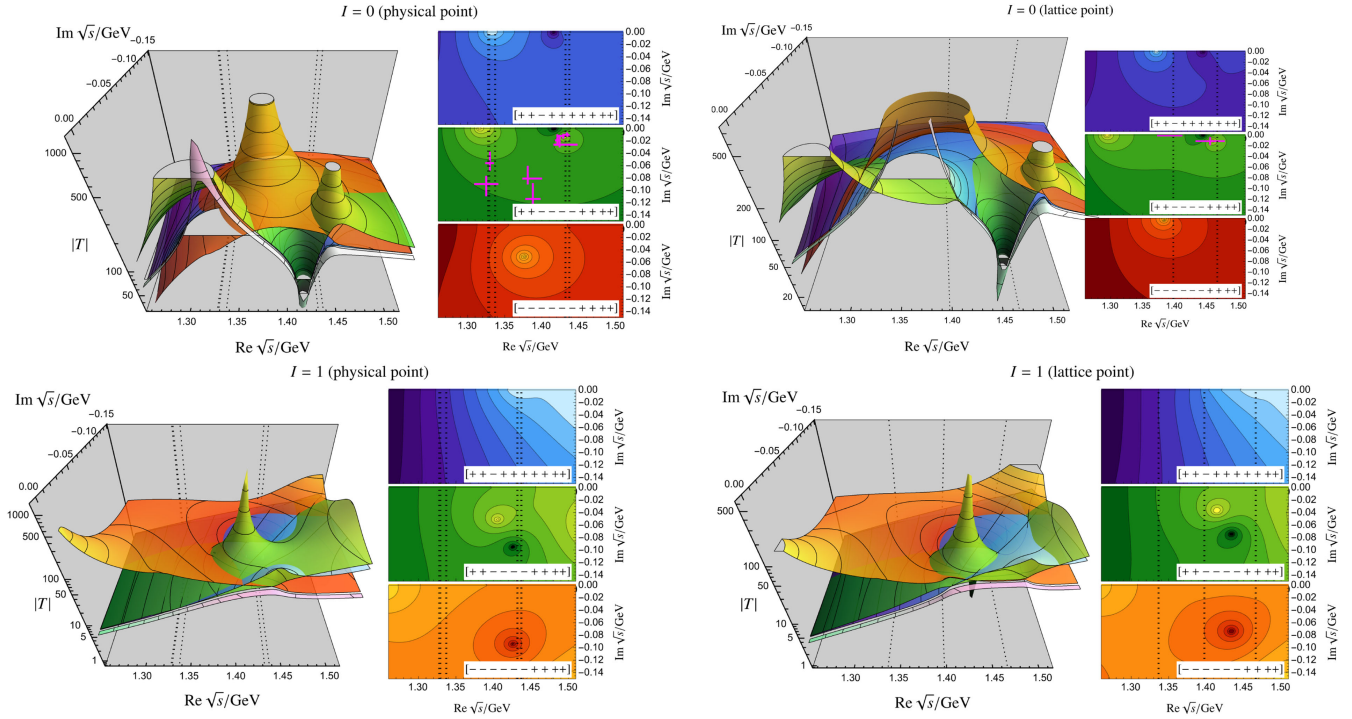

FIG. 69. Isoscalar and isovector projected absolute value of the $\pi\Sigma \to \pi\Sigma$ scattering amplitude on the unphysical second Riemann sheets. Nomenclature as in the main text. Magenta crosses represent literature values from Refs. [20,21] for the lattice point and Refs. [12,13,50] for the physical point.

2. M2S3PL (F_{23})

χ^2_{dof}	17.81
Λ[GeV]	1.088185

FIG. 70. The total χ^2_{dof}, as defined in Eq. (5.1), and the Λ parameter for M2S3PL (F_{23}).

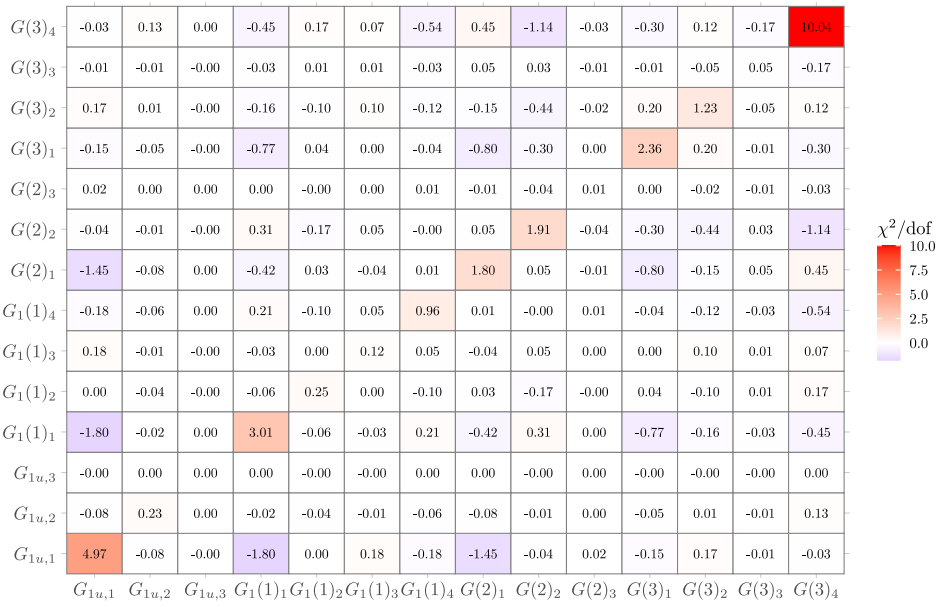

FIG. 71. Heat map of correlated $\chi^2_{\text{dof},ij}$, highlighting the relative impact of each energy level on the total fit quality.

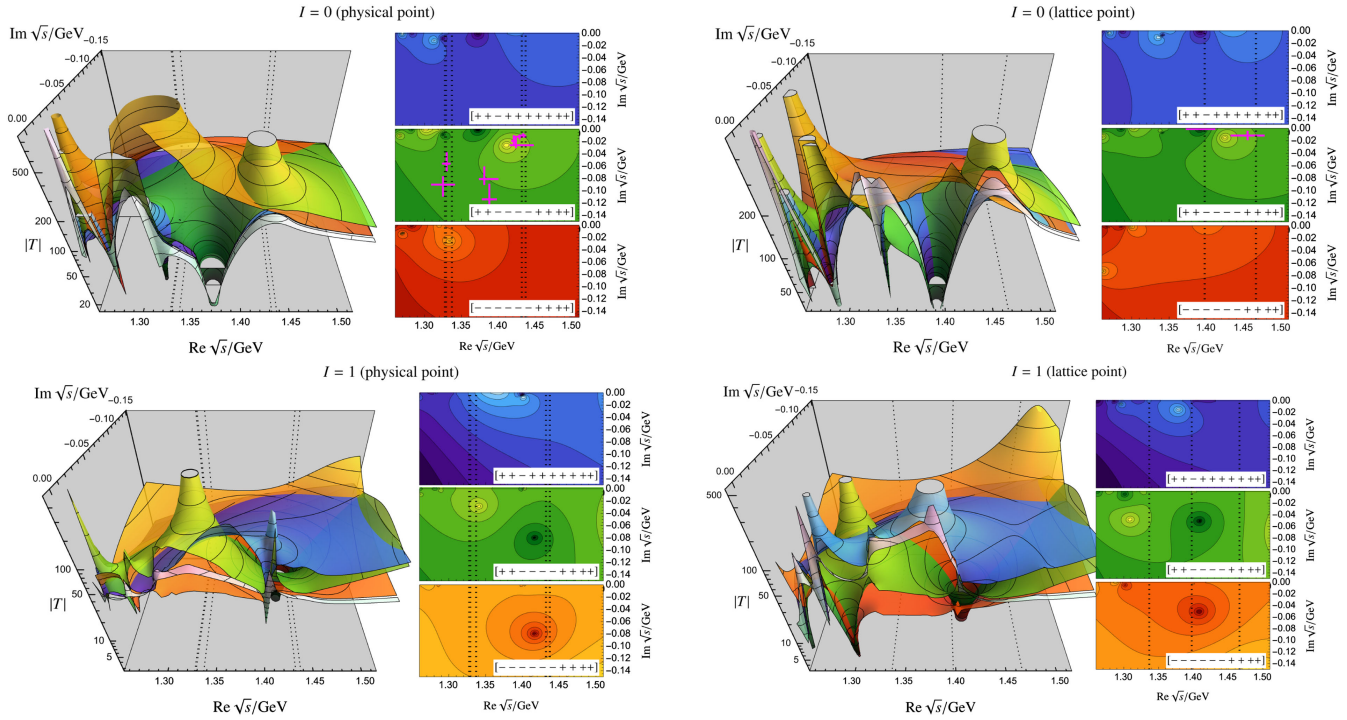

FIG. 72. Isoscalar and isovector projected absolute value of the $\pi\Sigma \to \pi\Sigma$ scattering amplitude on the unphysical second Riemann sheets. Nomenclature as in the main text. Magenta crosses represent literature values from Refs. [20,21] for the lattice point and Refs. [12,13,50] for the physical point.

3. M3S1PL (F_{17})

χ^2_{dof}	1.441434	
	Lattice	Experimental
$a_{\bar{K}N}$	-1.564779e-03	-1.546676e-03
$a_{\pi\Lambda}$	-1.079700e-01	8.517151e-02
$a_{\pi\Sigma}$	+3.721385e-03	-2.728888e-03
$a_{\eta\Lambda}$	+1.376050e-02	9.982057e-03
$a_{\eta\Sigma}$	+2.163700e-01	-5.741158e-03
$a_{K\Xi}$	+3.948000e-02	8.712392e-02
b_0[1/GeV]	-6.569390e-01	
b_D[1/GeV]	6.740337e-02	
b_F[1/GeV]	-3.257189e-01	
d_1[1/GeV]	-2.520795e-01	
d_2[1/GeV]	3.095445e-02	
d_3[1/GeV]	-8.990016e-02	
d_4[1/GeV]	-5.497259e-02	

FIG. 73. The total χ^2_{dof}, as defined in Eq. (5.1), subtraction constants for both the lattice and the physical points, and LECs for M3S1PL (F_{17}).

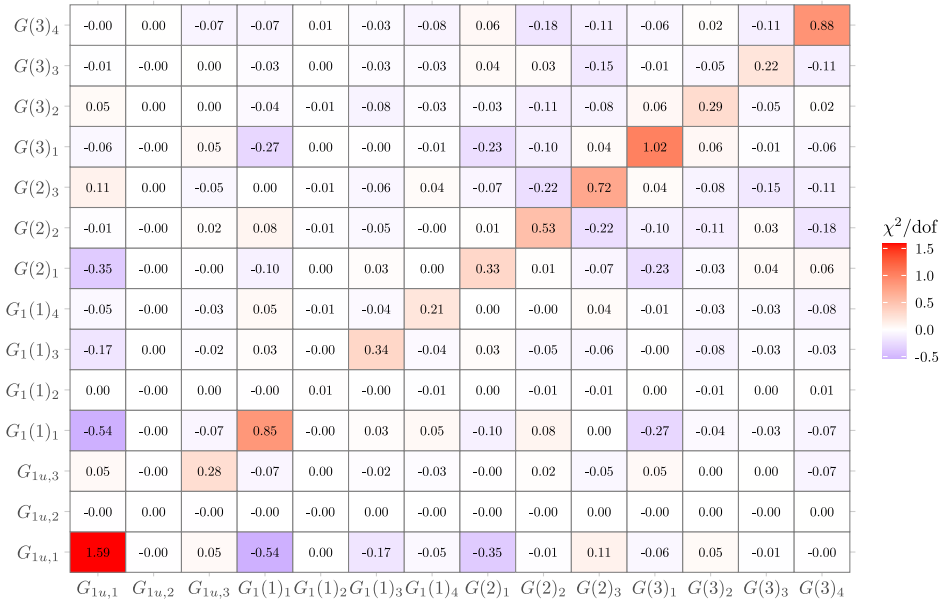

FIG. 74. Heat map of correlated $\chi^2_{\text{dof},ij}$, highlighting the relative impact of each energy level on the total fit quality.

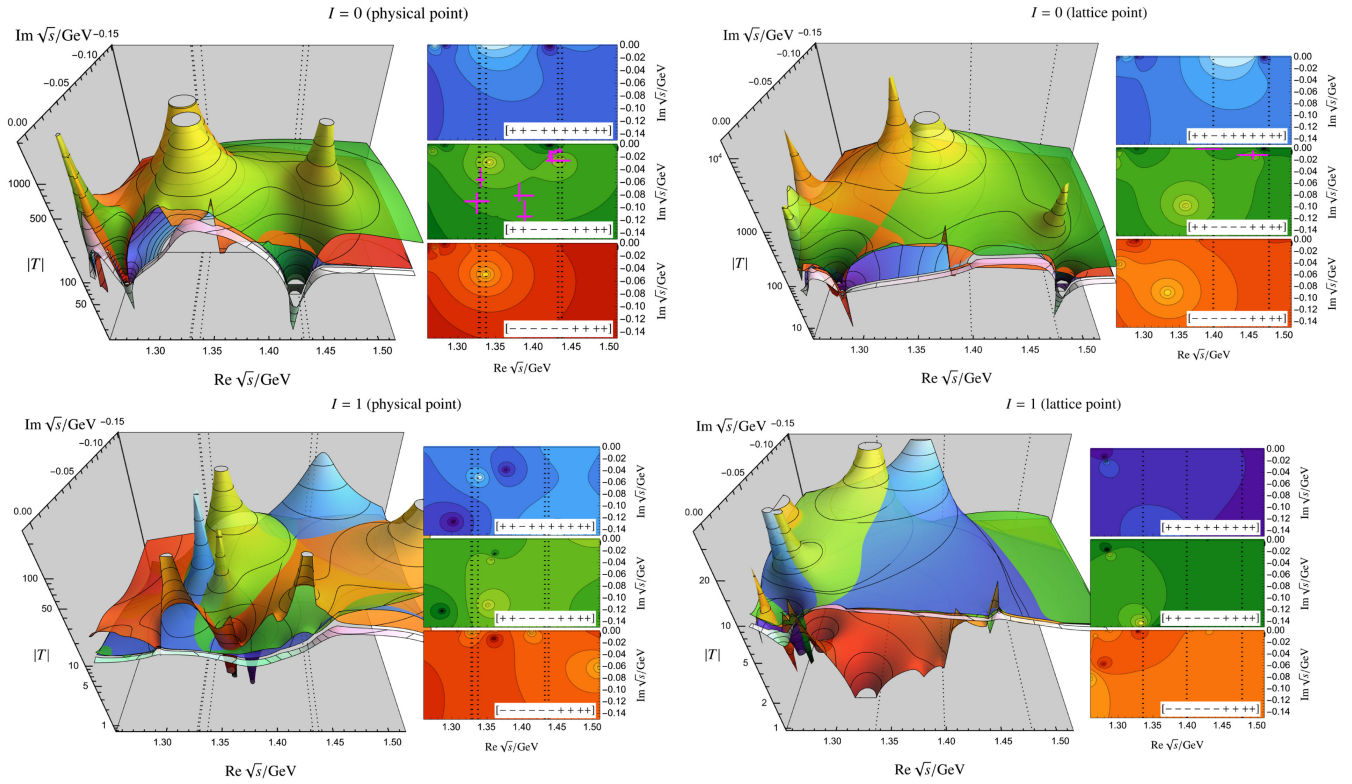

FIG. 75. Isoscalar and isovector projected absolute value of the $\pi\Sigma \to \pi\Sigma$ scattering amplitude on the unphysical second Riemann sheets. Nomenclature as in the main text. Magenta crosses represent literature values from Refs. [20,21] for the lattice point and Refs. [12,13,50] for the physical point.

4. M3S2PL (F_{16})

χ^2_{dof}	2.1189
$b_0[1/\text{GeV}]$	-3.414328e-01
$b_D[1/\text{GeV}]$	6.368574e-02
$b_F[1/\text{GeV}]$	-3.021744e-01
$d_1[1/\text{GeV}]$	-2.593481e-01
$d_2[1/\text{GeV}]$	4.433054e-02
$d_3[1/\text{GeV}]$	3.431286e-02
$d_4[1/\text{GeV}]$	-3.704632e-01

FIG. 76. The total χ^2_{dof}, as defined in Eq. (5.1), and LECs for M3S2PL (F_{16}).

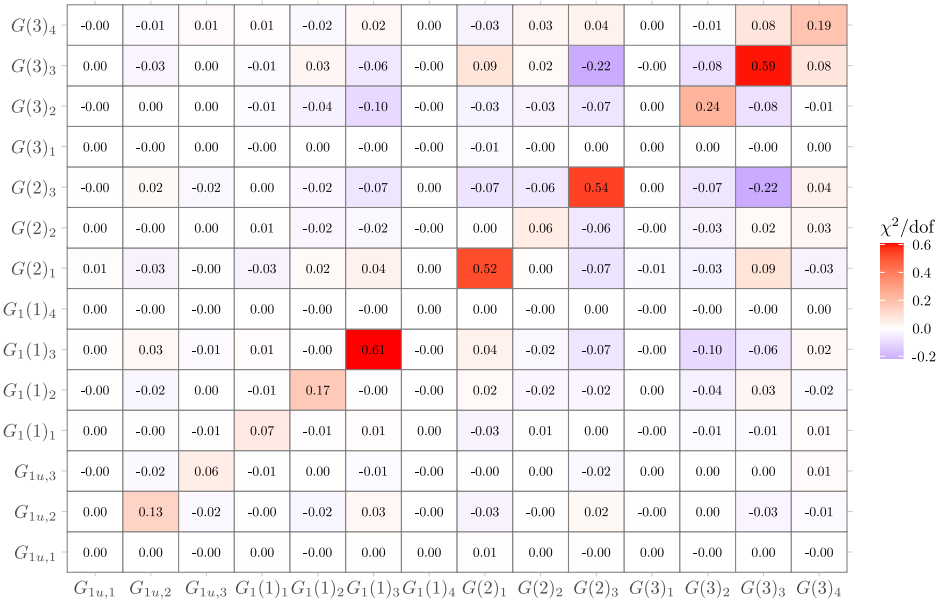

FIG. 77. Heat map of correlated $\chi^2_{\text{dof},ij}$, highlighting the relative impact of each energy level on the total fit quality.

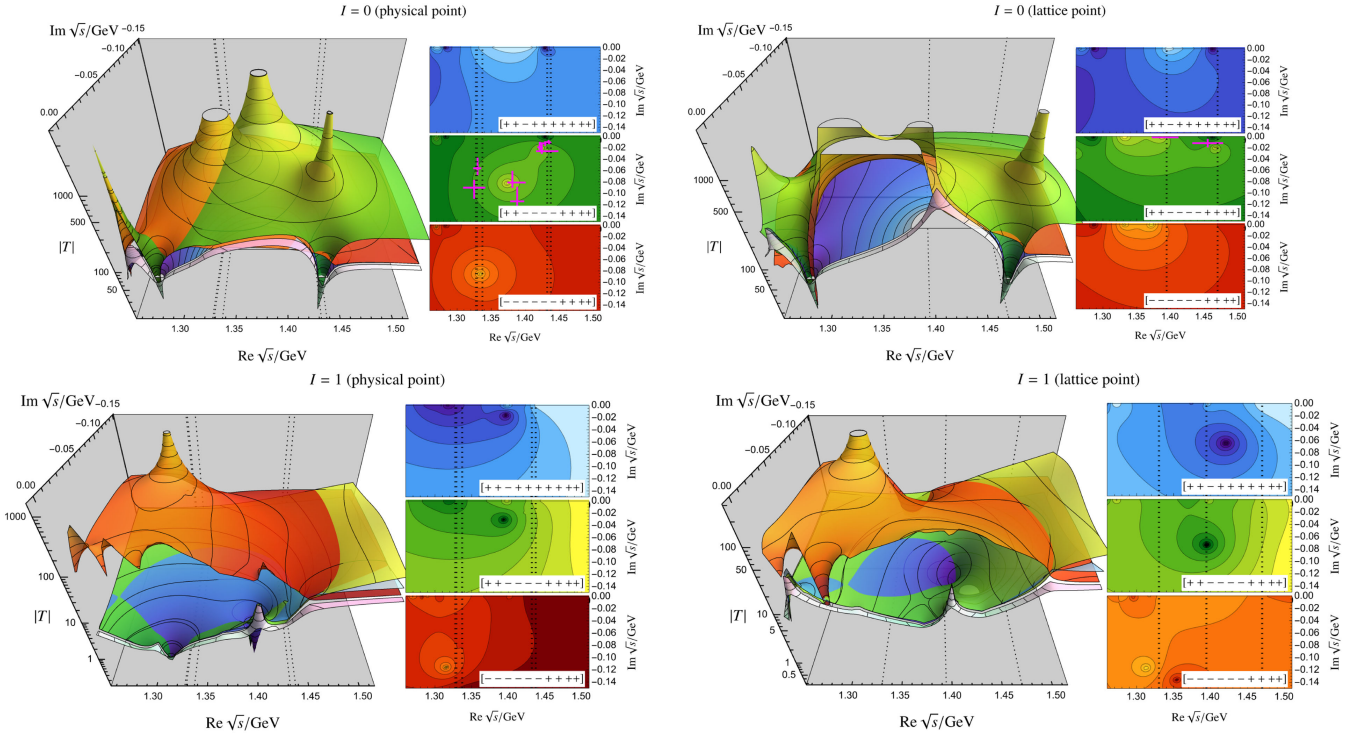

FIG. 78. Isoscalar and isovector projected absolute value of the $\pi\Sigma \to \pi\Sigma$ scattering amplitude on the unphysical second Riemann sheets. Nomenclature as in the main text. Magenta crosses represent literature values from Refs. [20,21] for the lattice point and Refs. [12,13,50] for the physical point.

5. M3S3PL (F_{12})

χ^2_{dof}	2.236
Λ[GeV]	0.4218104
b_0[1/GeV]	-8.768647e-01
b_D[1/GeV]	5.246210e-02
b_F[1/GeV]	-3.406325e-01
d_1[1/GeV]	1.201660e+00
d_2[1/GeV]	-1.753693e-01
d_3[1/GeV]	-4.544383e-01
d_4[1/GeV]	1.476738e-01

FIG. 79. The total χ^2_{dof}, as defined in Eq. (5.1), Λ parameter, and LECs for M3S3PL (F_{12}).

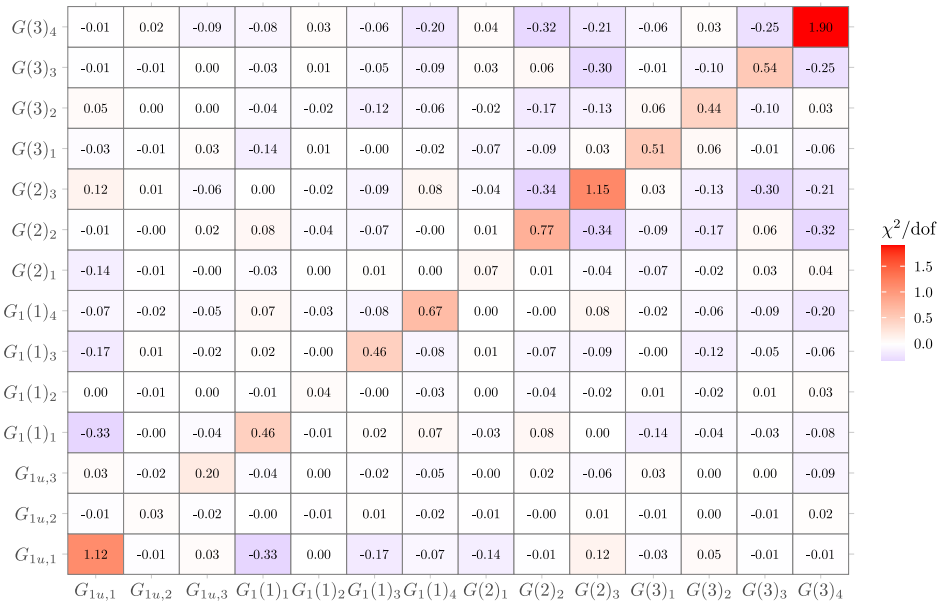

FIG. 80. Heat map of correlated $\chi^2_{\text{dof},ij}$, highlighting the relative impact of each energy level on the total fit quality.

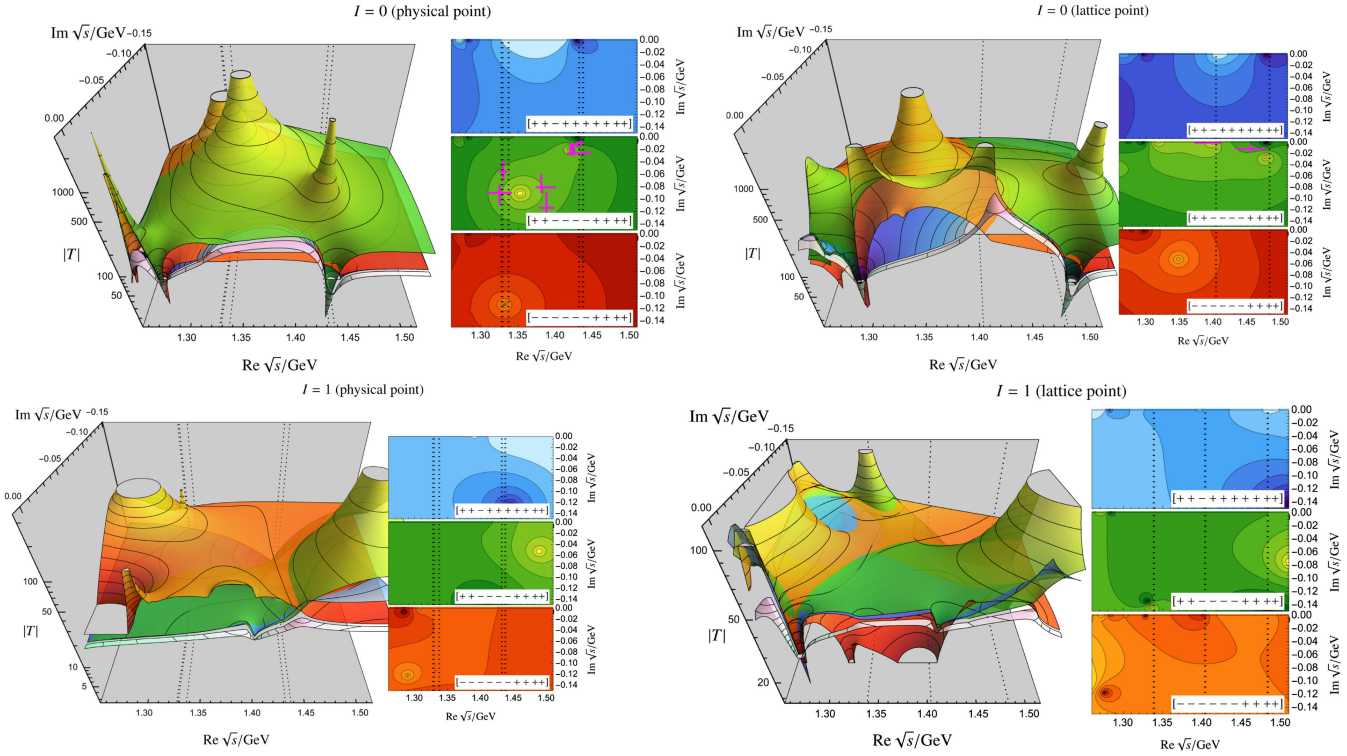

FIG. 81. Isoscalar and isovector projected absolute value of the $\pi\Sigma \to \pi\Sigma$ scattering amplitude on the unphysical second Riemann sheets. Nomenclature as in the main text. Magenta crosses represent literature values from Refs. [20,21] for the lattice point and Refs. [12,13,50] for the physical point.

[1] S. Navas *et al.* (Particle Data Group), Review of particle physics, Phys. Rev. D **110**, 030001 (2024).

[2] Annika Thiel, Farah Afzal, and Yannick Wunderlich, Light baryon spectroscopy, Prog. Part. Nucl. Phys. **125**, 103949 (2022).

[3] Gernot Eichmann, Helios Sanchis-Alepuz, Richard Williams, Reinhard Alkofer, and Christian S. Fischer, Baryons as relativistic three-quark bound states, Prog. Part. Nucl. Phys. **91**, 1 (2016).

[4] Michael Döring, Johann Haidenbauer, Maxim Mai, and Toru Sato, Dynamical coupled-channel models for hadron dynamics, arXiv:2505.02745.

[5] Maxim Mai, Ulf-G. Meißner, and Carsten Urbach, Towards a theory of hadron resonances, Phys. Rep. **1001**, 1 (2023).

[6] Volker Burkert, Gernot Eichmann, and Eberhard Klempt, The impact of γN and $\gamma^* N$ interactions on our understanding of nucleon excitations, arXiv:2506.16482.

[7] J. A. Oller and Ulf-G. Meißner, Chiral dynamics in the presence of bound states: Kaon nucleon interactions revisited, Phys. Lett. B **500**, 263 (2001).

[8] Ulf-G. Meißner, Two-pole structures in QCD: Facts, not fantasy! Symmetry **12**, 981 (2020).

[9] Maxim Mai, Review of the Λ(1405) A curious case of a strangeness resonance, Eur. Phys. J. Special Topics **230**, 1593 (2021).

[10] Tetsuo Hyodo and Masayuki Niiyama, QCD and the strange baryon spectrum, Prog. Part. Nucl. Phys. **120**, 103868 (2021).

[11] A. Cieplý, M. Mai, Ulf-G. Meißner, and J. Smejkal, On the pole content of coupled channels chiral approaches used for the $\bar{K}N$ system, Nucl. Phys. **A954**, 17 (2016).

[12] Yoichi Ikeda, Tetsuo Hyodo, and Wolfram Weise, Chiral SU(3) theory of antikaon-nucleon interactions with improved threshold constraints, Nucl. Phys. **A881**, 98 (2012).

[13] Zhi-Hui Guo and J. A. Oller, Meson-baryon reactions with strangeness −1 within a chiral framework, Phys. Rev. C **87**, 035202 (2013).

[14] Jun-Xu Lu, Li-Sheng Geng, Michael Doering, and Maxim Mai, Cross-channel constraints on resonant antikaon-nucleon scattering, Phys. Rev. Lett. **130**, 071902 (2023).

[15] Benjamin J. Menadue, Waseem Kamleh, Derek B. Leinweber, and M. Selim Mahbub, Isolating the Λ(1405) in lattice QCD, Phys. Rev. Lett. **108**, 112001 (2012).

[16] Georg P. Engel, C. B. Lang, and Andreas Schäfer (BGR (Bern-Graz-Regensburg) Collaboration), Low-lying Λ baryons from the lattice, Phys. Rev. D **87**, 034502 (2013).

[17] Robert G. Edwards, Nilmani Mathur, David G. Richards, and Stephen J. Wallace (Hadron Spectrum Collaboration), Flavor structure of the excited baryon spectra from lattice QCD, Phys. Rev. D **87**, 054506 (2013).

[18] Jonathan M. M. Hall, Waseem Kamleh, Derek B. Leinweber, Benjamin J. Menadue, Benjamin J. Owen, Anthony W. Thomas, and Ross D. Young, Lattice QCD evidence that the Λ(1405) resonance is an antikaon-nucleon molecule, Phys. Rev. Lett. **114**, 132002 (2015).

[19] Jonathan M. M. Hall, Waseem Kamleh, Derek B. Leinweber, Benjamin J. Menadue, Benjamin J. Owen, Anthony W. Thomas, and Ross D. Young, On the structure of the Lambda 1405, Proc. Sci., LATTICE2014 (**2014**) 094 [arXiv:1411.3781].

[20] John Bulava *et al.* (Baryon Scattering (BaSc) Collaboration), Lattice QCD study of $\pi\Sigma$-K^- N scattering and the Λ(1405) resonance, Phys. Rev. D **109**, 014511 (2024).

[21] John Bulava *et al.* (Baryon Scattering (BaSc) Collaboration), Two-pole nature of the Λ(1405) resonance from lattice QCD, Phys. Rev. Lett. **132**, 051901 (2024).

[22] Colin Morningstar, Nucleon scattering from lattice QCD, in *11th International Workshop on Chiral Dynamics* (2025), arXiv:2504.01950.

[23] Raul A. Briceno, Jozef J. Dudek, and Ross D. Young, Scattering processes and resonances from lattice QCD, Rev. Mod. Phys. **90**, 025001 (2018).

[24] Martin Lüscher, Two particle states on a torus and their relation to the scattering matrix, Nucl. Phys. **B354**, 531 (1991).

[25] Martin Lüscher, Signatures of unstable particles in finite volume, Nucl. Phys. **B364**, 237 (1991).

[26] K. Rummukainen and Steven A. Gottlieb, Resonance scattering phase shifts on a nonrest frame lattice, Nucl. Phys. **B450**, 397 (1995).

[27] C. h. Kim, C. T. Sachrajda, and Stephen R. Sharpe, Finite-volume effects for two-hadron states in moving frames, Nucl. Phys. **B727**, 218 (2005).

[28] Song He, Xu Feng, and Chuan Liu, Two particle states and the S-matrix elements in multi-channel scattering, J. High Energy Phys. 07 (2005) 011.

[29] Michael Lage, Ulf-G. Meißner, and Akaki Rusetsky, A method to measure the antikaon-nucleon scattering length in lattice QCD, Phys. Lett. B **681**, 439 (2009).

[30] Raul A. Briceno, Two-particle multichannel systems in a finite volume with arbitrary spin, Phys. Rev. D **89**, 074507 (2014).

[31] V. Bernard, M. Lage, U.-G. Meißner, and A. Rusetsky, Scalar mesons in a finite volume, J. High Energy Phys. 01 (2011) 019.

[32] M. Göckeler, R. Horsley, M. Lage, U.-G. Meißner, P. E. L. Rakow, A. Rusetsky, G. Schierholz, and J. M. Zanotti, Scattering phases for meson and baryon resonances on general moving-frame lattices, Phys. Rev. D **86**, 094513 (2012).

[33] Peter C. Bruns, Maxim Mai, and Ulf-G. Meißner, Chiral dynamics of the S11(1535) and S11(1650) resonances revisited, Phys. Lett. B **697**, 254 (2011).

[34] Maxim Mai and Ulf-G. Meißner, New insights into antikaon-nucleon scattering and the structure of the Lambda(1405). Nucl. Phys. **A900**, 51 (2013).

[35] Daniel Sadasivan, Maxim Mai, Michael Döring, Ulf-G. Meißner, Felipe Amorim, John Paul Klucik, Jun-Xu Lu, and Li-Sheng Geng, New insights into the pole parameters of the Λ(1380), the Λ(1405) and the Σ(1385), Front. Phys. **11**, 1139236 (2023).

[36] G. Höhler, *Methods and Results of Phenomenological Analyses / Methoden und Ergebnisse phänomenologischer Analysen*, edited by H. Schopper, Landolt-Boernstein—Group I Elementary Particles, Nuclei and Atoms, Vol. 9b2 (Springer, New York, 1983).

[37] G. F. Chew, M. L. Goldberger, F. E. Low, and Y. Nambu, Application of dispersion relations to low-energy meson-nucleon scattering, Phys. Rev. **106**, 1337 (1957).

[38] Colin Morningstar, John Bulava, Bijit Singha, Ruairí Brett, Jacob Fallica, Andrew Hanlon, and Ben Hörz, Estimating the two-particle K-matrix for multiple partial waves and decay channels from finite-volume energies, Nucl. Phys. **B924**, 477 (2017).

[39] Yu Lu, Hao-Jie Jing, and Jia-Jun Wu, Phase conventions in hadron physics from the perspective of the quark model, Symmetry **16**, 1061 (2024).

[40] Mattia Bruno *et al.*, Simulation of QCD with $N_f = 2 + 1$ flavors of non-perturbatively improved Wilson fermions, J. High Energy Phys. 02 (2015) 043.

[41] Michael Peardon, John Bulava, Justin Foley, Colin Morningstar, Jozef Dudek, Robert G. Edwards, Balint Joo, Huey-Wen Lin, David G. Richards, and Keisuke Jimmy Juge (Hadron Spectrum Collaboration), A novel quark-field creation operator construction for hadronic physics in lattice QCD, Phys. Rev. D **80**, 054506 (2009).

[42] Colin Morningstar, John Bulava, Justin Foley, Keisuke J. Juge, David Lenkner, Mike Peardon, and Chik Him Wong, Improved stochastic estimation of quark propagation with Laplacian heaviside smearing in lattice QCD, Phys. Rev. D **83**, 114505 (2011).

[43] Bárbara Cid-Mora *et al.*, The $\Lambda(1405)$ from lattice QCD: Determining the finite-volume spectra, Proc. Sci., LATTICE2023 (**2024**) 131 [arXiv:2312.05154].

[44] Masayuki Niiyama (LEPS TPC Collaboration), Photoproduction of $\Sigma^0(1385)$ and $\Lambda(1405)$ on the proton near threshold, Nucl. Phys. **A827**, 261C (2009).

[45] K. Moriya *et al.* (CLAS Collaboration), Measurement of the $\Sigma\pi$ photoproduction line shapes near the $\Lambda(1405)$, Phys. Rev. C **87**, 035206 (2013).

[46] K. Moriya *et al.* (CLAS Collaboration), Differential photoproduction cross sections of the $\Sigma^0(1385)$, $\Lambda(1405)$, and $\Lambda(1520)$, Phys. Rev. C **88**, 045201 (2013); **88**, 049902(A) (2013).

[47] G. Scheluchin *et al.* (BGOOD Collaboration), Photoproduction of $K^+\Lambda(1405) \to K^+\pi^0\Sigma^0$ extending to forward angles and low momentum transfer, Phys. Lett. B **833**, 137375 (2022).

[48] A. V. Anisovich, A. V. Sarantsev, V. A. Nikonov, V. Burkert, R. A. Schumacher, U. Thoma, and E. Klempt, Hyperon III: $K^-p - \pi\Sigma$ coupled-channel dynamics in the $\Lambda(1405)$ mass region, Eur. Phys. J. A **56**, 139 (2020).

[49] Luis Roca, Maxim Mai, Eulogio Oset, and Ulf-G. Meißner, Predictions for the $\Lambda_b \to J/\psi\Lambda(1405)$ decay, Eur. Phys. J. C **75**, 218 (2015).

[50] Maxim Mai and Ulf-G. Meißner, Constraints on the chiral unitary $\bar{K}N$ amplitude from $\pi\Sigma K^+$ photoproduction data, Eur. Phys. J. A **51**, 30 (2015).

[51] Matthias F. M. Lutz and Madeleine Soyeur, The associated photoproduction of positive kaons and pi0 Lambda or pi Sigma pairs in the region of the Sigma(1385) and Lambda (1405) resonances, Nucl. Phys. **A748**, 499 (2005).

[52] Kristian Piscicchia *et al.*, First simultaneous $K^-p \to \Sigma^0\pi^0$, $\Lambda\pi^0$ cross section measurements at 98 MeV/c, Phys. Rev. C **108**, 055201 (2023).

[53] F. Ambrosino *et al.*, Data handling, reconstruction, and simulation for the KLOE experiment, Nucl. Instrum. Methods Phys. Res., Sect. A **534**, 403 (2004).

[54] J. Ciborowski *et al.*, Kaon scattering and charged sigma hyperon production in K^-p interactions below 300 MeV/c, J. Phys. G **8**, 13 (1982).

[55] William E. Humphrey and Ronald R. Ross, Low-energy interactions of K^- mesons in hydrogen, Phys. Rev. **127**, 1305 (1962).

[56] M. Sakitt, T. B. Day, R. G. Glasser, N. Seeman, J. H. Friedman, W. E. Humphrey, and R. R. Ross, Low-energy K^- meson interactions in hydrogen, Phys. Rev. **139**, B719 (1965).

[57] Mason B. Watson, Massimiliano Ferro-Luzzi, and Robert D. Tripp, Analysis of Y_0^* (1520) and determination of the Σ parity, Phys. Rev. **131**, 2248 (1963).

[58] D. Sadasivan, M. Mai, and M. Döring, S- and p-wave structure of $S = -1$ meson-baryon scattering in the resonance region, Phys. Lett. B **789**, 329 (2019).

[59] R. F. Ferguson, D. G. Ireland, and B. McKinnon, Data-driven approach for interpolation of sparse data, arXiv:2505.01473.

[60] R. J. Nowak *et al.*, Charged sigma hyperon production by K- meson interactions at rest, Nucl. Phys. **B139**, 61 (1978).

[61] D. N. Tovee *et al.*, Some properties of the charged sigma hyperons, Nucl. Phys. **B33**, 493 (1971).

[62] M. Bazzi *et al.* (SIDDHARTA Collaboration), A new measurement of kaonic hydrogen x-rays, Phys. Lett. B **704**, 113–117 (2011).

[63] Ulf-G. Meißner, Udit Raha, and Akaki Rusetsky, Spectrum and decays of kaonic hydrogen, Eur. Phys. J. C **35**, 349 (2004).

[64] Ulf-G. Meißner, Udit Raha, and Akaki Rusetsky, Kaon-nucleon scattering lengths from kaonic deuterium experiments, Eur. Phys. J. C **47**, 473 (2006).

[65] A. Cieply and J. Smejkal, Kaonic hydrogen versus the K^-p low energy data, Eur. Phys. J. A **34**, 237 (2007).

[66] N. V. Shevchenko, Light kaonic atoms: From "corrected" to "summed up" Deser formula, Few Body Syst. **63**, 22 (2022).

[67] F. Sgaramella *et al.*, The SIDDHARTA-2 experiment for high precision kaonic atoms X-ray spectroscopy at DAΦNE, Nuovo Cimento C **47**, 285 (2024).

[68] K. Piscicchia *et al.*, First measurement of the $K^-n \to \Lambda\pi^-$ non-resonant transition amplitude below threshold, Phys. Lett. B **782**, 339 (2018).

[69] Rajan Gupta, Introduction to lattice QCD: Course, in Les Houches Summer School in Theoretical Physics, Session 68: Probing the Standard Model of Particle Interactions (1997), pp. 83–219, arXiv:hep-lat/9807028.

[70] Maxwell T. Hansen and Stephen R. Sharpe, Relativistic, model-independent, three-particle quantization condition, Phys. Rev. D **90**, 116003 (2014).

[71] M. Mai and M. Döring, Three-body unitarity in the finite volume, Eur. Phys. J. A **53**, 240 (2017).

[72] J. Gasser, M. E. Sainio, and A. Svarc, Nucleons with chiral loops, Nucl. Phys. **B307**, 779 (1988).

[73] Veronique Bernard, Norbert Kaiser, Joachim Kambor, and Ulf-G. Meißner, Chiral structure of the nucleon, Nucl. Phys. **B388**, 315 (1992).

[74] Hua-Bin Tang, A new approach to chiral perturbation theory for matter fields, arXiv:hep-ph/9607436.

[75] Thomas Becher and H. Leutwyler, Baryon chiral perturbation theory in manifestly Lorentz invariant form, Eur. Phys. J. **9**, 643 (1999).

[76] Paul J. Ellis and Hua-Bin Tang, Pion nucleon scattering in a new approach to chiral perturbation theory, Phys. Rev. C **57**, 3356 (1998).

[77] Maxim Mai, Peter C. Bruns, Bastian Kubis, and Ulf-G. Meißner, Aspects of meson-baryon scattering in three and two-flavor chiral perturbation theory, Phys. Rev. D **80**, 094006 (2009).

[78] Zhan-Wei Liu, Jonathan M. M. Hall, Derek B. Leinweber, Anthony W. Thomas, and Jia-Jun Wu, Structure of the **Λ(1405)** from Hamiltonian effective field theory, Phys. Rev. D **95**, 014506 (2017).

[79] Zhan-Wei Liu, Jia-Jun Wu, Derek B. Leinweber, and Anthony W. Thomas, Kaonic hydrogen and deuterium in Hamiltonian effective field theory, Phys. Lett. B **808**, 135652 (2020).

[80] Jiong-Jiong Liu, Zhan-Wei Liu, Kan Chen, Dan Guo, Derek B. Leinweber, Xiang Liu, and Anthony W. Thomas, Structure of the $\Lambda(1670)$ resonance, Phys. Rev. D **109**, 054025 (2024).

[81] K. Azizi, Y. Sarac, and H. Sundu, Investigation of $\Lambda(1405)$ as a molecular pentaquark state, Eur. Phys. J. C **84**, 428 (2024).

[82] K. Azizi, B. Barsbay, and H. Sundu, Mass and residue of $\Lambda(1405)$ as hybrid and excited ordinary baryon, Eur. Phys. J. Plus **133**, 121 (2018).

[83] Norbert Kaiser, T. Waas, and W. Weise, SU(3) chiral dynamics with coupled channels: Eta and kaon photoproduction, Nucl. Phys. **A612**, 297 (1997).

[84] M. F. M. Lutz and E. E. Kolomeitsev, Relativistic chiral SU (3) symmetry, large N(c) sum rules and meson baryon scattering, Nucl. Phys. **A700**, 193 (2002).

[85] B. Borasoy, R. Nissler, and W. Weise, Chiral dynamics of kaon-nucleon interactions, revisited, Eur. Phys. J. A **25**, 79 (2005).

[86] A. Krause, Baryon matrix elements of the vector current in chiral perturbation theory, Helv. Phys. Acta **63**, 3 (1990).

[87] Matthias Frink, Ulf-G. Meißner, and Ilka Scheller, Baryon masses, chiral extrapolations, and all that, Eur. Phys. J. A **24**, 395 (2005).

[88] B. Borasoy, P. C. Bruns, Ulf-G. Meißner, and R. Nissler, A Gauge invariant chiral unitary framework for kaon photo- and electroproduction on the proton, Eur. Phys. J. A **34**, 161 (2007).

[89] Dino Ruić, Maxim Mai, and Ulf-G. Meißner, η-Photoproduction in a gauge-invariant chiral unitary framework, Phys. Lett. B **704**, 659 (2011).

[90] Maxim Mai, Peter C. Bruns, and Ulf-G. Meißner, Pion photoproduction off the proton in a gauge-invariant chiral unitary framework, Phys. Rev. D **86**, 094033 (2012).

[91] Peter C. Bruns and Maxim Mai, Chiral symmetry constraints on resonant amplitudes, Phys. Lett. B **778**, 43 (2018).

[92] Maxim Mai, Theory of resonances, arXiv:2502.02654.

[93] J. A. Oller, Coupled-channel approach in hadron–hadron scattering, Prog. Part. Nucl. Phys. **110**, 103728 (2020).

[94] Albert Feijoo, Daniel Gazda, Volodymyr Magas, and Angels Ramos, The K^-N interaction in higher partial waves, Symmetry **13**, 1434 (2021).

[95] Feng-Kun Guo, Yuki Kamiya, Maxim Mai, and Ulf-G. Meißner, New insights into the nature of the $\Lambda(1380)$ and $\Lambda(1405)$ resonances away from the SU(3) limit, Phys. Lett. B **846**, 138264 (2023).

[96] Tetsuo Hyodo, Daisuke Jido, and Atsushi Hosaka, Origin of the resonances in the chiral unitary approach, Phys. Rev. C **78**, 025203 (2008).

[97] A. Cieply and J. Smejkal, Chirally motivated $\bar{K}N$ amplitudes for in-medium applications, Nucl. Phys. **A881**, 115 (2012).

[98] P. C. Bruns and A. Cieplý, SU(3) flavor symmetry considerations for the K^- N coupled channels system, Nucl. Phys. **A1019**, 122378 (2022).

[99] P. C. Bruns, A. Cieplý, and M. Mai, Testing chiral unitary models for the $\Lambda(1405)$ in $\mathrm{K} + \pi\Sigma$ photoproduction, Phys. Rev. D **106**, 074017 (2022).

[100] Maxim Mai, Michael Döring, and Akaki Rusetsky, Multi-particle systems on the lattice and chiral extrapolations: A brief review, Eur. Phys. J. Special Topics **230**, 1623 (2021).

[101] Daniel Severt, Maxim Mai, and Ulf-G. Meißner, Particle-dimer approach for the Roper resonance in a finite volume, J. High Energy Phys. 04 (2023) 100.

[102] M. Doring, C. Hanhart, F. Huang, S. Krewald, and U.-G. Meißner, Analytic properties of the scattering amplitude and resonances parameters in a meson exchange model, Nucl. Phys. **A829**, 170 (2009).

[103] Tanishk Shrimal, Sara Collins, Priyajit Jana, M. Padmanath, and Sasa Prelovsek, Lattice study of $cc\bar{u}\,\bar{s}$ tetraquark channel in $D^{(*)}D_s^{(*)}$ scattering, Phys. Rev. D **112**, 054513 (2025).

[104] Ivan Vujmilovic, Sara Collins, Luka Leskovec, Emmanuel Ortiz-Pacheco, Padmanath Madanagopalan, and Sasa Prelovsek, T_{cc}^+ via the plane wave approach and including diquark-antidiquark operators, Proc. Sci., LATTICE2024 (**2025**) 112 [arXiv:2411.08646].

[105] Luka Leskovec, Stefan Meinel, Martin Pflaumer, and Marc Wagner, Lattice QCD investigation of a doubly-bottom $\bar{b}\,\bar{b}\,ud$ tetraquark with quantum numbers $I(J^P) = 0(1^+)$, Phys. Rev. D **100**, 014503 (2019).

[106] Stefan Meinel, Martin Pflaumer, and Marc Wagner, Search for $\bar{b}\,\bar{b}\,us$ and $\bar{b}\,\bar{c}\,ud$ tetraquark bound states using lattice QCD, Phys. Rev. D **106**, 034507 (2022).

[107] Sara Collins, Alexey Nefediev, M. Padmanath, and Sasa Prelovsek, Toward the quark mass dependence of T_{cc}^+ from lattice QCD, Phys. Rev. D **109**, 094509 (2024).

[108] Meng-Lin Du, Arseniy Filin, Vadim Baru, Xiang-Kun Dong, Evgeny Epelbaum, Feng-Kun Guo, Christoph Hanhart, Alexey Nefediev, Juan Nieves, and Qian Wang, Role of left-hand cut contributions on pole extractions from lattice data: Case study for $T_{cc}(3875)^+$, Phys. Rev. Lett. **131**, 131903 (2023).

[109] Lu Meng, Vadim Baru, Evgeny Epelbaum, Arseniy A. Filin, and Ashot M. Gasparyan, Solving the left-hand cut problem in lattice QCD: $T_{cc}(3875)^+$ from finite volume energy levels, Phys. Rev. D **109**, L071506 (2024).

[110] Sebastian M. Dawid, Fernando Romero-López, and Stephen R. Sharpe, Comparison of integral equations used to study T_{cc}^{+}, J. High Energy Phys. 09 (2025) 058.
[111] S. Prelovsek, E. Ortiz-Pacheco, S. Collins, L. Leskovec, M. Padmanath, and I. Vujmilovic, Doubly heavy tetraquarks from lattice QCD: Incorporating diquark-antidiquark operators and the left-hand cut, Phys. Rev. D **112**, 014507 (2025).
[112] Andrei Alexandru, Ruairí Brett, Chris Culver, Michael Döring, Dehua Guo, Frank X. Lee, and Maxim Mai, Finite-volume energy spectrum of the $K^{-}K^{-}K^{-}$ system, Phys. Rev. D **102**, 114523 (2020).
[113] Sebastian M. Dawid, Zachary T. Draper, Andrew D. Hanlon, Ben Hörz, Colin Morningstar, Fernando Romero-López, Stephen R. Sharpe, and Sarah Skinner, Two- and three-meson scattering amplitudes with physical quark masses from lattice QCD, Phys. Rev. D **112**, 014505 (2025).
[114] Sebastian M. Dawid, Zachary T. Draper, Andrew D. Hanlon, Ben Hörz, Colin Morningstar, Fernando Romero-López, Stephen R. Sharpe, and Sarah Skinner, QCD predictions for physical multimeson scattering amplitudes, Phys. Rev. Lett. **135**, 021903 (2025).
[115] Haobo Yan, Maxim Mai, Marco Garofalo, Ulf-G. Meißner, Chuan Liu, Liuming Liu, and Carsten Urbach, ω meson from lattice QCD, Phys. Rev. Lett. **133**, 211906 (2024).
[116] Marco Garofalo, Maxim Mai, Fernando Romero-López, Akaki Rusetsky, and Carsten Urbach, Three-body resonances in the φ^4 theory, J. High Energy Phys. 02 (2023) 252.
[117] Daniel Sadasivan, Andrei Alexandru, Hakan Akdag, Felipe Amorim, Ruairí Brett, Chris Culver, Michael Döring, Frank X. Lee, and Maxim Mai, Pole position of the $a_1(1260)$ resonance in a three-body unitary framework, Phys. Rev. D **105**, 054020 (2022).
[118] Maxim Mai, Andrei Alexandru, Ruairí Brett, Chris Culver, Michael Döring, Frank X. Lee, and Daniel Sadasivan (GWQCD Collaboration), Three-body dynamics of the $a_1(1260)$ resonance from lattice QCD, Phys. Rev. Lett. **127**, 222001 (2021).
[119] D. Sadasivan, M. Mai, H. Akdag, and M. Döring, Dalitz plots and lineshape of $a_1(1260)$ from a relativistic three-body unitary approach, Phys. Rev. D **101**, 094018 (2020); **103**, 019901(E) (2021).
[120] Andrew R. Liddle, Information criteria for astrophysical model selection, Mon. Not. R. Astron. Soc. **377**, L74 (2007).
[121] H. Akaike, A new look at the statistical model identification, IEEE Trans. Autom. Control **19**, 716 (1974).
[122] Gideon Schwarz, Estimating the dimension of a model, Ann. Stat. **6**, 461 (1978).
[123] V. Bernard, Norbert Kaiser, and Ulf-G. Meissner, Chiral dynamics in nucleons and nuclei, Int. J. Mod. Phys. E **04**, 193 (1995).
[124] Matthias F. M. Lutz, Yonggoo Heo, and Renwick J. Hudspith, QCD in the chiral SU(3) limit from baryon masses on lattice QCD ensembles, Phys. Rev. D **110**, 094046 (2024).
[125] Scott Willenbrock, Mass and width of an unstable particle, Eur. Phys. J. Plus **139**, 523 (2024).
[126] A. Cieply, E. Friedman, A. Gal, D. Gazda, and J. Mares, K^{-} nuclear potentials from in-medium chirally motivated models, Phys. Rev. C **84**, 045206 (2011).
[127] Miguel Salg, Fernando Romero-López, and William I. Jay, Bayesian analysis and analytic continuation of scattering amplitudes from lattice QCD, arXiv:2506.16161.
[128] Maxim Mai, Chris Culver, Andrei Alexandru, Michael Döring, and Frank X. Lee, Cross-channel study of pion scattering from lattice QCD, Phys. Rev. D **100**, 114514 (2019).
[129] Dehua Guo, Andrei Alexandru, Raquel Molina, Maxim Mai, and Michael Döring, Extraction of isoscalar $\pi\pi$ phase-shifts from lattice QCD, Phys. Rev. D **98**, 014507 (2018).
[130] R. Molina and M. Döring, Pole structure of the $\Lambda(1405)$ in a recent QCD simulation, Phys. Rev. D **94**, 056010 (2016); **94**, 079901(A) (2016).
[131] Michael Döring, Bin Hu, and Maxim Mai, Chiral extrapolation of the sigma resonance, Phys. Lett. B **782**, 785 (2018).
[132] Peter C. Bruns and Ales Cieply, Chirally motivated $\pi\Sigma - \bar{K}N$ model in a finite volume, Eur. Phys. J. A **61**, 44 (2025).
[133] Zejian Zhuang, Raquel Molina, Jun-Xu Lu, and Li-Sheng Geng, Pole trajectories of the $\Lambda(1405)$ help establish its dynamical nature, Sci. Bull. **70**, 1953 (2025).
[134] https://github.com/maxim-mai/Supplemental_Material_arXiv2507.14283.